The Impinging Jet

Robert Wilke

The Impinging Jet

vorgelegt von
Dipl.-Ing.
Robert Wilke
geb. in Leinefelde

von der Fakultät V – Verkehrs- und Maschinensysteme
der Technischen Universität Berlin
zur Erlangung des akademischen Grades

Doktor der Ingenieurwissenschaften
- Dr.-Ing. -

genehmigte Dissertation

Promotionsausschuss:

Vorsitzender: Prof. Dr.-Ing. Utz von Wagner
Gutachter: Prof. Dr. sc. techn. habil. Jörn Sesterhenn
Prof. Dr. Luca Marino

Tag der wissenschaftlichen Aussprache: 3. Juli 2017

Berlin 2017

Zusammenfassung

Die interne Kühlung von Turbinenschaufeln und Triebwerke senkrecht startender und landender Flugzeuge sind nur zwei von vielen Anwendungsbeispielen, bei denen Prallstrahlen genutzt werden. Um globale Ressourcen zu schützen, wird eine Steigerung der Kühleffizienz benötigt. Deshalb wurden und werden enorme Forschungsaktivitäten bezüglich Prallstrahlen durchgeführt. Trotz bedeutenden Fortschritten während der letzten Jahrzehnte gibt es noch immer eine Wissenslücke mit Hinsicht auf deren turbulente Strömung. Diese Lücke muss geschlossen werden, um effizientere Kühlkonfigurationen entwickeln zu können. Eine weitere Fragestellung betrifft die Emission von tonalem Lärm. Dieser schädigt nicht nur das menschliche Hörsystem, sondern führt auch zu Materialermüdung und –versagen, insbesondere im Überschallfall. Es ist unstrittig, dass ein Rückkopplungsmechanismus für die Generierung dieser zerstörerischen Schallwellen verantwortlich ist. Dennoch ist die Rolle der Stöße in Prallplattennähe sowie der Wirbel unklar und umstritten.

In dieser Dissertation werden Prallstrahlen mittels direkter numerischer Simulationen untersucht. Mit diesem Ansatz kann das Wissen bezüglich der Dynamik des Prallstrahls erweitert werden. Dazu werden Beobachtungen der transienten Strömung sowie statistische Auswertungen und Informationen über die modale Struktur des Prallstrahls präsentiert. Diese Einblicke werden mit den Themen Wärmeübergang und Schallemission in Verbindung gebracht. Die Mechanismen der Schallentstehung in supersonischen Prallstrahlen mit niedrigem Druckverhältnis ($NPR = 2.15$) und weitem Strahlabstand ($h/D = 5$) werden aufgezeigt.

Abstract

The internal cooling of turbine blades and vertical take off and landing aircraft engines are just two of many examples where impinging jets are used. In order to save global resources, an increase of cooling efficiency is wanted. Therefore, enormous research activities have been and are presently being carried out with respect to impinging jets. Despite substantial advances within the last decades, a knowledge gap still exists concerning its turbulent flow. This gap needs to be closed in order to develop more efficient cooling configurations. An additional problem is the emission of vastly loud tonal noise. This noise does not only damage the human hearing system, but also leads to material fatigue and failure, especially in the supersonic case. A feedback-loop mechanism is generally accepted to generate those destructive sound waves. Nonetheless, the role of standoff shocks and vortices in that respect is unclear and controversial.

Within this dissertation, impinging jets are investigated by means of direct numerical simulations. Using this approach, the knowledge of the dynamics is extended by providing observations of the transient flow, statistical results as well as information about impinging jet modes. These insights are related to the topics heat transfer and sound emission. The sound source mechanism within supersonic impinging jets of low nozzle pressure ratio ($NPR = 2.15$) and high nozzle-to-plate distance ($h/D = 5$) are revealed.

Vorwort

Diese Arbeit entstand während meiner Tätigkeit als wissenschaftlicher Mitarbeiter im Fachgebiet für Numerische Fluiddynamik der Technischen Universität Berlin. Mein herzlicher Dank gilt Herrn Prof. Sesterhenn, der von Anfang an begeistert vom *Impinging Tone* war und mir die Möglichkeit gegeben hat, an diesem spannenden Thema zu forschen. Insbesondere bedanke ich mich für die sehr gute Betreuung, die zahlreichen fachlichen Diskussionen und die Initiierung der Kooperation mit der Universität La Sapienza in Rom, welche sowohl beruflich als auch privat einzigartige Resultate hervorgebracht hat.

Sono molto grato al Prof. Marino e a Giorgia Sinibaldi per avermi dato l'opportunità di trascorrere 3 mesi al Dipartimento di Ingegneria Meccanica e Aerospaziale, e di partecipare ad alcuni esperimenti sul rumore del getto impattante.

Darüber hinaus danke ich all meinen Kollegen und Freunden am Fachgebiet, insbesondere Mathias, Lewin, Sergio, Sonja, Juanjo, Jens, Christian, Julius, Steffen, Tommy, Sophie, Lars und Martin für die Unterstützung und die tolle Atmosphäre. Ich hatte das Glück, Teil des Sonderforschungsbereichs 1029 *TurbIn* sein zu dürfen. Dieser hat sich zum Ziel gesetzt, den Wirkungsgrad von Gasturbinen um mehr als 10% zu steigern. In diesem Kontext habe ich mich mit der Prallkühlung von Turbinenschaufeln beschäftigt. Ich danke Herrn Prof. King, Niko und Steffi für die hervorragende Organisation des SFB. Allen Mitgliedern danke ich für die konstruktiven Diskussionen und den guten Zusammenhalt. Unser Teamgeist entstand auf den regelmäßigen Sommerschulen in Italien. Vielen Dank an die Professoren und WM's, die sich daran beteiligt haben.

Mein Dank gilt ebenfalls der Deutschen Forschungsgemeinschaft (DFG), welche den SFB und somit auch meine Stelle und meinen Aufenthalt an der La Sapienza finanziert hat. Finanzielle Unterstützung habe ich ebenfalls vom Höchstleistungsrechenzentrum Stuttgart (HLRS) in Form von enormen Rechenkapazitäten erhalten, die ich kostenfrei nutzen durfte. Dafür bedanke ich mich herzlich. Ohne die gewaltigen Kontingente von mehr als 80 Millionen Kern-Stunden der Projekte GCS-NOIJ/12993 und GCS-ARSI/44027 wäre diese Arbeit nicht möglich gewesen. Die Rechnungen wurden auf den Supercomputern Cray XE6 (Hermit) und Cray XC40 (Hornet, Hazel Hen) durchgeführt.

Ganz besonders danke ich meiner Familie, im Besonderen meinen Eltern Astrid und Jörn für die langjährige Förderung während meines Studiums und die moralische Unterstützung, insbesondere in der Anfangsphase dieses Unterfangens.

Infine, ringrazio la mia ragazza Giorgia per avermi tranquillizzato e supportato soprattutto nelle ultime settimane, e per aver ascoltato la mia presentazione così tante volte, che alla fine avrebbe potuto tenere lei stessa il discorso. Grazie mille, amore!

Robert Wilke Stuttgart, 2. August 2017

Contents

Zusammenfassung **I**

Abstract **III**

Vorwort **V**

List of Figures **XIII**

List of Tables **XVII**

Nomenclature **XIX**

Thesis overview **XXV**

1 Introduction **1**

1.1 Flow characteristics 1
1.2 Heat transfer 6
1.2.1 Stationary impinging jets 7
1.2.2 Pulsating impinging jets 8
1.2.3 Numerical simulation of impinging jets 10
1.3 Sound emission 12
1.3.1 Free jet noise 12
1.3.2 Free jet modes 15
1.3.3 Impinging jet noise 17
1.3.4 Impinging jet modes 19
1.4 Objective of this thesis 21

2 Numerical model 23

2.1 Governing equations 23

2.1.1 Direct numerical simulation 23

2.1.2 Navier–Stokes equations 25

2.1.3 Characteristik formulation 26

2.2 Discretisation 28

2.2.1 Space discretisation 28

2.2.2 Parallelisation 29

2.2.3 Time discretisation 31

2.2.4 Shock treatment 33

2.3 Computational domain 35

2.3.1 Boundary conditions 35

2.3.2 Sponge 39

2.3.3 Grid stretching 42

2.3.4 Parameters 44

3 Methods for flow analysis 47

3.1 Averaged equations 47

3.1.1 Averaged governing equations 47

3.1.2 Reynolds stress transport 50

3.1.3 Turbulent heat flux transport 52

3.1.4 Averaging of the impinging jet 53

3.2 Dynamic mode decomposition 57

4 Description of the flow 61

4.1 Resolution 61

4.1.1 Kolmogorov microscales 61

4.1.2 Energy spectra 63

4.1.3 Boundary layer 64

4.2 Vortex dynamics 66

4.2.1 Primary and secondary vortex rings 66

4.2.2 Leapfrogging and vortex split-off 67

4.3 Modes . . . 70
  4.3.1 Subsonic impinging jets . . . 70
  4.3.2 Supersonic impinging jets . . . 77
  4.3.3 Schlieren imaging . . . 83
4.4 Deflection zone and standoff shock . . . 85
4.5 Wall jet . . . 89
4.6 Boundary layer . . . 92

5 The impinging tone **97**
5.1 Sound source mechanism for low supersonic flow . . . 97
  5.1.1 Type 1: Shock-vortex-interaction . . . 97
  5.1.2 Type 2: Shock-vortex-shock-interaction . . . 99
  5.1.3 Closure of the feedback loop . . . 103
5.2 Emanated sound . . . 104
5.3 Comparison to a free jet . . . 107
  5.3.1 Impinging tone and screech . . . 107
  5.3.2 Impinging jet and free jet modes . . . 109
5.4 Zone of silence . . . 110

6 Heat transfer **113**
6.1 Modes and heat transfer . . . 113
  6.1.1 Nusselt number . . . 113
  6.1.2 Turbulent heat flux . . . 115
  6.1.3 Pulsating impinging jets . . . 117
6.2 Reynolds analogies and correlations . . . 119
  6.2.1 Mean field . . . 119
  6.2.2 Fluctuations . . . 123
  6.2.3 Additional correlations . . . 125
6.3 Reynolds stresses . . . 128
6.4 Reynolds stress budgets . . . 131

7 Conclusion and Outlook **135**

A Appendix **141**
A.1 Methods for flow analysis 141
A.1.1 Calculation rules for averages 141
A.1.2 Cylindrical coordinates 144
A.1.3 Transport equations in cylindrical coordinates 146
A.1.4 Convergence 156
A.2 Description of the flow 157
A.2.1 Modes 157
A.2.2 Deflection zone and standoff shock 165
A.3 Heat transfer 166
A.3.1 Turbulent heat flux 166
A.3.2 Fluctuations 167
A.3.3 Reynolds stress budgets 169

References **173**

Publications related to this thesis **179**

List of Figures

1.1 Flow regions of supersonic impinging jets 2
1.2 Shock wave positions of supersonic impinging jets 6
1.3 Increase of heat transfer effectivity due to pulsation 9
1.4 Noise spectum of a supersonic jet 14
1.5 Screech feedback loop 14
1.6 Supersonic jet modes 16
1.7 Zone of silence 19

2.1 Domain decomposition 30
2.2 Scaling of the code 31
2.3 Shock-capturing filter 34
2.4 Computational domain 40
2.5 Sponge 41
2.6 Grid stretching 43

3.1 Convergence of averaging 56

4.1 Ratio of mesh width to Kolmogorov length scale 62
4.2 Energy spectra 64
4.3 y^+ at the impinging plate 65
4.4 Vortical structure of the impinging jet 68
4.5 Leapfrogging 69
4.6 Vortex split-off 70
4.7 Convergence of DMD and eigenvalue spectrum #5 71
4.8 Dominant dynamic modes #5: T 72

4.9 Dominant dynamic modes #5: Q 73
4.10 Original and reconstructed flow field #5 73
4.11 3D dominant dynamic modes #5: Q 74
4.12 Convergence of DMD and eigenvalue spectrum #6 76
4.13 Dominant dynamic modes #6: T 76
4.14 Original and reconstructed flow field #6 76
4.15 DMD eigenvalue spectrum #3 77
4.16 Periodical flow of a supersonic impinging #3 80
4.17 3D dominant dynamic mode #3: p 80
4.18 Different modes of simulation #1 82
4.19 Dominant dynamic modes of the impinging jet 82
4.20 Toepler Z-type schlieren arrangement 84
4.21 Experimental set-up for schlieren visualisation 84
4.22 Schlieren image for $NPR = 2.15$ 85
4.23 Pressure recovery at the impinging plate 86
4.24 Radial velocity fluctuations 87
4.25 Standoff shock position 88
4.26 Mean profiles of u_r and v 90
4.27 Mean profiles of T 91
4.28 Velocity boundary layer 94
4.29 Temperature boundary layer 95

5.1 Shock-vortex-interaction 101
5.2 Shock-vortex-shock-interaction 103
5.3 Feedback loop of a supersonic impinging jet 104
5.4 SPL of different configurations of the impinging jet 105
5.5 SPL of two different modes #1 106
5.6 p and v along the axis of the free and the impinging jet 108
5.7 SPL of the impinging and the free jet 109
5.8 3D dynamic modes (p) of impinging tone and screech 110

6.1 Nusselt number 115

6.2 Stagnation point nusselt number 115
6.3 Turbulent heat flux, Influence of Re 117
6.4 Pulsating impinging jet. 119
6.5 Skin friction factor 121
6.6 Reynolds analogy and Chilton Colburn analogy 121
6.7 Crocco-Busemann relation and generalized Reynolds analogy . 123
6.8 Scatter plots of fluctuations #6 125
6.9 RMS values of p and ρ for $Ma < 1$ 126
6.10 Scatter plots of fluctuations #6 127
6.11 Reynolds stress tensor 129
6.12 Relation of vortices to Reynolds stresses 131
6.13 Budget of $\overline{\rho u_\theta''^2}$ 132
6.14 Budget of $\overline{\rho v''^2}$ 133
6.15 Budget of $\overline{\rho u_r''^2}$ 134
6.16 Budget of $\overline{\rho v'' u_r''}$ 134

A.1 Convergence of averaging 156
A.2 Convergence of circumferential velocity 156
A.3 DMD eigenvalue spectrum #4 157
A.4 Dominant dynamic modes #4: T 157
A.5 Dominant dynamic modes #4: Q 158
A.6 Original and reconstructed flow field #4 158
A.7 Convergence of DMD #5 159
A.8 DMD eigenvalue spectrum #5 159
A.9 Mode $Sr = 0.46$ #5: T 160
A.10 Mode $Sr = 0.92$ #5: T 160
A.11 Reconstructed flow field #5 160
A.12 3D dominant dynamic modes #5: p 161
A.13 Dominant dynamic modes #6: Q 162
A.14 3D dominant dynamic modes #6: Q 162
A.15 3D dominant dynamic modes #6: p 163
A.16 Experimental set-up for schlieren visualisation 164

A.17 Axial velocity fluctuations 165
A.18 Pressure fluctuations 165
A.19 Turbulent heat flux, Influence of Ma 166
A.20 Scatter plots of fluctuations #5 167
A.21 Scatter plots of fluctuations #5 168
A.22 RST budget #1 169
A.23 RST budget #2 170
A.24 RST budget #3 171
A.25 RST budget #4 172

List of Tables

1.1 Overview of DNS of impinging jets 11

2.1 Scaling of the code 32
2.2 Common geometrical and physical parameters 45
2.3 Specific geometrical and physical parameters 45

5.1 Strouhal numbers of impinging tones 107

6.1 Correlation coefficients #6. 128

Nomenclature

Within this thesis, the variables are denoted with its common symbols. It is inevitable that some symbols are used repeatedly with different meanings, depending on the context. The respective meaning is clearly brought out within the text. Variables that are used only within a single short section and are not essential for the aims of the thesis are not listed.

All units are given in the legends of diagrams. If no unit is written, it means that the quantity is dimensionless. Within the captions, → and ↓ indicate the reading directions *left to right* and *top to down*.

* .. unit depends on components

Capital letters

C_f	–	skin friction factor
D, D^*	m	diameter, displaced ∼
DM	*	dynamic mode
E	J kg^{-1}	(specific) total energy
$E_{uu,vv,ww}$	J kg^{-1}	kinetic energy
F	*	right-hand side of Navier-Stokes equations
L_s	m	shock cell spacing
L_T	m	jet-to-jet spacing
$L_{x,y,z}$	m	domain size
Ma	–	Mach number
N	–	number of samples
NPR	–	nozzle pressure ratio
Nu, Nu_0	–	Nusselt number, stagnation point ∼

Pr, Pr_t	$-$	Prandtl number, turbulent $\sim$
Q	s^{-2}	2^{nd} invariant of velocity gradient tensor
R	$-$	Bravais-Pearson correlation coefficient
R_s	$\mathrm{J\ kg^{-1}\ K^{-1}}$	specific gas constant
Re	$-$	Reynolds number
S	*	companion matrix
SPL	dB	sound pressure level
Sr	$-$	Strouhal number
St	$-$	Stanton number
T, T_t	K	temperature, total $\sim$
T^+	$-$	dimensionless temperature
T_τ	K	friction temperature
U	*	flow field vector $U = (p, u, v, w, s)^\top$
V	*	snapshot matrix
X, Y, Z	$\mathrm{m\ s^{-2}}$	plane characteristic waves

Small letters

c	$\mathrm{m\ s^{-1}}$	speed of sound
c	$-$	coefficient vector
c_p, c_v	$\mathrm{J\ kg^{-1}\ K^{-1}}$	specific heat capacity at constant pressure / volume
e	$\mathrm{J\ kg^{-1}}$	(specific) internal energy
e	$-$	Euler's number ($e \approx 2.71828$)
e_{kin}	$\mathrm{J\ kg^{-1}}$	(specific) kinetic energy
f, f_s	Hz	frequency, screech $\sim$
f	$-$	spatial function for inlet definition
h	m	nozzle-to-plate distance
h	$-$	dimensionless mesh width
i	$-$	number of cores
k	$\mathrm{W\ m^{-1}\ K^{-1}}$	thermal conductivity
$k_{x,y,z}$	m^{-1}	wave number

l	m	nozzle-shock spacing
l_η	m	Kolmogorov length scale
m, n	–	exponents for Nusselt number correlation
$\dot{m}$	kg s^{-1}	mass flow
n	–	total number of grid points
p, p_t	Pa	pressure, total ∼
q, r		arbitrary variable out of U
q_i	W m^{-2}	heat flux vector
q_w	W m^{-2}	heat flux component normal to the wall at the wall
r	m	radial coordinate
r	–	recovery factor
r	*	residual vector
r_η	–	ratio of mesh width to Kolmogorov length
s	J kg^{-1} K^{-1}	(specific) entropy
s_{ij}	s^{-1}	rate-of-strain tensor
t, t_p	s	time, perfusion ∼
u, v, w	m s^{-1}	velocity in x, y, z-direction
u^+	–	dimensionless velocity
$u_{\theta,r}$	m s^{-1}	velocity in θ, r direction
u_τ	m s^{-1}	friction velocity
v	*	snapshot
x	*	eigenvectors of companion matrix S
x, y, z	m	Cartesian coordinates
x_c, y_c, z_c	m	positional parameter in x, y, z-direction
x_c^*, y_c^*, z_c^*	–	dimensionless position x, y, z-direction
y^+	–	dimensionless wall distance

Greek capital letters

ΔT	K	temperature difference ($\Delta T = T_{t,in} - T_w$)
$\Delta x, \Delta y, \Delta z$	m	mesh width

Φ	Pa s^{-1}	dissipation function
Φ_{Re}	–	heat transfer effectivity

Greek small letters

δ_{ij}	–	Kronecker delta
δ_s	m	shock width
δ^*	m	radial displacement
ϵ	m^2 s^{-3}	dissipation rate
η	kg m^{-1} s^{-1}	dynamic viscosity
θ	–	circumferential coordinate
κ	–	ratio of specific heats
λ, λ^*	*	eigenvalues of companion matrix S
ν	m^2 s^{-1}	kinematic viscosity
π	–	pi ($\pi \approx 3.14159$)
ρ	kg m^{-3}	density
σ^{sc}	–	shock filtering strength
σ_1	–	first root of the zero order Bessel function ($\sigma_1 \approx 2.4048$)
σ_s	–	sponge function
τ_{ij}	Pa	viscous stress tensor
τ_s	–	strength parameter of sponge
τ_w	Pa	wall shear stress
χ	°	radiation angle

Subscripts

$\star_\infty$	at fully expanded or ambient condition
$\star_\delta$	at the boundary layer edge
$\star_{in}$	at the inlet
$\star_{i,j,k}$	Cartesian spatial directions
$\star_r$	radial direction
$\star_{ref}$	reference

$\star_w$	at the wall
$\star_{\mathrm{RMS}}$	root mean square

Superscripts

$\star'$	Reynolds fluctuation
$\star'$	first derivative of the variable
$\star''$	Favre fluctuation
$\overline{\star}$	Reynolds average
$\widetilde{\star}$	Favre average
$\star^{\pm}$	acoustic wave
$\star^{(n)}$	time step
$\star^{s}$	entropy wave
$\star^{u,v,w}$	transport wave

Abbreviations

CBR	Crocco-Busemann relation
CCA	Chilton Colburn analogy
CFD	computational fluid dynamics
DMD	dynamic mode decomposition
DNS	direct numerical simulation
FFT	fast Fourier transform
GRA	reneralized Reynolds analogy
LES	large eddy simulation
RA	Reynolds analogy
RANS	Reynolds-averaged Navier–Stokes (equations / simulation)
RMS	root mean square
RST	Reynolds stress tensor
THF	turbulent heat flux

Thesis overview

This dissertation covers the two most important issues of impinging jets: heat transfer and emanated sound. Within the introduction (chapter 1), the state of research is given and the open questions are addressed. Afterwards, the used numerical model (chapter 2) as well as analysis methods (chapter 3) are explained. The heart of this thesis is divided into three chapters. Chapter 4 establishes a basis for the investigation of the two key topics taking a closer look at dynamic aspects of the impinging jet flow. After that, a chapter concerning the impinging tone follows (chapter 5). In chapter 6, heat transfer and related statistical quantities are investigated. In chapter 7, the dissertation is concluded and an outlook is given. Additional diagrams that are not discussed are given in the appendix for validation purposes.

1 Introduction

Jets impinging on a flat plate have a considerable number of applications in engineering. Heating and cooling configurations rank among the most important uses. Impinging jets are characterised by the occurrence of intense temperature gradients at heated or cooled impinging plates and thus enable a strong local heat transfer. For this reason impinging jets are applied to thermally high stressed components such as turbine blades.

Equally important is the use as rocket engine or vertical and/or short take off and landing aircraft aero engine. The obstructed jets are typically operated under pressure ratios high enough to allow a supersonic flow. The operation is characterised by the emission of destructive loud tonal noise that can cause deafness and material fatigue.

In the following sections, the state of research is given and the open questions concerning heat transfer efficiency improvement and noise source mechanisms are revealed.

1.1 Flow characteristics

Impinging jets have been studied for decades. Therefore, the basic flow characteristics are well-known and described in several reviews, such as Hrycak (1981), Jambunathan et al. (1992) ,Viskanta (1993), Weigand & Spring (2011). Following these reviews, the impinging jet contains three zones: the free jet, the deflection zone and the wall jet, as described in the following. A schematic illustration of a supersonic impinging jet is given in figure 1.1.

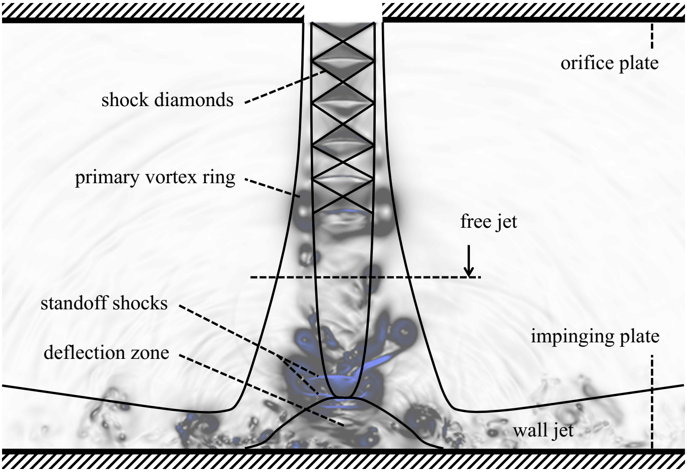

Figure 1.1: Schematic illustration of the flow of a supersonic impinging jet

The free jet contains a shear layer between the high velocity gas jet and the surrounding stagnant gas that leads to the development of Kelvin-Helmholtz instabilities. Primary ring vortices develop and grow as they are transported downstream. This mixing entrains fluid from the surrounding area. Consequently, the jet broadens and the diameter of the unaffected fluid (potential core) decreases. According to Livingood & Hrycak (1973), the potential core for turbulent flow is 6 to 7 nozzle diameters. In this thesis, all computed impinging jets have a nozzle-to-plate distance of five diameters. Therefore, the length of the potential core is decreased and ends in the region of the stagnation flow.

In the deflection zone, the axial velocity rapidly decreases and the static pressure rises. Consequently, the radial velocity strongly increases. The wall-normal extension of this zone is approximatively between 1.2 and 2 nozzle diameters. The flow in this region is also referred to as stagnation flow.

The radial velocity reaches a maximum at around one diameter from the jet axis within the wall jet. Compared to a simple wall-parallel flow, the turbulence generated within the shear layer between the wall and the wall jet leads to higher heat transfer. A second shear layer exists, analogue to the free jet region, between the high velocity wall gas jet and the surrounding stagnant gas. Both shear layers lead to a widening of the wall jet with increasing radial distance.

Two more effects occur in the case of supersonic under-expanded impinging jets: shocks within the free jet and standoff shocks in and above the deflection zone. Depending on flow conditions, a recirculation region within the deflection zone may occur as well.

The shocks within the free jet are caused by an imperfect expansion. This happens when the pressure at the nozzle exit p_{in} of supersonic jets is not equal to the ambient pressure p_∞. If $p_{in} > p_\infty$, the jet is called under-expanded and when $p_{in} < p_\infty$ it is called over-expanded. The most common way to study this phenomenon is to use a high pressure reservoir and a low pressure reservoir e.g. the environment (Norman et al. (1982)). For subsonic jets p_{in} is always equal to p_∞. We assume no total pressure loss within the nozzle, so that the total pressure at the nozzle exit $p_{t,in}$ (= inlet of the domain) is equal to the reservoir pressure. The ratio $p_{t,in}/p_\infty$ is called nozzle pressure ratio *NPR*. If it is higher than $\left((\kappa+1)/2\right)^{\kappa/(\kappa-1)}$, an under-expanded jet forms for convergent nozzles (Iwamoto (1990)). For air ($\kappa = 1.4$) the critical NPR is 1.893. In this dissertation, only subsonic and under-expanded supersonic impinging jets are looked at. As shown in figure 1.1, slightly under-expanded jets feature characteristic shock diamonds. Following Adamson & Nicholls (1959), this phenomenon occurs as follows: Gas leaves the nozzle and expands going through an expansion fan to the ambient pressure at the jet boundary. As the expansion waves reach the jet boundary, they are reflected as compression waves and are sent back into the flow. These waves coalesce to form intercepting shocks. The repetition of this effect forms the characteristic shock cells or shock diamonds that are illustrated in figure 1.1. For fully expanded Mach numbers

$$Ma_\infty = \sqrt{\left(\left(\frac{p_{t,in}}{p_\infty}\right)^{\frac{\kappa-1}{\kappa}} - 1\right)\frac{2}{\kappa-1}} \tag{1.1}$$

higher than approximately two, a normal shock, also referred to as Mach disk, may appear at the end of the first shock cell. Ma_∞ is a reasonable parameter, since all chocked jet have a Mach number of one at the orifice. The Mach disk creates a region of mixed sub- and supersonic flow (Schulze (2013)). Mach disks can appear in impinging jets at lower pressure, but only when the nozzle-to-plate distance is less than about 1½ diameters (Henderson (2002)). The fully expanded Mach number of the supersonic simulations presented in this thesis is $Ma_\infty = 1.106$. The nozzle-to-plate distance h is 5 diameters. Therefore, Mach disks are not considered further. According to Tam & Tanna (1982), the shock cell spacing L_s can be approximated as:

$$L_s \approx \pi\sqrt{Ma_\infty^2 - 1}\,\frac{D_\infty}{\sigma_1}\ . \tag{1.2}$$

$\sigma_1 = 2.4048$ and is the first root of the zero order Bessel function. D_∞ is the fully expanded jet diameter. Regarding equation (1.2), it follows that shock cells become larger with increasing fully expanded Mach number respectively *NPR*. D_∞ can be derived by the condition of conservation of mass flux and using isentropic flow relations:

$$D_\infty = D\left(\frac{1+\frac{1}{2}(\kappa-1)Ma_\infty^2}{1+\frac{1}{2}(\kappa-1)Ma_d^2}\right)^{\frac{\kappa+1}{4(\kappa-1)}}\sqrt{\frac{Ma_d}{Ma_\infty}}\ . \tag{1.3}$$

With a design Mach number Ma_d of one and $Ma_\infty = 1.106$, the fully expanded jet diameter is approximatively equal to the nozzle diameter D:

$$D_\infty = 1.0044D \approx D\ . \tag{1.4}$$

Therefore, in this thesis no difference between D and D_∞ is made. The approximation error of 0.44% is negligible compared to the influence of the inlet velocity profile, as described later in section 2.3.1.

Iwamoto (1990) investigated the shock wave location experimentally. The distance between the nozzle and the shock waves l were measured on shadowgraph pictures for $NPR = 3$. Figure 1.2 shows the dependence of l on the nozzle-to-plate distance h. Hence, the distance between the shock and the impinging plate is $(h - l)$. For nozzle-to-plate distances $h/D \lesssim 1.5$, a single shock stands in front of the impinging plate. The distance between the shock wave and the impinging plate $(h - l)$ is almost independent of h/D. When $h/D \gtrsim 2$, the mentioned shock wave remains at the position of the free jet shock and a second shock appears whose distance to the impinging plate likewise remains constant, until the third shock can occur with further increasing h/D. As a consequence of the chosen parameters ($NPR = 3.0$, $h/D \leq 4$), a maximum of three shock cells fit between the nozzle and the impinging plate. Regarding a free jet, shock cells close to the nozzle are relatively clear and stationary. Shock cells farther downstream are effected much stronger by the ever-growing vortices and loose in strength. All configurations investigated by Iwamoto (1990) are relatively stationary concerning the shock cells of the free jet region and consequently the standoff shock. The occurrence and behaviour of the standoff shock in configurations with lower NPR and greater h/D remain unclear.

As mentioned above, a stagnation bubble may occur in the impingement region. According to Sinibaldi et al. (2013) it is still unclear under which conditions this recirculation region forms, but it may be connected to the Mach disk. A summary of research on this topic is given in Henderson (2002). The stagnation bubble does not occur in the simulations presented in this thesis and is not further considered.

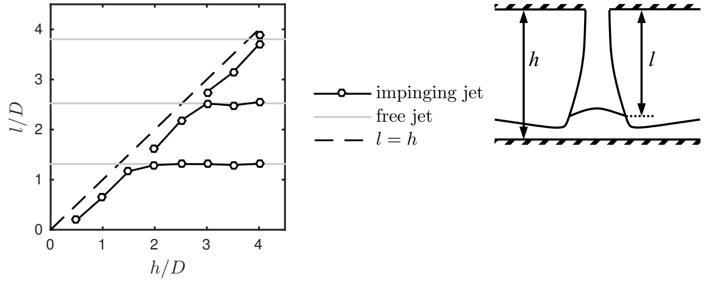

Figure 1.2: Position of the shock waves at the jet boundary at $NPR = 3.0$: nozzle-shock spacing l as function of the nozzle-to-plate distance h. Data from Iwamoto (1990).

1.2 Heat transfer

Subsonic impinging jets are used for the heating and cooling of surfaces. One important example is the cooling of turbine blades. Higher turbine entry temperatures increase the total efficiency of the thermodynamic cycle (Uhlmann (2003)). Also new engine and combustion concepts such as pulsed detonation, which is studied within the *Collaborative Research Centre 1029*, cause higher thermal loads of the blades. These loads need to be counteracted with a more efficient cooling mechanism, which can evacuate a higher heat quantity at unchanged demand of cooling mass flow. A promising approach is the use of pulsating impinging jets.

Despite enormous research efforts within the last decades, still little is known about turbulence of both, unforced and forced impinging jets. These information are essential for a possible increase of heat transfer efficiency.

1.2.1 Stationary impinging jets

Following Weigand & Spring (2011), the heat transfer caused by impingement of a jet onto a flat plate is affected by many different factors, such as the exit velocity, the velocity profile, the geometry of the nozzle or the orifice, the turbulence level, the entrainment condition, the nozzle-to-plate distance and the thermal boundary condition at the wall. The highest heat transfer is typically reached in the stagnation point. With increasing axial distance, the heat transfer decreases monotonously, except for low h/D. Here, a secondary maximum can occur. In praxis, multiple impinging jets (arrays) are used in order to cool surfaces. Arrays are not further considered in this thesis, but one important parameter, namely h/D, can only be chosen meaningfully, when multiple jets are involved. The question to an optimal arrangement of nozzles for a given cooling mass flow per area involves the diameter D, the nozzle-to-plate distance h/D and the distance between the jets L_T/D. Considering all three parameters (D, h, L_T), no reasonable optimum can be derived. The steady decrease of all three parameters leads in theory to an ever increasing heat transfer coefficient. Consequently, the optimisation makes only sense if one parameter is fixed. The common choice for the given parameter is h (Martin (1977)). Under this condition, optimal nozzle-to-plate distances are reported to be in the range of six to eight diameters Weigand & Spring (2011). According to Martin (1977), the optimal nozzle-to-plate distance is $h/D \approx 5$. In this thesis, $h/D = 5$ is used for all simulations.

Heat transfer at the impinging plate is quantified by the Nusselt number:

$$Nu = \frac{D}{\Delta T} \cdot \left.\frac{\partial T}{\partial y}\right|_w = q_w \frac{D Pr}{\Delta T c_p \eta} \ . \tag{1.5}$$

D is the inlet diameter, ΔT is the difference between the total inlet temperature $T_{t,in}$ and the wall temperature T_w. Pr, c_p, η and q_w are the Prandtl number, the ratio of specific heats, the dynamic viscosity and the heat flux in the wall-normal direction at the wall. Most research was carried out in order to find approximations for the Nusselt number in the shape of a power law:

$$Nu \sim Re^m Pr^n \ . \tag{1.6}$$

The Prandtl and Reynolds numbers

$$Pr = \frac{\eta c_p}{k} \ , \tag{1.7}$$

$$Re = \frac{v_\infty D}{\nu} \ . \tag{1.8}$$

relate viscous to thermal diffusion rate respectively inertial to viscous forces. k, v_∞ and ν are the thermal conductivity, the fully expanded inlet velocity and the kinematic viscosity. Typical values for the exponents within equation (1.6) are $0.5 \leq m \leq 0.9$ and $n = 1/3$ (Weigand & Spring (2011)). It is obvious that Nu increases with increasing Reynolds number. This kind of correlation can be extended with geometrical parameters, such as the nozzle-to-plate distance and the distance between the jets, in case of arrays.

1.2.2 Pulsating impinging jets

Pulsating impinging jets are not the central topic of this thesis. However the results presented in this work help to understand the physics of the stationary impinging jet. Some of its characteristics, e.g. the modal structure, as shown later, are crucial for the research concerning pulsating impinging jets.

Two different strategies exist with the aim to increase heat transfer efficiency of the impinging jet. In the first one, shear layer instabilities are excited by the use of loudspeakers. The introduced disturbances are relatively low: the amplitude reaches $(0.1 - 2\%)$ of the inlet velocity. A summary of this method is given in Janetzke (2010).

The second method deals with a much stronger excitation. The entire jet is influenced by a pulsating inlet, e.g. due to a valve. Janetzke

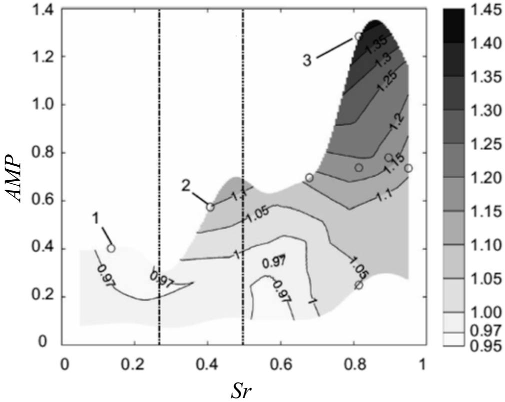

Figure 1.3: Increase of heat transfer effectivity Φ_{Re} of pulsating impinging jets related to a stationary one, depending on the Strouhal number Sr and amplitude AMP. Modified from Janetzke (2010).

(2010) experimentally investigated such configurations. He found that the pulsation with a Strouhal number of approximately 0.85 and maximal amplitude (on/off) increases the heat transfer compared to a non-pulsating jet of 40%. The mass flow has been kept constant. Figure 1.3 shows the increase of heat transfer effectivity

$$\Phi_{Re} = \left(\frac{Nu_p}{Nu} \right)^{1/m} \tag{1.9}$$

depending on the amplitude AMP and the Strouhal number Sr. The subscript p addresses the pulsated case. Nu (without subscript) referres to the non-pulsed reference. m is the exponent of the correlation (see equation (1.6)), based on the stationary reference case. The exponent found by Janetzke (2010) is $m = 0.524$. In the range $0.5 \lesssim Sr \lesssim 0.9$, exactly one primary vortex ring per actuator cycle was generated. The increased vortex diameter causes higher wall shear stresses, which were found due to the use of oil painting pictures. The reason for the generation of larger primary vortex rings at this specific frequency remained unclear. However according to Janetzke (2010), the shear layer instabilities are meaningless for this strategy. Investigation of other authors are summarised in Janetzke (2010) as well. It is pointed out that the question for a fluid dynamical explanation of the effects on heat transfer due to pulsation is still open.

1.2.3 Numerical simulation of impinging jets

Experiments are able to reveal optimal geometrical arrangements as well as Strouhal numbers which can increase the heat transfer efficiency due to trying out. However, complete physical explanations can only be found if numerical simulations are carried out as well. Simulations can provide all quantities of the turbulent flow spatially and temporally well resolved. In the following, the state of the art is reviewed briefly, using the article of Wilke & Sesterhenn (2016c).

Most existing publications of a numerical nature use either turbulence models for the closure of the Reynolds-averaged Navier-Stokes (RANS) equations, e.g. Zuckerman & Lior (2005), or large eddy simulation (LES), e.g. Cziesla et al. (2001).

Due to the lack of computing power in the past, direct numerical simulations (DNS) carried out early are either at low (laminar) Reynolds number ($Re < 3000$) or under-resolved “false DNS” (Satake & Kunugi (1998), Hattori & Nagano (2004)). For example, Hattori & Nagano (2004) performed a 2.5-dimensional “DNS” on 3 million grid points ($Re = 9120$) on a large domain of $26 \times 2 \times 1.6$ diameters. As a comparison, the simulations described in this thesis are performed with more than one billion grid points for $Re = 8000$.

The only true DNS of a fully turbulent impinging jet beside the simulations presented in this dissertation, and the corresponding own articles, was carried out from Dairay et al. (2014, 2015). They conducted a DNS of a round impinging jet with a nozzle to plate distance of two and focused on the secondary maximum of the heat transfer distribution and

Publication	Re	grid size
Satake & Kunugi (1998)	10000	$192 \times 220 \times 192 \ \left(8.11 \cdot 10^6\right)$
Chung & Luo (2002)*	1000	$256 \times 256 \ \left(0.07 \cdot 10^6\right)$
Tsubokura et al. (2003)	2000	$100 \times 150 \times 96 \ \left(1.44 \cdot 10^6\right)$
Hattori & Nagano (2004)**	9120	$320 \times 96 \times 96 \ \left(2.95 \cdot 10^6\right)$
Tsujimoto et al. (2009)	1500	$256 \times 200 \times 256 \ \left(13.11 \cdot 10^6\right)$
Dairay et al. (2015)	10000	$1541 \times 401 \times 1541 \ \left(952.25 \cdot 10^6\right)$
own simulations	3300	$512 \times 512 \times 512 \ \left(134.22 \cdot 10^6\right)$
own simulations	8000	$1024 \times 1024 \times 1024 \ \left(1073.74 \cdot 10^6\right)$

Table 1.1: Overview of direct numerical simulations of impinging jets. Simulations marked with * and ** are two-dimensional respectively 2.5-dimensional.

on the connection to elongated structures. The influence of the small-scale component of the flow on the heat transfer is subtle and leads to radially elongated cold spots in the instantaneous Nusselt number distribution. In addition, LES are carried out and compared to the DNS data. The results show that conventional subgrid-scale models based on eddy viscosity (dynamic Smagorinsky, WALE models) deliver unrealistic heat transfer predictions in the impingement region. The use of a discrete viscous operator significantly improves the heat transfer prediction in this region. However, none of the LES models was able to clearly predict the secondary peak in the Nusselt number distribution, as measured and computed with DNS. The simulations presented in this thesis differ, since the nozzle-to-plate-distance is larger ($h/D = 5$ vs. $h/D = 2$) and we analyse a compressible flow at Mach numbers between 0.4 and 1.1, instead of an incompressible impinging jet. In table 1.1, all direct numerical simulations available in the literature are listed.

One more important issue found by Kharoua & Khezzar (2011) is the fact that the use of symmetry conditions prevents flapping modes and leads to artificial recirculation areas in the vicinity of these boundary conditions and consequently to an unrealistic heat transfer prediction. An in-line array by the use of LES on 9.5 million grid points with $Re = 20000$ was simulated.

1.3 Sound emission

Impinging jets feature a flow region that is equal to the flow of a free jet if the plate distance is large enough. Hence, the sound sources present in free jets also exist within impinging jets. These sources and their relation to jet modes are briefly explained in the following (sections 1.3.1 and 1.3.2). Afterwards (section 1.3.3), we concentrate on the main topic: the additional sound source within impinging jets, referred to as impinging tones. This sound source differs in its origin according to sub- and supersonic flow. In the under-expanded supersonic case, this source has a similar mechanism like screech tones, which occur in under-expanded free jets. In section 1.3.4, we shortly review what is known about modes of the impinging jet.

1.3.1 Free jet noise

Following Tam (1995) and Schulze (2013), a brief summary concerning free jet noise is given. For subsonic jets, the only sound source is turbulent mixing noise.

Turbulent mixing noise is of low frequency f and occurs at Strouhal numbers

$$Sr = \frac{f D_\infty}{v_\infty} \tag{1.10}$$

in the range of $0.1 \lesssim Sr \lesssim 0.25$. It is caused by large and small turbulent structures in the mixing layer of the jet. Large structures are believed to cause the dominant part of the noise whereas smaller structures are believed to generate background noise. The dominant part of turbulent mixing noise is radiated in the downstream direction. The intensity as well as the directional and spectral characteristics depend on the Mach number and the ratio of jet to ambient temperature.

In under-expanded jets, two additional sound sources appear: broadband shock-associated noise and screech noise.

Broadband shock-associated noise is caused by the interaction of downstream propagating large scale structures with the quasi-periodic shock cell structure of the under-expanded jet. This source causes a peak on the right of the spectrum, at higher frequencies than the screech tone. Figure 1.4 shows a typical far-field noise spectrum of a supersonic jet. The sound pressure level SPL is defined as:

$$SPL = 20 \log_{10} \left(\frac{p'_{\mathrm{RMS}}}{p_{ref}} \right) , \tag{1.11}$$

where p'_{RMS} is the root mean square of the pressure fluctuation and p_{ref} is a reference pressure. In this thesis, p_{ref} has the common value of $2 \cdot 10^{-5}$ Pa. Broadband shock noise is the dominant sound source mechanism in the upstream direction. The corresponding peak frequency changes with the direction of radiation.

Screech tones are discrete tones that are generated due to a feedback mechanism. Powell (1953) was the first to observe this mechanism (Schulze (2013)). As described in section 1.1, vortical structures develop in the shear layer of the jet due to Kelvin-Helmholtz instabilities (1). These structures grow while they are convected downstream. When large scale structures reach the fourth or fifth shock cell, both interact with each other and emit strong acoustic waves (2) that propagate upstream (3). These waves reach the nozzle lip or upper plate, if present, and excite the shear layer of the jet (4). As a consequence, new instability waves are generated (1), which close of the feedback mechanism. The loop is shown in figure 1.5.

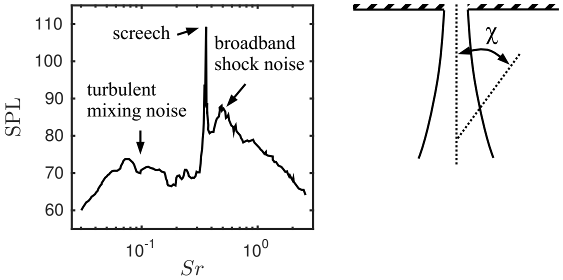

Figure 1.4: Typical far-field noise spectum of a supersonic jet. Microphone at $\chi = 30°$ to the nozzle inlet direction. See Tam (1995), original data from Seiner & Yu (1984).

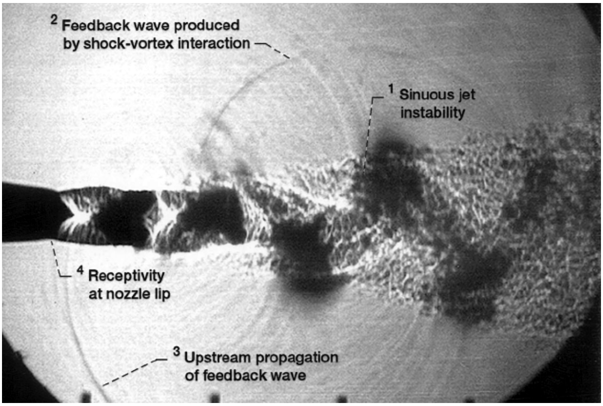
2 Feedback wave produced
by shock-vortex interaction
1 Sinuous jet
instability
4 Receptivity
at nozzle lip
3 Upstream propagation
of feedback wave

Figure 1.5: Screech feedback loop of a rectangular jet (aspect ratio = 9), $Ma_\infty = 1.5$. From Raman (1997).

The interaction between shock cells and vortices (2) was described by Suzuki and Lele Suzuki & Lele (2003), based on a two-dimensional (2D) direct numerical simulation. Peña Fernández & Sesterhenn (2015) performed a three-dimensional direct numerical simulation of a round starting jet. They found that the shock-wave present in the core of the trailing jet is bent by shear layer vortices that reach the shock-wave. As a result, the shock transforms into a strong acoustic wave that is radiated apart the jet.

Screech noise is associated with corresponding modes referred to as screech modes. These modes are described in section 1.3.2. Following Tam (1995), screech is usually accompanied by its harmonics. The fundamental mode radiates primarily in the upstream direction, whereas the principal direction of the first harmonic is $\chi = 90^\circ$.

Since the screech frequency depends on the shock cell spacing and therefore on the fully expanded Mach number, the frequency can be approximated analysing the travel times of a large coherent structure and the acoustic wave. In Schulze (2013), a summary concerning these estimation is given. It is noted that assumptions concerning the convection velocity of the structure are not consistent in the literature and thus the screech frequency is difficult to predict.

1.3.2 Free jet modes

Screech noise is closely related to jet modes. Based on the work of Powell et al. (1992) and Panda (1998), five acoustic modes exist and are labelled alphabetically: A_1, A_2, B, C, D and E. The occurrence of these modes depends on the nozzle pressure ratio, and consequently the fully expanded jet Mach number. Important is that the shape of the mode determines the emanated sound. A_1 and A_2 are axisymmetric (varicose, toroidal), B and D are flapping. Powell et al. (1992) denote them “primarily flapping” as they can occasionally appear as helical. A flapping mode can be considered as a superposition of two helical modes with the same amplitude and opposite sense. In case one of them is missing or weak, what is possible since B and D are not very robust, the resulting mode remains helical. Mode C is helical. Mode E is unknown, but in the case of an elliptic nozzle it is known to split up in different modes denoted E_1, E_2 and E_3. The fact that it splits up in the elliptical case could indicate that we deal with several modes indeed. Figure 1.6 shows the dominant screech frequency as function of Ma_∞. Little is known about Reynolds number effects. The

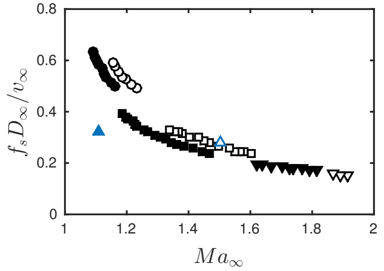

Figure 1.6: Supersonic jet modes: dominant screech frequency f_s as function of Ma_∞. Adapted from Schulze (2013); experimental data from Panda et al. (1997). The two triangles with the peak oriented to the top indicate DNS of four own group. Filled: $Re = 8000, Ma_\infty = 1.106$ Wilke & Sesterhenn (2015b), not filled: $Re = 5000, Ma_\infty = 1.55$ Schulze (2013). $D_\infty, v_\infty, Ma_\infty$ denote the fully expanded values of diameter, jet velocity and Mach number.

primary cause for that is a lack of data and the fact that most experiments have been performed at high Reynolds numbers, which arrise naturally if experiments are done with reasonable size. However, DNS from our own group Schulze (2013) at $Ma_\infty = 1.55$ and $Re = 5000$ as well as the simulation described in section 5.3 indicate that the correspondence of Ma_∞ to modal structure might be distorted. This is also supported by a simulation of Sesterhenn et al. (2013), who report a change in modal structure when particles are added to the jet. This might be due to the change of density of the jet, which then would also lead to the conclusion that heating changes the modes.

One more issue deserves attention: A closer look at figure 1.6 shows that for some Mach numbers, multiple modes exist. For example at $Ma_\infty \approx 1.2$, we observe A_1, A_2, and B as possible candidates, each of which having a different frequency. The mechanism of the mode selection is still unclear. A possible way to study this phenomenon would be the attempt to select different modes with the choice of different initial conditions where the boundary conditions are equal. The coexisting states are underlined, but mode selection is not topic of this thesis.

1.3.3 Impinging jet noise

Noise emanated by impinging jets can be caused by the three sources that are present in free jets (turbulent mixing noise, broadband shock-associated noise and screech tones, as described in section 1.3.1) plus an additional sound source: the *impinging tone.* This source emits tonal noise that appears similarly to screech in the sound spectrum. Therefore, both sources have to be distinguished carefully. The source of screech noise is located between the rear edge of the third and fifth shock cell. As a consequence, the nozzle-to-plate distance needs to measure at least five diameters ($h/D \geq 5$) in order to allow the generation of screech tones (Sinibaldi et al. (2013)). This statement assumes a NPR above a certain value. As we will see in section 5.3.1, at low supersonic Mach number, a decreased nozzle-to-plate distances of approximately four diameters should be sufficient for the generation of screach. A large proportion of the research was concentrated on very close plates and high pressure ratios ($NPR > 3$, Sinibaldi et al. (2013)). This set-up avoids the mixing up of the two mechanisms. The configurations chosen in this thesis theoretically allow the appearance of screech as well as impinging tones. However, both mechanisms can be distinguished, as it is explained in section 5.3.1.

Following Wilke & Sesterhenn (2016b), a summary of the state of research is given. Impinging jets may emanate incredibly loud tonal noise if the Mach number is sufficiently high ($Ma \gtrsim 0.7$) and the plate is less than about 7.5 diameters away from the nozzle (Ho & Nosseir (1981)). In addition to these discrete tones, the presence of the impinging plate also increases the overall sound pressure level (OASPL). Marsh (1961) noticed that for subsonic impinging jets the OASPL increases with decreasing nozzle-to-plate distance (h/D).

The loud tonal components in the sound spectrum (impinging tones) were early found to be caused by a feedback loop involving a shear layer instability travelling downstream and an acoustic wave travelling upstream in a subsonic part of the flow (Rockwell & Naudascher (1979)). This is in analogy with the screech tone generation mechanism described in section 1.3.1. This idea was supported by Ho & Nosseir (1981) as well as Henderson & Powell (1993), Henderson (2002). Nevertheless, it remained unclear how exactly the feedback loop is closed in the supersonic case. Ho & Nosseir (1981) identified primary vortices impinging on the plate as the possible missing link in the feedback chain. On the contrary, Henderson & Powell (1993) identified standoff shock oscillations as the responsible mechanism within the loop. For subsonic cases, no shock is present. Consequently, direct interaction of primary vortices with the impinging plate is reported as the only possible sound source mechanism. The sound source of subsonic impinging jets is not considered further within this dissertation.

One more issue deserves some special emphasis: the *zone of silence*. Powell (1988), Henderson & Powell (1993), Henderson (2002) reported a zone, in which the configuration does not allow the production of impinging tones. Crutial for this phenomenon are NPR and h/D. The analysed nozzle pressure ratios are in the ranges $3.38 \leq NPR \leq 4.50$. In contrast, for ideally expanded jets, Krothapalli et al. (1999) found continuously tones for h/D up to 10. Henderson (2002) argued that both configurations (ideally and under-expanded) differ strongly in the shock-wave structure. Consequently, the zone of silence and the production of impinging tones must be affected by the shock-wave structure. He also proposed that tones generated at $5 \leq h/D \leq 10$ may be related to screech noise.

Sinibaldi et al. (2015) conducted acoustic and particle image velocimetry (PIV) measurements of supersonic under-expanded impinging jets. NPR between two and four were analysed for nozzle-to-plate distances of two, three and four diameters. The zone of silence shifts to higher values of NPR with increasing h/D. For $h/D = 3$, the zone of silence ranges from $3.1 \lesssim NPR \lesssim 3.5$. For $h/D = 4$, the zone of silence starts at $NPR \approx 3.2$ and goes at least until $NPR \lesssim 4$. Sinibaldi et al. (2015) suggest that the interaction of the shear layer vortices with the plate is the only source

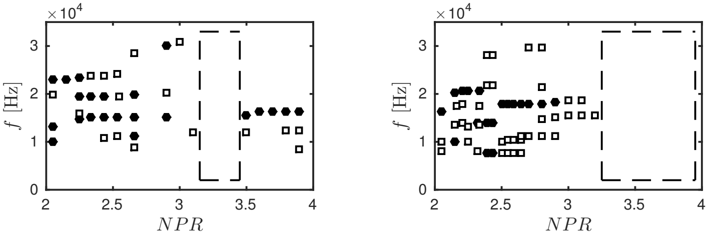

Figure 1.7: Discrete tone frequency distribution over NPR. Left: $h/D = 3$, right: $h/D = 4$. Filled markers: dominant tones, empty markers: secondary tones, dashed line: zone of silence. Data from Sinibaldi et al. (2015).

of impinging tones in the pre-silence region, since the standoff shock is not present. In the post-silence region, the standoff shock oscillations are believed to be the only possible source of impinging tones. This is antithetical to the observations of Mitchell et al. (2012) and Buchmann et al. (2012), who captured images of the receptivity at the nozzle (step (4) in the feedback loop, see figure 1.5) by means of schlieren images from a high-speed camera. The investigated case is located in the pre-silence region ($NPR = 3.2, h/D = 4$) and clearly shows the presence of a standoff shock. Also Hirata et al. (1971) were able to observe standoff shock oscillations for large h/D.

1.3.4 Impinging jet modes

In sections 1.3.1 and 1.3.2, we saw that free jet screech is strongly related to the modal structure of the jet. Despite this topic is still being investigated, the gained knowledge during the past decades is substantial. On the contrary, comparably little is known about impinging jet modes. Following Wilke & Sesterhenn (2016b), a summary of the state of research is given.

Tam & Ahuja (1990) state that only axisymmetrical modes are possible for subsonic impinging jets, whereas also helical modes can occur in the supersonic case. This conclusion is based on an analytical model and studies found in the literature: Neuwerth (1974, 1981) observed torodial, helical and flapping (superposition of two helical) modes for supersonic impinging jets. A helical coherent structure for a free jet was observed as well at $Ma = 0.8$. While adding an impinging plate (without changing any other parameter), the mode changed to axisymmetrical. Nosseir & Ho (1982) also observed an axisymmetrical mode for an impinging jet with $Ma = 0.7$.

Krothapalli et al. (1999) conducted experiments involving ideally expanded free and impinging jets at $Ma_\infty = 1.5$. The mode of the free jet was found to be helical. Approaching the plate, this mode remains dominant until $h/D = 8$. In the range $4 \lesssim h/D \lesssim 6$, the axisymmetyric mode begins to dominate. A further decrease of the nozzle-to-plate distance leads to a re-emergence of the helical mode.

Tsubokura et al. (2003) conducted a direct numerical simulation with $Re = 2000$. The flow at this Reynolds number is not fully turbulent, since therefore $Re \gtrsim 3000$ is required (Hrycak (1981)). The simulation with $h/D = 10$ showed a mode that is axisymmetrical close to the orifice plate, but asymmetric close to the impinging plate.

A recent numerical investigation was performed by Uzun et al. (2013). They conducted a large eddy simulation (LES) with a plate distance of five diameters and a fully expanded Mach number of 1.5. The coherent axisymmetrical structures found using a dynamic mode decomposition (DMD) correspond to the dominant tone at $Sr \approx 0.33$.

1.4 Objective of this thesis

Numerous research activities concerning impinging jets were carried out during the last decades. Despite enormous advanced in the understanding of the physics of impinging jets, many open questions remain. Within this thesis, direct numerical simulations of subsonic and under-expanded supersonic impinging jets are presented in order to extend the knowledge concerning the following issues:

Statistics of the turbulent flow and heat transfer. The heat transfer efficiency can be increased by the use of pulsating impinging jets. It is however unclear why one large primary vortex ring can be generated in the frequency range $0.5 \lesssim Sr \lesssim 0.9$. Even the flow field of the unforced impinging jet is still not completely understood. Compared to free jets, pipe and channel flows, little is known about turbulence of impinging jets.

The objective of this thesis is to identify and to bring the modes of the impinging jets into accordance with the known average and instantaneous flow phenomena. A complete statistical analysis, including among others the turbulent heat flux, the Reynolds stress tensor and correlations of statistical variables is provided for two uses: First, to complement the analysis of the flow and second, to provide a data base for the improvement of LES and RANS models.

Impinging tone. The generation of impinging tones is generally accepted to be caused due to a feedback mechanism. If vortices impinging on the wall or standoff shock oscillations generate the feedback wave in the supersonic case is controversial and presently not clarified. Little is known about the relation between modes and impinging tones. In addition, the occurrence of a standoff shock within the zone of silence and its position is debatable.

The aim of this thesis is to identify the sound source mechanism of the impinging jet in the supersonic pre-silence region. This includes an analysis of the two most important aspects of the flow: the jet instability and the standoff shock. The mechanism is brought into accordance with the modes of the impinging jet and the feedback loop analogous to the free jet shown in figure 1.5. The sound spectra are analysed and the impinging tones are distinguished from free jet screech.

2 Numerical model

2.1 Governing equations

2.1.1 Direct numerical simulation

Flows subject to friction are described by the Navier-Stokes equations (section 2.1.2). Unfortunately, no analytical solution for this system of differential equations exists. In order to find a numerical approximation of the flow, different strategies exist: direct numerical simulation (DNS), large eddy simulation (LES) and Reynolds-averaged Navier-Stokes simulation (RANS).

Turbulent flows are characterised by three-dimensional stochastic distributed fluctuations of fluid particles in space and time that are superposed on a mean flow (Frederich (2010)). Those fluctuations in form of vortices occur in different time and length scales. The latter range from the order of magnitude of the size of the domain to the smallest energy dissipating scales. Since the turbulent kinetic energy is transferred downwards to smaller and smaller scales, the smallest ones have to be resolved by the numerical grid. If this is not the case, the energy cannot be dissipated and, depending on the peculiarity of the under-resolution, the results can become imprecise and the computation can "explode". The resolution of small scales is discussed in section 4.1. If all scales are resolved by the numerical grid, the simulation is called DNS. This is the most accurate method within computational fluid dynamics (CFD). The problem of DNS is that enormous computing capacities are necessary for relatively low Reynolds numbers ($\mathcal{O}\left(10^3\right)$), which are often too low for practical applications. Therefore, direct numerical simulation is nowadays still restricted to academic problems.

In order to decrease the computational costs, RANS or URANS (unsteady RANS) is used. This method is standard for industrial applications. The Reynolds-averaged Navier-Stokes equations are solved instead of the Navier-Stokes equations. The problem that rises is that unknown terms, e.g. the Reynolds stresses and the turbulent heat flux occur and need to be modelled. This leads to the failure of this method for heat transfer prediction. Additionally, RANS simulations use the integral formulation of the equations of motion by default. As a consequence, fine pressure fluctuations fall within the order of magnitude of numerical inaccuracy. This prevents the investigation of generated sound or noise using RANS.

Large eddy simulation lies in between DNS and RANS concerning computational costs as well as accuracy. Large scales are resolved and small scales, which cannot be resolved on the numerical grid, are modelled using a subgrid-scale model. The question that arises now is: Are the small scales important for a) acoustics and b) heat transfer of impinging jets? With regard to acoustics, LES is unable to predict the high-frequency noise components (Schulze (2013)). If those are not of interest, LES may be an appropriate choice. As already noted in section 1.2.3, Dairay et al. (2014) observed that none of the tested LES models was able to clearly predict the secondary peak in the Nusselt number distribution, as measured and computed with DNS. This investigation is the only one in the literature, where LES was directly compared to well-resolved DNS of a fully turbulent impinging jet.

Summing up, only direct numerical simulations make it possible to simultaneously study the source mechanism(s) of impinging tones and to perform a precise analysis on its statistics, including heat transfer, of the turbulent flow. Therefore, DNS was the method of choice to realise this thesis.

2.1.2 Navier–Stokes equations

The Navier-Stokes equations consist of the non-linear equations for the conservation of mass (2.1a), momentum (2.1b) and energy (2.1c). For a three-dimensional Cartesian coordinate system they read:

$$\frac{\partial \rho}{\partial t} + \frac{\partial \rho u_j}{\partial x_j} = 0 \tag{2.1a}$$

$$\frac{\partial \rho u_i}{\partial t} + \frac{\partial \rho u_i u_j}{\partial x_j} = -\frac{\partial p}{\partial x_i} + \frac{\partial \tau_{ij}}{\partial x_j} \tag{2.1b}$$

$$\frac{\partial \rho e}{\partial t} + \frac{\partial \rho e u_j}{\partial x_j} = -\frac{\partial q_j}{\partial x_j} - p\frac{\partial u_j}{\partial x_j} + \Phi\ . \tag{2.1c}$$

Time, density, pressure, internal energy and velocity in the direction x_i are denoted as t, ρ, p, e and u_i. The viscous stress tensor τ_{ij} can be expressed using the Kronecker delta δ_{ij}:

$$\tau_{ij} = 2\eta\left(s_{ij} - \frac{1}{3}s_{kk}\delta_{ij}\right) + \mu_d s_{kk}\delta_{ij}\ , \tag{2.2}$$

where s_{ij} is the rate-of-strain tensor:

$$s_{ij} = \frac{1}{2}\left(\frac{\partial u_i}{\partial x_j} + \frac{\partial u_j}{\partial x_i}\right)\ . \tag{2.3}$$

The bulk viscosity is neglected $\mu_d = 0$ and the dynamic viscosity is modelled using the Sutherland's law:

$$\eta(T) = \eta_{ref}\frac{T_{ref} + S}{T + S}\left(\frac{T}{T_{ref}}\right)^{3/2}\ . \tag{2.4}$$

The Sutherland's temperature S for air is 110.4 K. η_{ref} is the viscosity at a reference temperature T_{ref} (Schlichting & Gersten (2006)). Equation (2.1c) is the conservation of the internal energy, which can be derived from the conservation of the (specific) total energy:

$$E = e + \frac{u_i u_i}{2} \ , \tag{2.5}$$

see e.g. Poinsot & Veynante (2005), where $e_{kin} = {}^1\!/_2 \, (u_i u_i)$ is the (specific) kinetic energy. Two more expressions occur within equation (2.1c): the heat flux by conduction

$$q_j = -k \frac{\partial T}{\partial x_j} \tag{2.6}$$

and the dissipation function

$$\Phi = \tau_{ij} s_{ij} \ . \tag{2.7}$$

The thermal conductivity k can be expressed using the definition of the Prandtl number, see equation (1.7). Additionally, the ideal gas law

$$\frac{p}{\rho} = R_s T \tag{2.8}$$

is needed in order to close the set of equations. $R_s = c_p - c_v$ is the specific gas constant, which has a value of 287 J/(kg K) for air. The ratio of the specific heat capacities at constant pressure c_p respectively volume c_v used in this dissertation is $\kappa = c_p/c_v = 1.4$. The specific heat capacities are constant (perfect gas).

2.1.3 Characteristik formulation

The governing Navier-Stokes equations given in equation (2.1) can also be expressed in terms of pressure, velocity and entropy. Following Sesterhenn (2001), they can then be rewritten in a characteristic formulation:

$$\begin{aligned} \frac{\partial p}{\partial t} = &-\frac{\rho c}{2} \left(X^+ + X^- + Y^+ + Y^- + Z^+ + Z^- \right) \\ &+ \frac{p}{c_v} \left(\frac{\partial s}{\partial t} + X^s + Y^s + Z^s \right) \end{aligned} \tag{2.9a}$$

$$\frac{\partial u}{\partial t} = -\left[\frac{1}{2}\left(X^{+} - X^{-}\right) + Y^{u} + Z^{u}\right] + \frac{1}{\rho}\frac{\partial \tau_{1j}}{\partial x_j} \tag{2.9b}$$

$$\frac{\partial v}{\partial t} = -\left[X^{v} + \frac{1}{2}\left(Y^{+} - Y^{-}\right) + Z^{v}\right] + \frac{1}{\rho}\frac{\partial \tau_{2j}}{\partial x_j} \tag{2.9c}$$

$$\frac{\partial w}{\partial t} = -\left[X^{w} + Y^{w} + \frac{1}{2}\left(Z^{+} - Z^{-}\right)\right] + \frac{1}{\rho}\frac{\partial \tau_{3j}}{\partial x_j} \tag{2.9d}$$

$$\frac{\partial s}{\partial t} = -\left(X^{s} + Y^{s} + Z^{s}\right) + \frac{1}{\rho T}\left(-\frac{\partial q_i}{\partial x_i} + \Phi\right) \tag{2.9e}$$

with the following abbreviations:

$$\begin{aligned}
X^{\pm} &:= (u \pm c)\left(\frac{1}{\rho c}\frac{\partial p}{\partial x} \pm \frac{\partial u}{\partial x}\right)\\
Y^{\pm} &:= (v \pm c)\left(\frac{1}{\rho c}\frac{\partial p}{\partial y} \pm \frac{\partial v}{\partial y}\right)\\
Z^{\pm} &:= (w \pm c)\left(\frac{1}{\rho c}\frac{\partial p}{\partial z} \pm \frac{\partial w}{\partial z}\right)\\
X^{v} &:= u\frac{\partial v}{\partial x}\ ,\ X^{w} := u\frac{\partial w}{\partial x}\ ,\ X^{s} := u\frac{\partial s}{\partial x}\\
Y^{u} &:= v\frac{\partial u}{\partial y}\ ,\ Y^{w} := v\frac{\partial w}{\partial y}\ ,\ Y^{s} := v\frac{\partial s}{\partial y}\\
Z^{u} &:= w\frac{\partial u}{\partial z}\ ,\ Z^{v} := w\frac{\partial v}{\partial z}\ ,\ Z^{s} := w\frac{\partial s}{\partial z}
\end{aligned} \tag{2.10}$$

and the speed of sound

$$c = \sqrt{\kappa R_s T}\ . \tag{2.11}$$

This formulation has the following advantages (Sesterhenn (2001)): a) High order accuracy can be easily obtained, also at the boundaries. b) The implementation of boundary conditions is relatively easy, since they are consistent with the interior scheme. c) The decomposition of the domain into blocks is handled in the same manner and therefore, the formulation is well-suited for massive parallelisation on high performance computers.

2.2 Discretisation

2.2.1 Space discretisation

The spatial discretisation is realised using implicit (compact) finite difference schemes. These schemes can be written for an equally spaced grid in the interval from 0 to 1 with the dimensionless mesh width h as:

$$\sum_{r=-c}^{d} \beta_{j+q}\, q'_{j+p} = \frac{1}{h} \sum_{p=-a}^{b} \alpha_{j+p}\, q_{j+p} \ . \tag{2.12}$$

q'_j is the first derivative of the variable q_j at the location x_j. a, b, c and d are the number of used adjacent points (left respectively right). The coefficients α and β are chosen according to the desired order, the consistency condition and the desired properties of the discretisation. The advantage of these schemes is that they offer a high accuracy while using a small stencil (number of neighbouring points). The implicit system can be efficiently solved by means of a LU decomposition, followed by one forward and one backward elimination (Schulze (2013)).

In our case, the inviscid (hyperbolic) parts of the Navier-Stokes equations are decomposed into plane characteristic waves ($X^\star, Y^\star, Z^\star$), as shown in section 2.1.3. These convective parts are discretised with the fifth order upwind scheme CLUD of Adams & Shariff (1996). The direction of the waves is taken into account. The upwind scheme introduces dissipation for high wavenumbers. This stabilises the simulation in case some areas of the domain are (temporary) slightly under-resolved. For strongly under-resolved simulations, an additional filter has to be applied after a certain number of time steps, which was not done within this work.

The remaining diffusive terms (heat flux and friction terms) are of parabolic nature and are discretised by a central scheme of sixth order, as described by Lele (1992). Central schemes have no numerical dissipation. Both, the 5th order upwind and the 6th order central scheme are characterised by a low dispersion error. The coefficients used can be found in the mentioned articles.

2.2.2 Parallelisation

An appropriate resolution of an impinging jet with a Reynolds number of 8000 requires more than one billion grid points. Considering roughly a quarter million time steps necessary to obtain statistical quantities, the resulting computational load reaches multiple million core hours. It is obvious that a massive parallelisation is necessary in order to obtain the results *already* after some month instead of after hundreds of years using only one core.

The computational task is partitioned between a huge number of processes. In this project, up to $2^{14} = 16384$ cores have been used. Each process solves the Navier-Stokes equations for a fractional part of the domain (block). This approach is called domain decomposition, see Eidson & Erlebacher (1995). In order to calculate derivatives using compact finite differences, the data of the entire direction is required. Consequently, the decomposed domain has to be rearranged so that each process receives grid lines that span the entire domain in the particular direction. The total number of grid points per process remains constant and is typically between 32^3 and 64^3. Figure 2.1 exemplary shows the transformation from the original decomposition to the decomposition used for the calculation of derivatives in x-direction. The inter-process communication is managed via MPI libraries.

All computations were run on the machines of the High Performance Computing Center in Stuttgart (HLRS). The latest system called Hazelhen is a CRAY XC40 machine and currently the 9th biggest supercomputer on the world[1]. This system replaced the former CRAY XE6 machine named

---

[1] According to the June 2016 list of http://www.top500.org

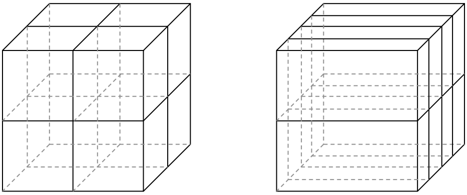

Figure 2.1: Domain decomposition of a three-dimensional domain. Left: original decomposition, right: transformed decomposition for the calculation of derivatives in x-direction.

Hermit.

Figure 2.2 shows nearly perfect linear scaling up to 16384 cores on Hazelhen. The speed up is the ratio of wall times, comparing the run on i cores to the run with the lowest number of cores. If the total number of grid points n is kept constant, the measurement is referred to as strong scaling. The number of grid point per core n/i varies. The scaling was made for the case of an impinging jet. In order not to distort the measurement, input and output was turned off. Each node of the system contains 24 cores and is equipped with 128 GB of memory. The required memory by the simulation determines the minimal number of nodes and consequently the minimally required cores. For this reason, a measurement with less then $2^9 = 512$ cores is not possible. Weak scaling provides an alternative assessment method. Here, the number of grid points per core is kept constant and the total number of cores varies. This enables to span a larger measurement range.

Using auto-vectorisation, the efficiency with 16384 cores is 102% (strong) respectively 83% (weak). Grids with 512^3 points are typically parallelised on $16^3 = 4096$ cores and grids with 1024^3 points are run on $i = 32 \times 16 \times 16 = 8192$ or $i = 32 \times 32 \times 16 = 16384$. Detailed run times can be found in table 2.1.

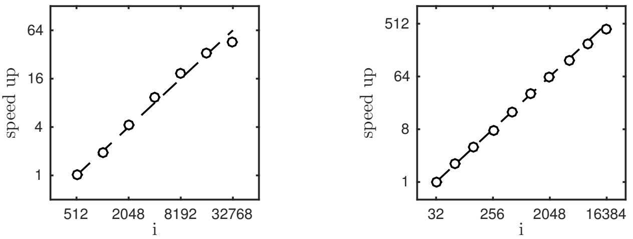

(a) Simulations run with $n = 1024^3$

(b) Simulations run with $n/i = 64^3$

Figure 2.2: Strong (a) and weak (b) scaling of the code on CRAY XC40 (Hazelhen). n and i denote the total number of grid points and used cores respectively.

2.2.3 Time discretisation

The choice of the time integration scheme is crucial for the accuracy and efficiency of the code. In this study, a 4th order five stage explicit Runge-Kutta scheme RK4(3)5[2R+], as described by Kennedy et al. (2000), is used. The spatially discretised compressible Navier-Stokes equations can be written as an initial value problem:

$$\frac{dU}{dt} = F\left(t, U\left(t\right)\right)\ ,\ U\left(t=0\right) = U_0\ , \tag{2.13}$$

where $U = \left(p, u, v, w, s\right)^{\top}$ and F contains the inviscid, viscous and body force terms. The current time step is denoted by n. The time interval between n and $n+1$ is $\Delta t = t^{(n+1)} - t^{(n)}$. The flow field at $t^{(n+1)}$ is obtained by:

$$y_i = U^{(n)} + \Delta t \sum_{j=1}^{i-1} a_{ij} F\left(t^{(n)} + c_j \Delta t, y_j\right)\ ,\ 1 \leq i \leq m \tag{2.14a}$$

i	$(n/i)^{1/3}$	wall time per time step [s]	speedup	ideal speedup	efficiency
512	128	166	1.00	1	1.00
1024	102	85.6	1.94	2	0.97
2048	81	39.2	4.23	4	1.06
4096	64	17.9	9.28	8	1.16
8192	51	9.1	18.3	16	1.14
16384	40	5.1	32.6	32	1.02
32768	32	3.7	44.9	64	0.70

i	n	wall time per time step [s]	speedup	ideal speedup	efficiency
32	8.4×10^6	16.7	1.00	1	1.00
64	1.7×10^7	16.6	2.02	2	1.01
128	3.4×10^7	17.0	3.93	4	0.98
256	6.7×10^7	17.1	7.84	8	0.98
512	1.3×10^8	17.1	15.7	16	0.98
1024	2.7×10^8	17.0	31.4	32	0.98
2048	5.4×10^8	17.2	62.1	64	0.97
4096	1.1×10^9	17.9	120	128	0.94
8192	2.1×10^9	18.5	231	264	0.90
16384	4.3×10^9	20.1	425	512	0.83

Table 2.1: Scaling of the code on CRAY XC40 (Hazelhen). Upper part: strong scaling, simulations run with $n = 1024^3$. Lower part: weak scaling, simulations run with $n/i = 64^3$. n and i denote the total number of grid points respectively the number of used cores.

$$U^{(n+1)} = U^{(n)} + \Delta t \sum_{j=1}^{m} b_j F\left(t^{(n)} + c_j \Delta t, y_j\right) \,, \tag{2.14b}$$

where m is the number of stages and y_i are intermediate values. The corresponding Butcher coefficients a_{ij}, b_j and c_j can be found in Kennedy et al. (2000).

2.2.4 Shock treatment

In under-expanded supersonic impinging jets, shocks appear in the free jet as well as in front of the impinging plate (standoff shocks). In Schulze (2013), an approximation concerning the shock width ($\delta_s \sim Re^{-1}$) is given, based on the theory of Taylor (1910) and is compared to the Kolmogorov length scale ($l_\eta \sim Re^{-3/4}$). It is shown that for $Re \lesssim 10^5$ the shock width is larger than the Kolmogorov length scale and for $Re \gtrsim 10^5$ it is the opposite case. However, this consideration can give only a rough estimation. For $Re = 8000$, l_η and δ_s lie roughly in the same order of magnitude, whereby $\delta_s > l_\eta$ holds. For the DNS we use a grid that resolves the Kolmogorov scale ($\Delta x \approx l_\eta$). If the shock width is in the same order of magnitude as l_η, the shock is resolved only with a few grid points. Depending on the strength of the shock, these points may not be sufficient to handle the huge gradients and Gibbs oscillations in the vicinity of the shock can appear.

Figure 2.3 shows a snapshot of the supersonic impinging jet with $Re = 8000$ (middle: density gradient) and the pressure at the jet axis (left). Within the shock diamonds of the free jet, the pressure is smooth and the gradients can be resolved by the numerical grid.

More challenging are the standoff shocks. In this snapshot, two standoff shocks are present at $y/D = 0.85$ and $y/D = 0.58$ where the pressure increases by 0.53 respectively 0.35 bar. The shocks are resolved with six respectively five grid points. This is not enough to handle the huge gradients within the standoff shock. Hence, a filter needs to be applied for standoff shocks.

In this thesis, an adaptive shock-capturing filter developed by Bogey et al. (2009) is used. The filter is written in a conservative form to accurately describe the propagation of shocks. The flow field U at grid point i is second-order filtered by

$$U_i^{sc} = U_i - \left(\sigma_{i+\frac{1}{2}}^{sc} D_{i+\frac{1}{2}}^{sc} - \sigma_{i-\frac{1}{2}}^{sc} D_{i-\frac{1}{2}}^{sc} \right) \, , \tag{2.15}$$

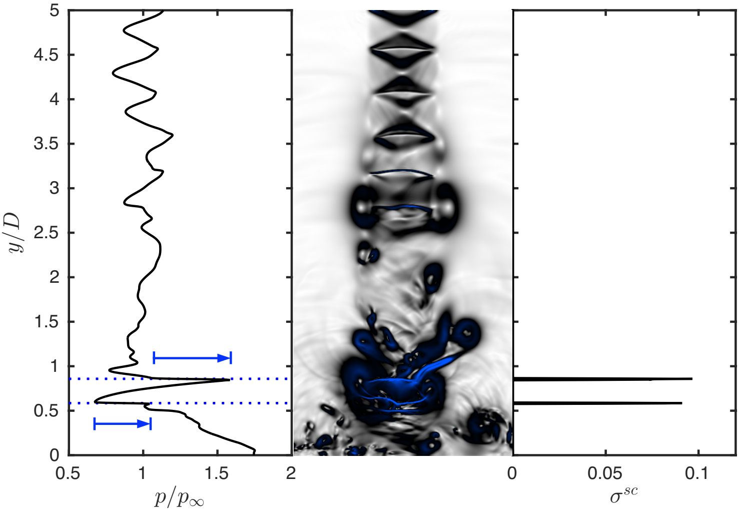

Figure 2.3: Application of the shock-capturing filter to the impinging jet. Left: pressure at the jet axis. The two arrows and dashed lines indicate the standoff shocks. Middle: instantaneous flow field (density gradient, white $|\nabla\rho|\, D/\rho_\infty = 0$, black: $|\nabla\rho|\, D/\rho_\infty = 1$, blue: $|\nabla\rho|\, D/\rho_\infty = 7$). Right: filter strength σ^{sc}.

where $D^{sc}_{i+\frac{1}{2}}$ and $D^{sc}_{i-\frac{1}{2}}$ are the damping functions and $\sigma^{sc} \in [0,1]$ is the filtering strength that is automatically adapted by the flow conditions. Therefore, a shock sensor based on the high-pass filtered dilatation is compared to a threshold value. For in depth description of the filter, see Bogey et al. (2009).

To get back to the impinging jet, the shock-capturing filter is applied for the impinging jet in a way that it is allowed to be active only in the region where standoff shocks are expected. Especially the impinging plate has to be excluded, since large velocity gradients appear at the wall. These can be erroneously detected as shock by the filter. Figure 2.3 (right) shows that the two standoff shocks are successfully detected by the procedure. The filter strength is zero in the entire domain, except at the locations, where standoff shocks occur.

2.3 Computational domain

2.3.1 Boundary conditions

The implementation of boundary conditions for the Navier-Stokes equations in characteristic formulation (section 2.1.3) is straightforward. The direction from which information comes from is known in the entire domain, including the boundaries (Sesterhenn (2001)). The waves entering the domain are set in order to achieve the desired conditions. For the simulation of impinging jets, we basically need three conditions: a wall, an inlet and a non-reflecting boundary, which is a kind of outlet that allows return flow, but does not reflect acoustic waves. The isothermal wall and the inlet can be described with one set of equations, but one has to distinguish between the sub- and the supersonic case.

Wall with subsonic inlets. In Wilke & Sesterhenn (2015a), a set of equations was derived so as to consistently describe a boundary consisting of an isothermal wall and one or multiple subsonic inlets. For clarity, the equations are again expressed for a Cartesian grid and refer to the upper boundary. The unknown waves Y^u and Y^w in equations (2.9b) and (2.9d) can be derived directly by imposing the boundary-parallel velocity derivatives $\frac{\partial u}{\partial t}$ and $\frac{\partial w}{\partial t}$ in the boundary plane. In the subsonic case, the waves Y^- and Y^s enter the domain and therefore have to be set. Using the temporal derivative of the total temperature T_t

$$\frac{\partial T_t}{\partial t} = \frac{\kappa - 1}{\kappa} \frac{T}{p} \frac{\partial p}{\partial t} + \frac{T}{c_p} \frac{\partial s}{\partial t} + \frac{1}{c_p} \left(u \frac{\partial u}{\partial t} + v \frac{\partial v}{\partial t} + w \frac{\partial w}{\partial t} \right) , \tag{2.16}$$

(2.9a) ,(2.9c), (2.9e) and (2.16) form a set of four equations for six unknowns: $\frac{\partial p}{\partial t}$, $\frac{\partial s}{\partial t}$, $\frac{\partial T_t}{\partial t}$, $\frac{\partial v}{\partial t}$, Y^- and Y^s ($\frac{\partial u}{\partial t}$ and $\frac{\partial w}{\partial t}$ are already fixed). Specifying $\frac{\partial v}{\partial t}$ and $\frac{\partial T_t}{\partial t}$ delivers the desired equations that allow a very easy switch between wall and inlet:

$$Y^u = -\frac{\partial u}{\partial t} - \frac{1}{2}\left(X^+ - X^-\right) - Z^u + \frac{1}{\rho}\frac{\partial \tau_{1j}}{\partial x_j} \tag{2.17a}$$

$$Y^w = -\frac{\partial w}{\partial t} - X^w - \frac{1}{2}\left(Z^+ - Z^-\right) + \frac{1}{\rho}\frac{\partial \tau_{3j}}{\partial x_j} \tag{2.17b}$$

$$Y^- = Y^+ + 2\left(\frac{\partial v}{\partial t} + X^v + Z^v - \frac{1}{\rho}\frac{\partial \tau_{2j}}{\partial x_j}\right) \tag{2.17c}$$

$$\begin{aligned} Y^s = &- \left(X^s + Z^s\right) + \frac{\kappa}{\rho T}\left(-\frac{\partial q_i}{\partial x_i} + \Phi\right) - \frac{c_p}{T}\frac{\partial T_t}{\partial t} + \frac{u}{T}\frac{\partial u}{\partial t} + \frac{v}{T}\frac{\partial v}{\partial t} \\ &+ \frac{w}{T}\frac{\partial w}{\partial t} - \frac{c}{2T}\left(X^+ + X^- + Y^+ + Y^- + Z^+ + Z^-\right) . \end{aligned} \tag{2.17d}$$

At the wall, the temporal derivatives of all three velocity components and the total temperature are simply zero. Applying a zero-velocity initial condition, the velocity remains zero and the (total) temperature remains constant at the wall for the entire computation. The wall is fully acoustically reflective. At the inlet, those derivatives are set in such a way that the intentional temporal progressions occur. In the present cases, the velocity derivative is set such that a given total pressure sets up.

Wall with supersonic inlets. In the supersonic case, also the wave Y^+ is now entering the domain. Therefore, an additional condition has to be given. Imposing $\frac{\partial p}{\partial t}$ offers the opportunity to control the adaptation of the jet to under-, perfectly or over-expanded. The waves Y^u and Y^w are equal to the subsonic case. Y^+, Y^- and Y^s read:

$$\begin{aligned} Y^+ = &-\frac{1}{\rho}\frac{\partial p}{\partial t} - \frac{\partial v}{\partial t} - \frac{1}{2}\left(X^+ + X^- + Z^+ + Z^-\right) \\ &+ \frac{\kappa - 1}{\rho}\sigma - \left(X^v + Z^v\right) + \frac{1}{\rho}\frac{\partial \tau_{2j}}{\partial x_j} \end{aligned} \tag{2.18a}$$

$$Y^- = -\frac{1}{\rho}\frac{\partial p}{\partial t} + \frac{\partial v}{\partial t} - \frac{1}{2}\left(X^+ + X^- + Z^+ + Z^-\right)$$

$$+\frac{\kappa-1}{\rho}\left(-\frac{\partial q_i}{\partial x_i}+\Phi\right)+\left(X^v+Z^v\right)-\frac{1}{\rho}\frac{\partial \tau_{2j}}{\partial x_j} \tag{2.18b}$$

$$Y^s=-\frac{c_p}{T}\frac{\partial T_t}{\partial t}+\frac{c_p}{p}\frac{\kappa-1}{\kappa}\frac{p}{t}+\frac{u}{T}\frac{\partial u}{\partial t}+\frac{v}{T}\frac{\partial v}{\partial t}+\frac{w}{T}\frac{\partial w}{\partial t}$$

$$-\left(X^s+Z^s\right)+\frac{1}{\rho T}\left(-\frac{\partial q_i}{\partial x_i}+\Phi\right)\ . \tag{2.18c}$$

Non-reflecting plane. In order to accurately capture noise generated by the impinging jet, the subsonic in-/outflow boundaries must not reflect any outgoing acoustic waves. This is achieved by simply setting the ingoing waves to zero. Those non-reflecting boundaries have to be located far away from the intense turbulent flow, so that aerodynamic fluctuations can be neglected. For the left plane normal to the x-axis the conditions are:

$$X^v=X^w=X^+=X^s=0\ . \tag{2.19}$$

Distinction between wall and inlet. Isothermal walls and subsonic inlets are described with one set of equations (2.17). The distinction is made by the choice of $\frac{\partial u}{\partial t}$, $\frac{\partial v}{\partial t}$, $\frac{\partial w}{\partial t}$ and $\frac{\partial T_t}{\partial t}$. This method can be used to set fully turbulent or laminar inflow conditions. In this thesis, the second option is used. Consequently, the boundary-parallel velocity components for the wall as well as for the inlet remain zero with $\frac{\partial u}{\partial t}=\frac{\partial w}{\partial t}=0$, since the initial velocity is zero in the entire domain. The boundary-normal velocity component and therewith the position of the nozzle exit is set by multiplying the corresponding velocity derivative with a spatial function $f_x(r,\theta)$. Walls are obtained for $f_x=0$ and inlets for $f_x=1$. This treatment makes it very easy to define one or multiple inlet areas (nozzle exits) by adjusting f_x. The location of a single nozzle is defined using a hyperbolic tangent profile with a thin laminar annular shear layer described by a thickness function b, see Wilke & Sesterhenn (2015a):

$$f_x^{(n)}(r,\theta)=\frac{1}{2}-\frac{1}{2}\tanh\left[\left(\frac{r}{D}-\frac{D}{2}+\tanh^{-1}(1-g)\right)b^{(n)}(\theta)\right]\ . \tag{2.20}$$

The parameter g moves the shear layer adjacent to the wall of the artificial nozzle. A similar profile has been used by Freund (2001) for free jets with $Ma = 0.9$ and $Re = 3600$. He applied random perturbations of b in order to accelerate the transition of the jet. In agreement with his investigation, the impinging jet with $Re = 3300$ remained laminar and symmetric for thousands of time steps, unless a perturbation is added:

$$\begin{aligned} b^{(n)}(\theta) = e^{-\tau} b^{(n-1)}(\theta) + \left(1 - e^{-\tau}\right) \cdot \\ \cdot \left[b_0 + \frac{1}{N} \sum_{n=1}^{N} c_1^{(n)} \cos\left(2\pi \frac{v_\infty}{D} c_2^{(n)} t + c_3^{(n)}\right) \cos\left(\theta + c_4^{(n)}\right) \right] . \end{aligned} \tag{2.21}$$

The time correlation of the thickness function at time step n to the previous time step $n-1$ is achieved by the introduction of a decay function e^{τ}. c_1, c_2, c_3 and c_4 are random variables. This approach is a combination of those by Freund (2001) and Davidson (2007). The used parameters are: $b_o = 26.47$, $g = 10^{-2}$, $N = 100$ and $\tau = 10^{-2}$. The defined ranges of the random variables are: $0 \leq c_1 \leq 20$, $0 \leq c_2 \leq 20$, $0 \leq c_3 \leq 2\pi$, $0 \leq c_4 \leq 2\pi$. The resulting random distribution of the thickness function b has the following properties: $\max\left[\Delta b\right]/b_o = \max\left[b^{(n)} - b^{(n-1)}\right]/b_o = 8.87\ 10^{-4}$, $\mathrm{std}\left[\Delta b / b_o\right] = 1.30\ 10^{-4}$ and $26.31 \leq b \leq 26.63$.

The profile f_x has a radial displacement

$$\delta^* = \frac{D - D^*}{2} \tag{2.22}$$

of $\delta^* = 0.1 \cdot D$, based on the average flow field. The effects due to the boundary layer displacement are not taken into account while computing dimensionless numbers, such as Re and Sr. For those numbers, the diameter D and not the displaced diameter D^*

$$D^* = \sqrt{\frac{4}{\pi} \frac{\dot{m}}{\rho v}} \Bigg|_{in} \tag{2.23}$$

is used. $\dot{m}$, ρ and v are the mass flow, density and velocity in the axial direction at the inlet. Changing the reference length to D^* effects the non-dimensional frequencies. This issue has to be considered when comparing e.g. sound spectra and Nusselt numbers to experimental data or to simulations carried out with a geometrically modelled nozzle. Also the nozzle-to-plate distance h/D is affected.

One more issue has to be considered in the supersonic case: The spatial function f_x necessarily leads to the occurrence of subsonic flow within the boundary layer of the artificial nozzle. Consequently, a procedure has to be included in the code that chooses the correct equations (either sub- or supersonic) for each point at the boundary. The wall is necessarily subsonic, and therefore $\frac{\partial p}{\partial t}$ must not be given there.

The impinging jet is computed on a cuboid. The orifice plate is realised by an isothermal wall including the artificial nozzle (inlet). For the impinging plate, the same boundary condition is used, but f_x is zero at the entire boundary. The walls are fully acoustically reflective. The remaining four boundary conditions are non-reflecting. The computational domain is shown in figure 2.4.

2.3.2 Sponge

As described in the previous section, the ingoing waves of the non-reflecting boundary condition are simply set to zero. A problem arises when this boundary is located within a recirculating flow, as in the case of the impinging jet. Fluid entering the domain requires the placement of the respective waves. Since the recirculating flow is laminar and of very low velocity $(\max(u)/v_\infty \lesssim 4\%)$, the non-reflecting boundary can be used when a sponge region is applied additionally. A sponge smoothly forces the values of pressure, velocity and entropy to reference values $U_{ref} = (p, u, v, w, s)^\top_{ref}$. In order to do so, an additional source term

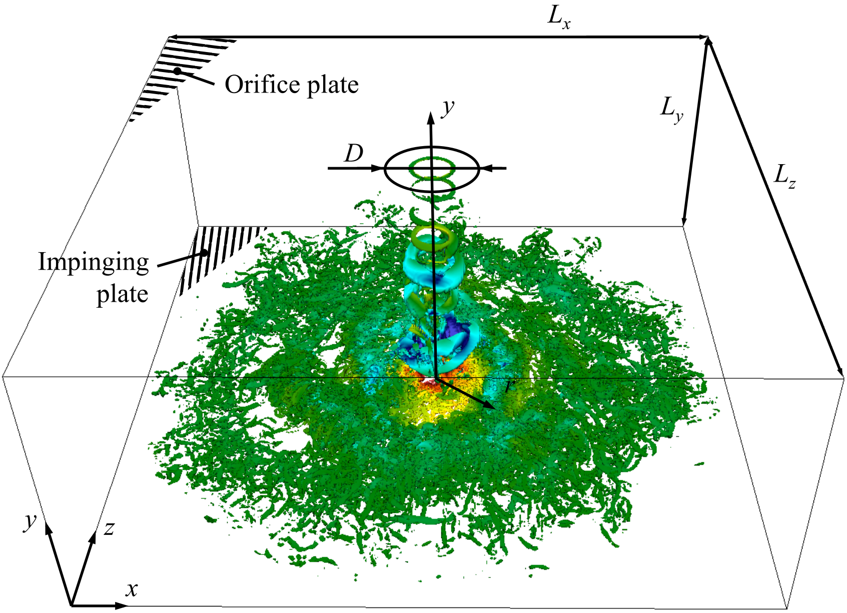

Figure 2.4: Computational domain: 3D countour plot of a supersonic impinging jet with $Ma = 1.11$ and $Re = 8000$ at $QD^2/v_\infty^2 = 1.7$, coloured with pressure ($0.6 \leq p/p_\infty \leq 1.5$, blue to red).

is included in the right-hand side of the Navier-Stokes equations:

$$\frac{dU}{dt} = F(U) - \tau_s \sigma_s (U - U_{ref}) \ . \tag{2.24}$$

The function

$$\sigma_s(r) = \frac{1}{2} + \frac{1}{2}\mathrm{erf}\left(\frac{2r}{L_x}L_e + f_1 - L_e\right) \tag{2.25}$$

with

$$L_e = \frac{L_x}{2L_{sp}}(f_1 - f_2) \tag{2.26}$$

defines the area where the sponge is active. In the case of the impinging

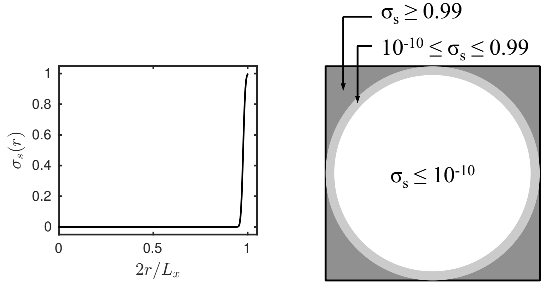

Figure 2.5: Left: sponge function σ_s, right: illustration of σ_s within the computational domain (view from the top).

jet, σ_s depends on the radius

$$r = \sqrt{(x - x_c)^2 + (z - z_c)^2} \tag{2.27}$$

and is shown in figure 2.5. The positional parameter x_c defines the centre of the inlet whereas L_x is the length of the domain in x-direction. The same holds for y and z. The parameters $L_{sp} = 0.5$, $f_1 = \mathrm{erf}^{-1}(0.99)$, $f_2 = \mathrm{erf}^{-1}\left(-1 + 10^{-10}\right)$ are chosen so that σ_s reaches a value of 10^{-10} at a radial position of $r/D = 5.5$ and 0.99 at $r/D = 6$. This function has to be smooth, since otherwise acoustic reflections can occur. Equation (2.25) as well as τ_s and u_{ref} are chosen similary to Schulze (2013). τ_s defines the strength of the source term. In this work, a value of 500 is used. Please note that in this context p_{ref} is different from the reference pressure used for the computation of the sound pressure level. The reference values U_{ref} were obtained by a preliminary LES on a greater domain (average values). However, the pressure as well as the circumferential velocity can be set to p_∞ respectively zero. The flow solution within the sponge region has no physical meaning and should be cut for the analysis of the flow.

Besides the treatment of the recirculation, a sponge offers a second advantage. The forcing of the flow variables towards reference values destroys vortices before they can leave the domain. This avoids artificial noise that is generated when a vortex or vortex pair is cut by the boundary condition. In case of the impinging jet, large and medium-scale vortices are crumbled even before they come close to the boundary (until $r/D \lesssim 4$).

2.3.3 Grid stretching

A grid stretching is applied for all three directions. The purpose is to achieve a higher resolution in the areas of the domain where the dissipation rate ϵ is high, see equation (4.1). The first simulation was carried out with $Re = 3300$ and $Ma = 0.78$ (#5 according to table 2.3). In order to refine the shear layer of the free jet region (x- and z-direction), the grid stretching function of Schulze (2013) that was successfully applied for free jets, was used:

$$\begin{aligned} B &= \frac{1}{2\tau_x} \ln \left[\frac{1 + \left(e^{\tau_x} - 1\right) x_c^*}{1 + \left(e^{-\tau_x} - 1\right) x_c^*} \right] \\ x &= x_c^* \left(\frac{\sinh\left[\tau_x \left(\xi - B\right)\right]}{\sinh\left(\tau_x B\right)} + 1 \right) . \end{aligned} \tag{2.28}$$

The equidistant grid $\xi \in [0, 1]$ is transformed into the stretched grid $x \in [0, 1]$. In order to set the size of the domain, x has then to be multiplied with the length of the domain L_x. The parameters x_c^* and τ_x control the centre of the refinement respectively its strength. All simulations carried out within this work use $x_c^* = 0.5$. For simulation #5, $\tau_x = 3$ was chosen. The analysis of this simulation shows that additionally to the free jet shear layer, also the area with increased turbulence in the wall jet $r/D \lesssim 3$ needs to be refined. Consequently, a new grid stretching was developed and applied for all other simulations. This stretching involves multiple steps and can be implemented in the code as follows:

```
1: $x \leftarrow e^{(\xi - x_c^*)^{\tau_x}} - 1$
```

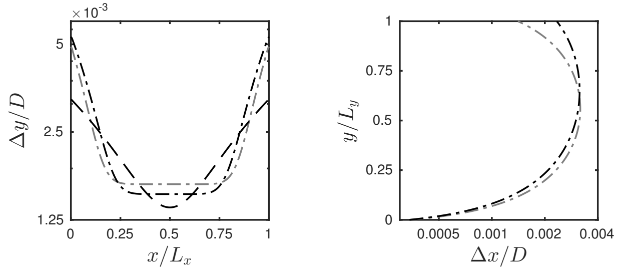

Figure 2.6: Grid spacings due to different grid stretchings for 512 points.
Left: x- and z-direction, –·–·: equation (2.29) $\tau_x = 10, \iota_x = 3, x_c^* = 0.5$, –·–·: equation (2.29) $\tau_x = 8, \iota_x = 3.5, x_c^* = 0.5$, — —: equation (2.28) $\tau_x = 3, x_c^* = 0.5$.
Right: y-direction equation (2.30), –·–·: $\tau_y = 2.75, y_c = 0.72$, –·–·: $\tau_y = 2.34, y_c = 0.83$.

$$2\text{: } x \leftarrow \frac{x}{\max(x)}$$

$$3\text{: } x \leftarrow 1 + (\iota_x - 1)\,x$$

$$4\text{: } x \leftarrow \int\limits_{\xi=0}^{1} x(\xi)\,d\xi$$

$$5\text{: } x \leftarrow \frac{x}{\max(x)}\,, \tag{2.29}$$

where τ_x and ι_x control the strength and the extent of the refinement. τ_x has to be even if greater one. Values of $(\tau_x, \iota_x) = (8, 3.5)$ or $(10, 3)$ were used and can be recommended. A confrontation of the stretchings according to equation (2.28) and equation (2.29) is shown in figure 2.6.

For the wall-normal direction y, the grid needs to be refined at the impinging plate ($y = 0$) in order to allow an appropriate resolution of the boundary layer. The upper plate does not need to be resolved as fine as the impinging plate, since the velocity due to recirculation as a consequence of entrainment is low and the flow is laminar. However, it is reasonable to use a function that refines both walls when the centre y_c^* is moved closer to the upper plate. The equidistant grid $\eta \in [0, 1]$ is transformed into $y \in [0, 1]$ by:

$$\begin{aligned} B &= \frac{1}{2\tau_y} \ln \left[\frac{1 + \left(e^{\tau_y} - 1\right) y_c^*}{1 + \left(e^{-\tau_y} - 1\right) y_c^*} \right] \\ y &= \frac{\tanh\left[\tau_y \left(\eta - B\right)\right] + \tanh\left(\tau_y B\right)}{\tanh\left[\tau_y \left(1 - B\right)\right] + \tanh\left(\tau_y B\right)} \; . \end{aligned} \tag{2.30}$$

Using $\tau_y = 0.72$ it turned out that the upper wall does not need to be refined at all. Consequently, τ_y has been changed to 0.83, which gives the optimal distribution of this function for a given grid spacing adjacent to the impinging plate. The small refinement close to the orifice plate does not significantly increase the computational load ($< 2\%$). All described refinements lead to a smooth and small change of the mesh spacing, which is lower than 1%, based on 512 grid points per direction and the given values of the parameters.

2.3.4 Parameters

Within this thesis, three sub- and three supersonic simulations are analysed. The simulations are numbered with #1 to #6. Influences of three parameters are described within this thesis: a) Mach number: #(4,5,6), b) Reynolds number: #(2,3) and #(5,6) and c) a heated environment #(1,2). Only simulations grouped in braces #(..,..) differ within a single parameter and can be compared. An additional simulation (#7) with a pulsed inlet was carried out. Common parameters are given in table 2.2 and specific parameters are shown in table 2.2.

R_s [J/(kg K)]	κ [−]	Pr [−]	p_∞ [Pa]	$T_{t,in}$ [K]	$L_x \times L_y (= h) \times L_z$ [−]
287	1.4	0.71	10^5	293.15	$12D \times 5D \times 12D$

Table 2.2: Common geometrical and physical parameters for all simulations. R_s, κ, Pr, p_∞, $T_{t,in}$ and L_x, L_y, L_z denote specific gas constant, ratio of specific hats, Prandtl number, ambient pressure, total temperature at the inlet and the size of the domain.

N°	$p_{t,in}/p_\infty$ [−]	Ma [−]	$T_\infty = T_w$ [K]	Re [−]
#1	2.15	1.106	373.15	3300
#2	2.15	1.106	293.15	3300
#3	2.15	1.106	293.15	8000
#4	1.12	0.408	373.15	3300
#5	1.50	0.784	373.15	3300
#6	1.50	0.784	373.15	8000
#7	0 − 1.50	0 − 0.784	373.15	0 − 6600
N°	grid points	max. y_w^+ [−]	Δx, Δz [D]	Δy [D]
#1	$512 \times 512 \times 512$	0.67	0.0199−0.0588	0.0017−0.0159
#2	$512 \times 512 \times 512$	0.77	0.0199−0.0588	0.0017−0.0159
#3	$1024 \times 1024 \times 1024$	1.02	0.0099−0.0296	0.0012−0.0072
#4	$512 \times 512 \times 512$	0.62	0.0184−0.0636	0.0017−0.0159
#5	$512 \times 512 \times 512$	0.63	0.0165−0.0388	0.0017−0.0159
#6	$1024 \times 1024 \times 1024$	0.58	0.0099−0.0296	0.0008−0.0078
#7	$1024 \times 1024 \times 1024$	0.35	0.0093−0.0307	0.0008−0.0078

Table 2.3: Specific geometrical and physical parameters of the simulation. $p_{t,in}$, p_∞, Ma, T_∞, T_w, Re, y_w^+ and $\Delta_{x,y,z}$ denote total pressure at the inlet, ambient pressure, Mach number, ambient and wall temperature, Reynolds number, the dimensionless wall distance at the wall and the grid width in x-, y- and z-direction

3 Methods for flow analysis

3.1 Averaged equations

3.1.1 Averaged governing equations

For engineering problems, a much faster and less expensive approach than DNS is needed. The knowledge of the statistically averaged flow field is sufficient for many applications. Thus, the common approach to find a solution for a flow problem involves an averaging of the governing equations (2.1). It is common practice to work with two different averages simultaneously (Friedrich (1999)). The quantities pressure and density are usually decomposed into:

$$\rho = \overline{\rho} + \rho' \; , \; p = \overline{p} + p' \; . \tag{3.1}$$

The fluctuation is denoted with one apostrophe ($\star'$) and the average with an overbar ($\overline{\star}$). This kind is called Reynolds-average. Temperature, internal energy and velocity by contrast are typically decomposed into a Favre-average ($\widetilde{\star}$) and the corresponding fluctuation ($\star''$):

$$T = \widetilde{T} + T'' \; , \; e = \widetilde{e} + e'' \; , \; u_i = \widetilde{u_i} + u_i'' \; . \tag{3.2}$$

It is also possible to use both kinds of averages for a single variable, e.g. for the temperature and and velocity components. The mass-weighted

(Favre-) averages are defined as:

$$\widetilde{\alpha} = \frac{\overline{\rho\alpha}}{\overline{\rho}} \ . \tag{3.3}$$

The average of a variable α can be obtained either by ensemble averaging over an infinite number of snapshots N:

$$\overline{\alpha}^e = \lim_{N\to\infty} \frac{1}{N} \sum_{n=1}^{N} \alpha^{(n)} \ , \tag{3.4}$$

or by time-averaging over a time interval Δt:

$$\overline{\alpha}^t = \frac{1}{\Delta t} \int\limits_0^{\Delta t} \alpha \ dt \ . \tag{3.5}$$

An additional averaging in space is possible, if symmetry planes or axes exist. The statistically averaged Navier-Stokes equations are obtained by simply Reynolds-averaging each equation entirely, e.g. the momentum conservation becomes:

$$\overline{\frac{\partial \rho u_i}{\partial t} + \frac{\partial \rho u_i u_j}{\partial x_j}} = \overline{-\frac{\partial p}{\partial x_i} + \frac{\partial \tau_{ij}}{\partial x_j}} \ . \tag{3.6}$$

Following Friedrich (1999), we assume that the averaging procedure commutes with differentiation, is linear and preserves constants. Furthermore, the following computation rules

$$\overline{\alpha'} = 0 \ , \ \overline{\alpha''} \text{ gen. } \neq 0 \ , \overline{\rho\alpha''} = 0 \tag{3.7a}$$

$$\overline{\alpha\beta} = \overline{\alpha}\,\overline{\beta} + \overline{\alpha'\beta'} \tag{3.7b}$$

$$\overline{\rho\alpha\beta} = \overline{\rho}\,\widetilde{\alpha}\,\widetilde{\beta} + \overline{\rho\alpha''\beta''} \tag{3.7c}$$

$$\overline{\alpha''} = \overline{\alpha} - \widetilde{\alpha} \tag{3.7d}$$

can be derived as shown in appendix A.1.1. α and β are arbitrary variables and ρ is the density. The application of these rules to equation (2.1) leads to the averaged governing equations:

$$\frac{\partial \overline{\rho}}{\partial t} + \frac{\partial \overline{\rho}\, \widetilde{u_j}}{\partial x_j} = 0 \tag{3.8a}$$

$$\frac{\partial \overline{\rho}\, \widetilde{u_i}}{\partial t} + \frac{\partial \overline{\rho}\, \widetilde{u_i}\, \widetilde{u_j}}{\partial x_j} = -\frac{\partial\, \overline{\rho u''_i u''_j}}{\partial x_j} - \frac{\partial \overline{p}}{\partial x_i} + \frac{\partial \overline{\tau_{ij}}}{\partial x_j} \tag{3.8b}$$

$$\begin{aligned} \frac{\partial \overline{\rho}\, \widetilde{e}}{\partial t} + \frac{\partial \overline{\rho}\, \widetilde{e}\, \widetilde{u_j}}{\partial x_j} = -\frac{\partial \overline{q_j}}{\partial x_j} - \frac{\partial\, \overline{\rho e'' u''_j}}{\partial x_j} - \overline{p}\frac{\partial \overline{u_j}}{\partial x_j} - \overline{p'\frac{\partial u'_j}{\partial x_j}} \\ + \overline{\tau_{ij}}\, \overline{s_{ij}} + \overline{\tau'_{ij} s'_{ij}}\ , \end{aligned} \tag{3.8c}$$

with

$$\overline{\tau_{ij}} = 2\,\overline{\eta}\left(\overline{s_{ij}} - \frac{1}{3}\,\overline{s_{kk}}\delta_{ij}\right) + 2\left(\overline{\eta' s'_{ij}} - \frac{1}{3}\,\overline{\eta' s'_{kk}}\delta_{ij}\right) \tag{3.9a}$$

$$\overline{q_j} = -\,\overline{k}\frac{\partial \overline{T}}{\partial x_j} - \overline{k'\frac{\partial T'}{\partial x_j}}\ . \tag{3.9b}$$

The terms are transformed so that only averages of single variables and not of products occur. Consequently, new terms arise that need to be modelled (closure problem):

$$\begin{gathered} \overline{\rho u''_i u''_j}\ \ ,\ \overline{\eta' s'_{ij}},\ \overline{k'\frac{\partial T'}{\partial x_j}} \\ \overline{\rho e'' u''_j},\ \overline{p'\frac{\partial u'_j}{\partial x_j}},\ \overline{\tau'_{ij} s'_{ij}}\ . \end{gathered} \tag{3.10}$$

The turbulent dissipation rate is defined as:

$$\epsilon = \frac{\overline{\tau'_{ij} s'_{ij}}}{\overline{\rho}}\ . \tag{3.11}$$

The most famous term is the Reynolds stress tensor $\overline{\rho u_i'' u_j''}$. Various turbulence models were developed in order to approximate it. In wide use are models containing the Boussinesq hypothesis:

$$-\,\overline{\rho u_i'' u_j''} = \mu_t \left(\frac{\partial\, \widetilde{u_i}}{\partial x_j} + \frac{\partial\, \widetilde{u_j}}{\partial x_i} - \frac{2}{3} \frac{\partial\, \widetilde{u_k}}{\partial x_k} \delta_{ij} \right) - \frac{2}{3} \overline{\rho} K \delta_{ij} \;, \tag{3.12}$$

where

$$K = \frac{1}{2} \widetilde{u_i'' u_i''} \tag{3.13}$$

is the turbulent kinetic energy and μ_t is the turbulent or eddy viscosity. K and μ_t need to be approximated e.g. by two transport equations for K and ϵ. A different approach is to calculate each entry of the Reynolds stresses tensor by means of an own transport equation, see section 3.1.2. This approach is referred to as Reynolds stress model (RSM) or Reynolds stress transport (RST) model. At this point we leave the topic of turbulence modelling, since it is not the focus of this thesis. The introduction to turbulence modelling was given in order to get an insight for what the obtained statistical results can be used. The analysis within this work will be focused on the Reynolds stresses as well as on the turbulent heat flux $\overline{\rho e'' u_j''}$.

3.1.2 Reynolds stress transport

The transport equation for $\overline{\rho u_i'' u_j''}$ can be derived in several steps. Differentiating equation (3.7c) ($\alpha = u_i, \beta = u_j$) as well as applying the chain rule (see equation (A.7)) leads to:

$$\begin{aligned} \frac{\partial}{\partial t}\left(\overline{\rho u_i'' u_j''}\right) = {} & \overline{u_j \frac{\partial}{\partial t}\left(\rho u_i\right)} + \overline{u_i \frac{\partial}{\partial t}\left(\rho u_j\right)} - \overline{u_i u_j \frac{\partial}{\partial t}\left(\rho\right)} \\ & + \widetilde{u_j} \frac{\partial}{\partial t}\left(\overline{\rho}\, \widetilde{u_i}\right) + \widetilde{u_i} \frac{\partial}{\partial t}\left(\overline{\rho}\, \widetilde{u_j}\right) - \widetilde{u_i}\, \widetilde{u_j} \frac{\partial}{\partial t}\left(\overline{\rho}\right) \;. \end{aligned} \tag{3.14}$$

Now, the non-averaged (2.1a, 2.1b) as well as averaged (3.8a, 3.8b) governing equations can be inserted. After splitting all averaged products and rearranging, the transport equation for the Reynolds stress tensor reads:

$$
\begin{aligned}
\frac{\partial}{\partial t}\left(\overline{\rho u_i'' u_j''}\right) \underbrace{+\frac{\partial}{\partial x_k}\left(\widetilde{u_k}\,\overline{\rho u_i'' u_j''}\right)}_{-C_{ij}} = & \underbrace{-\,\overline{\rho u_i'' u_k''}\frac{\partial\,\widetilde{u}_j}{\partial x_k} - \overline{\rho u_j'' u_k''}\frac{\partial\,\widetilde{u}_i}{\partial x_k}}_{PR_{ij}} \\
& \underbrace{+\frac{\partial}{\partial x_k}\left[\overline{\rho u_i'' u_j'' u_k''} + \overline{p'\left(u_i'\delta_{jk} + u_j'\delta_{ik}\right)}\right]}_{TD_{ij}} \\
& \underbrace{+\frac{\partial}{\partial x_k}\left(\overline{u_i'\tau_{jk}'} + \overline{u_j'\tau_{ik}'}\right)}_{VD_{ij}} \underbrace{+\overline{p'\left(\frac{\partial u_i'}{\partial x_j} + \frac{\partial u_j'}{\partial x_i}\right)}}_{PS_{ij}} \\
& \underbrace{+\overline{u_i''}\left(\frac{\partial\,\overline{\tau_{jk}}}{\partial x_k} - \frac{\partial\,\overline{p}}{\partial x_j}\right) + \overline{u_j''}\left(\frac{\partial\,\overline{\tau_{ik}}}{\partial x_k} - \frac{\partial\,\overline{p}}{\partial x_i}\right)}_{M_{ij}} \\
& \underbrace{-\,\overline{\tau_{ik}'\frac{\partial u_j'}{\partial x_k}} - \overline{\tau_{jk}'\frac{\partial u_i'}{\partial x_k}}}_{DS_{ij}}\ . \qquad (3.15)
\end{aligned}
$$

The terms are named as follows:

C_{ij} .. convection
PR_{ij} .. production
TD_{ij} .. turbulent diffusion
VD_{ij} .. viscous diffusion
M_{ij} .. mass-flux variation
PS_{ij} .. pressure strain
DS_{ij} .. turbulent dissipation .

3.1.3 Turbulent heat flux transport

The transport equation for the turbulent heat flux can be derived analogously. The equation in Cartesian coordinates reads:

$$
\begin{aligned}
\frac{\partial}{\partial t}\left(\overline{\rho e'' u_i''}\right) + \underbrace{\frac{\partial}{\partial x_j}\left(\widetilde{u}_j\,\overline{\rho e'' u_i''}\right)}_{-C_i} = \underbrace{-\frac{\partial}{\partial x_j}\left(\overline{\rho e'' u_i'' u_j''}\right)}_{TD_i} \\
\underbrace{-\,\overline{\rho u_i'' u_j''}\,\frac{\partial\,\widetilde{e}}{\partial x_j} - \overline{\rho e'' u_j''}\,\frac{\partial\,\widetilde{u}_i}{\partial x_j} - \overline{p u_i''}\,\frac{\partial\,\widetilde{u}_j}{\partial x_j} + \overline{u_i'' \tau_{jk}}\,\frac{\partial\,\widetilde{u}_j}{\partial x_k}}_{PR_i} \\
\underbrace{-\,\overline{u_i''\frac{\partial q_j}{\partial x_j}} + \overline{e''\frac{\partial \tau_{ij}}{\partial x_j}} + \overline{u_i'' \tau_{jk}\frac{\partial u_j''}{\partial x_k}}}_{DS_i} \\
\underbrace{-\,\overline{e''\frac{\partial p}{\partial x_i}}}_{PG_i}\,\underbrace{-\,\overline{p u_i''\frac{\partial u_j''}{\partial x_j}}}_{FD_i}\ .
\end{aligned}
\tag{3.16}
$$

This equation can be derived in various forms. Here, the instantaneous pressure and stress tensor have not been split, but kept inside the correlations. This avoids the appearance of too many terms, as proposed by Friedrich (1999). However, he presented a slightly different form, which can be transformed into equation (3.16) by applying the chain rule with respect to the convection term C_i. Gerolymos & Vallet (2014) on the contrary split also p and τ_{ij}. Consequently, the aggregation of the terms is not unique as well. In equation (3.16), the aggregation was made so that it appears in a similar fashion to the terms in the Reynolds stress tensor:

C_i .. convection
TD_i .. turbulent diffusion
PR_i .. production

DS_i .. turbulent dissipation
PG_i .. term containing pressure gradient
FD_i .. term containing fluctuating dilatation .

3.1.4 Averaging of the impinging jet

In this thesis, ensemble averaging with typically $N \approx 10^5$ is used. The ensemble-averaged flow field is then additionally averaged in the circumferential direction θ, since the averaged impinging jet is rotationally symmetric. The coordinate system (θ, y, r) is used for the analysis. All equations that were derived within this section can be adapted. Vectorial quantities, e.g. the velocity are transformed as follows:

$$\begin{aligned} u_\theta &= -u\sin(\theta) + w\cos(\theta) \\ u_r &= u\cos(\theta) + w\sin(\theta) \ . \end{aligned} \tag{3.17}$$

Components in the y-direction are unaffected. In Moser & Moin (1984), Reynolds stress transport equations are given for cylindrical coordinates using only Reynolds averages. In this work, Reynolds and Favre averages are used simultaneously. The derived transport equations are given in appendix A.1.3. All terms involving a derivative in the circumferential direction are omitted, since they are zero due to the circumferential average:

$$\frac{\partial\,\widetilde{\alpha}}{\partial\theta} = 0 \ , \ \frac{\partial\,\overline{\alpha}}{\partial\theta} = 0 \ . \tag{3.18}$$

On the contrary, averaged components in the circumferential direction are not neglected, since they could be different from zero, depending on the mode, e.g.:

$$\widetilde{u_\theta} \ \text{gen.} \ \neq 0 \ . \tag{3.19}$$

The biggest simulations within this thesis are resolved with more than one billion grid points. Storing one time step with the necessary five variables (pressure, velocity (x,y,z) and entropy) requires 41 GB of storage. It is not possible nowadays to store thousands of time steps so as to do statistical analysis as post-processing. Therefore, mean values, variances and budget terms are computed on-the-fly. The average of variable α at time step n can be computed recursively from the average at the previous time step and the current value of α:

$$\overline{\alpha}^{(n)} = \frac{n-1}{n}\,\overline{\alpha}^{(n-1)} + \frac{1}{n}\alpha^{(n)} \; . \tag{3.20}$$

Averages of terms containing fluctuations, e.g. the Reynolds stresses can be computed analogously:

$$\overline{\rho u_i'' u_j''}^{(n)} = \frac{n-1}{n}\,\overline{\rho u_i'' u_j''}^{(n-1)} + \frac{1}{n}\rho^{(n)} \underbrace{\left(u_i^{(n)} - \widetilde{u_i}^{(n)}\right)}_{u_i''^{(n)}} \underbrace{\left(u_j^{(n)} - \widetilde{u_j}^{(n)}\right)}_{u_j''^{(n)}} \; . \tag{3.21}$$

The fluctuations occurring in equation (3.21) require the knowledge of averages (e.g. $\widetilde{u_i}$). All involved averages need to be converged to a certain point in order to allow reasonable values of the fluctuations. In order to ensure the correct calculation of all statistical terms, the procedure is divided into the following steps: At first (step zero), the simulation runs until the influence of the start is faded away and the flow reaches a settled or periodic state. In this thesis, the simulations with $Re = 3300$ are started from the initial condition:

$$U_0 = [p, u, v, w, s]_0^\top = [p_\infty, 0, 0, 0, s\left(p_\infty, T_w\right)]^\top \; . \tag{3.22}$$

The initial condition for simulations with $Re = 8000$ is an interpolated instantaneous flow field of the corresponding case with $Re = 3300$. Skipping the starting of the impinging jet reduces the computational cost. However, some time steps need to be computed so that the effect of the interpolation and the change in the Reynolds number are decayed. In the following, the numbers are given exemplary for simulation #3 (supersonic impinging jet on > 1 billion grid points). The first 35000 time steps after the interpolation are not considered for the computation of statistics. If we approximate the time necessary for a fluid particle to pass from the inlet to the outlet of the domain (perfusion time) with

$$t_p \approx \frac{h + \frac{L_x}{2}}{v_\infty} \,, \tag{3.23}$$

the 35000 time steps correspond to 1.35 perfusion times. After the initialisation is done, averages including only instantaneous variables (step one, simple averages, equation (3.20)) are computed. Therefore, 82500 time steps (3.2 perfusion times) are used. This is enough for the averages to decrease its residuum by two orders of magnitude. In order to reach three orders of magnitude approximatively a half million time steps (only for this step of the averaging procedure) would be necessary. This would exceed the computational resources that can be provided. In the second step, averages of terms containing fluctuations (equation (3.21)) are computed. Also here, approximately 3 perfusion times ($2.9\, t_p$ corresponding to 75000 time steps) are required in order to decrease two orders of magnitude in the residuum. Since the cost of the averaging is relatively low, the previous simple averages can be continued. The circumferential averaging and updating was carried out directly after each restart of the simulation (each 24 hours of wall time). In the last step, terms that are simply products of averages are computed, for instance the convection C_{ij}. Figure 3.1 exemplary shows the convergence of the main variables p, u, v, w, s (first row) and the Reynolds stress transport terms TD_{ij}, VD_{ij}, PS_{ij}, DS_{ij} of simulation #3. Additional plots are given in appendix A.1.4: figures A.1 and A.2.

Computing averages on-the-fly reduces the required storage to a fraction. Nevertheless, this approach has one big disadvantage: all variables needed for the analysis have to be correctly implemented before the simulation is

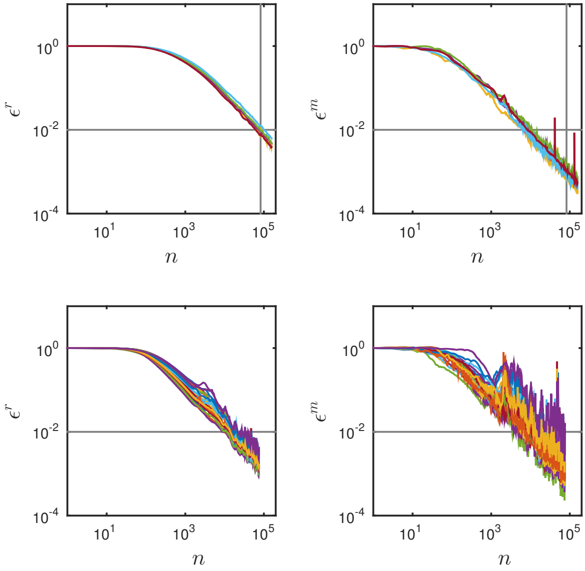

Figure 3.1: Convergence of the averaging for simulation #3. ϵ^r (first column) and ϵ^m (second column) are the RMS and the maximum value of the residuum within the domain, normalised with the respective value of the first time step of the averaging. First row: simple averages (p, u, v, w, s), second row: averages of terms including fluctuations (Reynolds stress transport terms TD_{ij}, VD_{ij}, PS_{ij}, DS_{ij}). The vertical gray line indicates the start of averaging step two.

carried out. Once it has run, all other statistical information is lost. The correctness of the budget equations can be checked since

$$C_{ij} + PR_{ij} + TD_{ij} + VD_{ij} + M_{ij} + PS_{ij} + DS_{ij} = 0 \;, \tag{3.24}$$

respectively

$$C_i + TD_i + PR_i + DS_i + PG_i + FD_i = 0 \tag{3.25}$$

holds due to the fact that the time derivative of an average value is zero for a statistically periodical flow such as the impinging jet.

For the Reynolds stress transport, equation (3.24) could be confirmed. Unfortunately, the same was not possible for the turbulent heat flux transport, equation (3.25). The imbalance term is denoted IB and arises mainly in the deflection zone of the impinging jet. For this reason, the budget terms of the turbulent heat flux are not presented within this thesis. However, equation (3.16) is in agreement with Friedrich (1999). The corresponding equations in cylindrical coordinates (appendix A.1.3.2) were checked several times. To the knowledge of the author, no publication exists where these equations are given and could be used for validation. Since the transformation from Cartesian to cylindrical coordinates was successfully done and due to the truth of equation (3.24), it is expected that the equations of the turbulent heat flux transport in cylindrical coordinates (3.16) are correct and that the error lies within the implementation of the equations within the code.

Additional to the on-the-fly data acquisition, sets of slices and three-dimensional fields of lower resolution (256^3 points) are stored, since they require much less storage. These sets are used in order to perform dynamic mode decompositions and scatter plots of correlations between variables.

3.2 Dynamic mode decomposition

In order to investigate the modes of the impinging jet, a dynamic mode decomposition (DMD) is used. The DMD allows the extraction of dynamically relevant flow features from time-resolved data. The coherent structures can be related to physical effects such as the impinging tone as well as the secondary maximum within the Nusselt number distribution. In the following, a brief summary of this method, developed by Schmid & Sesterhenn (2008) is given, based on Schmid (2010) and Schmid (2011).

The matrix

$$V_1^N = \{v_1, v_2, v_3, \ldots, v_N\} \tag{3.26}$$

contains N temporally equidistant instantaneous flow fields v_i. Each is reshaped and put into one column. The sub- and superscript of V state the first and last snapshot used for the matrix. For instance, V_1^N contains all fields (1 to N). The sequence of flow fields can be either generated experimentally or numerically. For the analysis of DNS data the set can consist of e.g. each 500th time step.

It is assumed that a linear mapping A connects subsequent flow fields within the entire sampling interval:

$$v_{i+1} = Av_i \ . \tag{3.27}$$

The flow field can then be expressed as a Krylov sequence:

$$V_1^N = \left\{v_1, Av_1, A^2v_1, \ldots, A^{N-1}v_1\right\} \ . \tag{3.28}$$

The goal is to extract dynamic characteristics such as eigenvalues and eigenvectors of the process described by A. Furthermore, it is assumed that beyond a critical number of snapshots, the vectors given by equation (3.27) become linearly dependent. Thus, v_N can be expressed as a linear combination of the previous and linearly independent vectors $\{v_1, v_2, \ldots, v_{N-1}\}$:

$$\begin{aligned} v_N &= a_1v_1 + a_2v_2 + \ldots + a_{N-1}v_{N-1} + r \\ &= V_1^{N-1}a + r \ , \end{aligned} \tag{3.29}$$

where a is a vector of unknown coefficients and r is the residual vector. According to equation (3.27), the reduced data sequence V_2^N can be expressed as:

$$V_2^N = AV_1^{N-1} \ . \tag{3.30}$$

Replacing its last entry with a linear combination of the previous ones (equation (3.29)), one can express this sequence as:

$$V_2^N = \{v_2, v_3, \ldots, v_N\} = \left\{v_2, v_3, \ldots, V_1^{N-1}a\right\} + re_{N-1}^\top \,, \tag{3.31}$$

where e_{N-1} is the $(N-1)^{\mathrm{th}}$ unit vector. Rewriting equation (3.31) in matrix form and considering equation (3.30) leads to:

$$V_2^N = AV_1^{N-1} = V_1^{N-1}S + re_{N-1}^\top \,. \tag{3.32}$$

The companion matrix S

$$S = \begin{bmatrix} 0 & & & & a_1 \\ 1 & 0 & & & a_2 \\ & \ddots & \ddots & & \vdots \\ & & 1 & 0 & a_{N-2} \\ & & & 1 & a_{N-1} \end{bmatrix} \tag{3.33}$$

has the size $(N-1) \times (N-1)$. The last column contains the unknown coefficients $\{a_1, a_2, \ldots, a_{N-1}\}$, which generate the linear representations of the last sample v_N in terms of the previous samples $\{v_1, v_2, \ldots, v_{N-1}\}$. The eigenvalues of S approximate some of the eigenvalues of A, see Schmid (2011) for details. In order to compute the unknown coefficients within the last column of S, the residual vector r (equation (3.29)) needs to be minimised. The last sequence v_N of a data set is expressed as a linear combination of the previous elements of the sequence. Consequently, the solution of the minimisation

$$\min_S \left\|V_2^N - V_1^{N-1}S\right\| \tag{3.34}$$

minimises the residual vector r. This can be realised with a QR-Decomposition:

$$S = R^{-1}Q^H V_2^N \,, \tag{3.35}$$

where Q^H is the complex conjugate transpose (adjoint) of Q and

$$V_1^{N-1} = QR \; . \tag{3.36}$$

The complex eigenvalues of the S describe the dynamics of the flow captured by the sequence. The eigenvalues λ_i^* and its corresponding eigenvectors x_i are obtained by solving the eigenvalue problem:

$$Sx_i = \lambda_i^* x_i \; . \tag{3.37}$$

The eigenvalues are then logarithmically mapped onto the complex plane:

$$\lambda_i = \frac{\ln(\lambda_i^*)}{\Delta t} \; . \tag{3.38}$$

The real part of λ_i represents exponential growth $\Re\left(\lambda_i\right) > 0$ respectively decay $\Re\left(\lambda_i\right) < 0$ and the imaginary part contains the temporal frequency:

$$f_i = \frac{\Im\left(\lambda_i\right)}{2\pi} \; . \tag{3.39}$$

The dynamic modes DM_i are the projection of the eigenvectors of S onto the reduced snapshot matrix:

$$DM_i = V_1^{N-1} x_i \; . \tag{3.40}$$

The flow field can be approximatively reconstructed using the dominant dynamic modes DM_j:

$$v\left(t\right) \approx \sum_{(j)} DM_j c_j e^{\lambda_j t} \; . \tag{3.41}$$

The coefficient vector $c = \{c_1, c_2, \dots, c_{N-1}\}$ is given by:

$$c = DM^{-1} V_1^N \; . \tag{3.42}$$

4 Description of the flow

4.1 Resolution

4.1.1 Kolmogorov microscales

Before we start to analyse the flow field of the impinging jet, it has to be ensured that the chosen resolution is sufficient. The Kolmogorov microscales give an estimation of the smallest scales that appear within a turbulent flow. These are computed with the kinematic viscosity ν and dissipation rate ϵ:

$$l_\eta \sim \left(\frac{\nu^3}{\epsilon}\right)^{1/4} \ , \ \tau_\eta \sim \left(\frac{\nu}{\epsilon}\right)^{1/2} \ , \ u_\eta \sim (\nu\epsilon)^{1/4} \ . \tag{4.1}$$

The length- l_η, time- τ_η and velocity scales u_η are valid for isotropic turbulence that occurs at "sufficiently high" Reynolds numbers. However, it is unclear what sufficiently high means in terms of a number (Pope (2000)). The Kolmogorov microscales can indicate only the order of magnitude of the scales that need to be resolved by the numerical grid. In Moser & Moin (1984), the resolution of DNS for different cases such as channel flow, boundary layer and isotropic turbulence are given. The statistical results agree well with experimental data even though the grid spacing is considerably (e.g. five times) larger than l_η. Pirozzoli et al. (2008) showed that structures within a supersonic boundary layer typically have a core radius of $5 - 6l_\eta$.

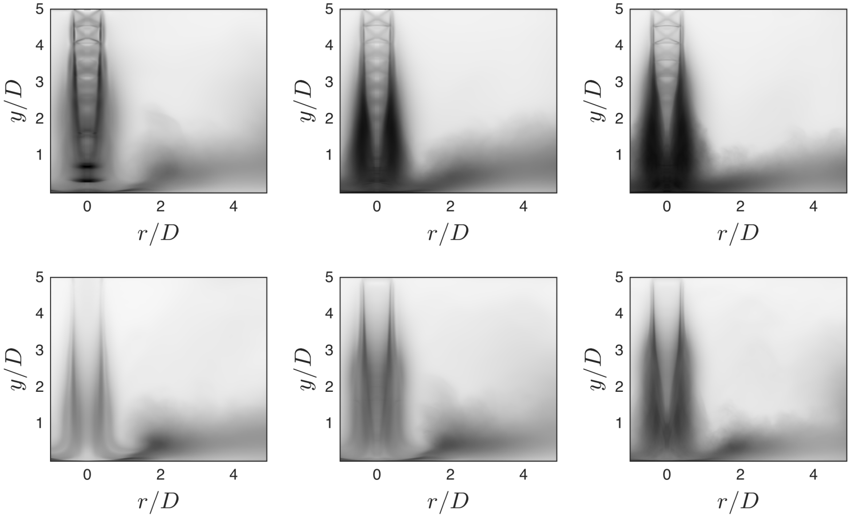

Figure 4.1: Ratio of mesh width to Kolmogorov length scale r_η in the range from 0 (white) to 2 (black). First row →: simulation #1, #2, #3. Second row →: simulation #4, #5, #6.

Figure 4.1 shows the ratio of mesh width to the Kolmogorov length scale

$$r_\eta = \frac{(\Delta x \Delta y \Delta z)^{1/3}}{l_\eta} \tag{4.2}$$

for the simulations carried out within this thesis. The highest values appear at the stagnation point ($r_\eta \leq 4.0$ for the supersonic- and $r_\eta \leq 2.1$ for the subsonic cases). Additionally, two areas exhibit relatively high values: the shear layer of the free jet ($r_\eta \leq 1.9$ for $Ma > 1$ and $r_\eta \leq 1.5$ for $Ma < 1$) and the wall jet around $r/D = 2$ ($r_\eta \leq 1.4$). A similar resolution with respect to the Kolmogorov scale was used by Dairay et al. (2015) for an incompressible impinging jet.

4.1.2 Energy spectra

A more precise statement whether the resolution is sufficient or not can be obtained when considering the energy spectra. If the energy-dissipating scales are not resolved, energy piles up within the smallest scales of the numerical grid. According to Moser & Moin (1984), the smallest length scales that must be accurately resolved are typically greater than the Kolmogorov length scale. E.g. most of the dissipation in a curved channel flow occurs at scales grater then $15 l_\eta$, based on average dissipation.

One-dimensional energy spectra are computed using 375 snapshots of a plane through the jet axis. Due to the rotational symmetry of the impinging jet, this plane is sufficient to detect a possible under-resolution. The original data on the stretched grid is interpolated on an equidistant one with a grid spacing that is equal to the smallest spacing of the original grid. A fast Fourier transform (FFT) is carried out for each line. The FFT are then averaged for each spatial direction separately.

Figure 4.2 shows the energy spectra plotted versus the dimensionless wavenumber in the x- ($k_x h$) respectively y-direction ($k_y h$). No accumulation of energy within the high wavenumbers exists. This confirms the appropriate resolution of the simulations. The slope $-5/3$ of the inertial subrange is shown as well. For those low Reynolds numbers of 3300 and 8000 only a tangent exists. Noticeable is the spectrum of the wall-normal velocity v in the wall-normal direction y. Here, the typical hump for low Reynolds numbers is missing. This is a consequence of the imposed laminar inlet velocity profile. With this profile, large coherent structures can develop without interruption, which was done on purpose in order to identify the modes of the impinging jet. The entire energy is introduced at low wavenumbers. Vortices in the scale of approximately $2 \cdot 10^{-2} - 2 \cdot 10^{-1}$ are missing, which are responsible for the characteristic hump.

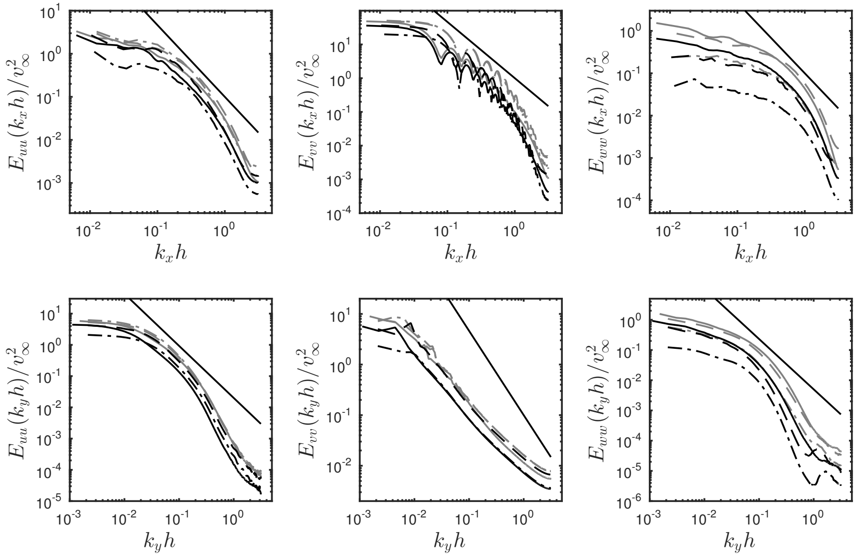

Figure 4.2: One-dimensional energy spectra E plotted versus the dimensionless wavenumber kh in the x- (first row) respectively y-direction (second row). Simulations: – · – ·: #1, — —: #2, ——: #3, – · – ·: #4, — —: #5, ——: #6, straight line: slope $-5/3$.

4.1.3 Boundary layer

The Kolmogorov microscales and the energy spectra consider the entire domain. A closer look has to be taken at the resolution of the boundary layer, especially attached to the impinging plate. Steep velocity and temperature gradients appear at the wall and must be resolved by the numerical grid. Following Eggels et al. (1994), an appropriate resolution is achieved when the first grid point near the wall is located at a dimensionless wall distance

$$y^+ = \frac{u_\tau y}{\nu} \tag{4.3}$$

of $y^+ \approx 1$ and three grid points are within the viscous sublayer. u_τ and

Figure 4.3: Dimensionless wall distance y^+ of the nearest grid point to the impinging plate. Simulations: – - –: #1, — —: #2, ——: #3, – - –: #4, — —: #5, ——: #6.

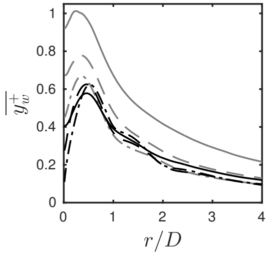

τ_w are the friction velocity and the wall shear stress:

$$u_\tau = \sqrt{\frac{\tau_w}{\rho}}\ ,\ \tau_w = \eta \left.\sqrt{\left(\frac{\partial u}{\partial y}\right)^2 + \left(\frac{\partial w}{\partial y}\right)^2}\,\right|_w \ . \tag{4.4}$$

The viscous sublayer extends from the wall to $y^+ \approx 5$ and is characterised by a laminar flow dominated by viscous forces. Figure 4.3 shows the distribution of y^+ of the nearest grid point to the impinging plate. The y^+-value is smaller than 0.67 for the entire impinging plate for all simulations that are analysed in terms of heat transfer (#1, #4 − #6). The other two supersonic simulations were carried out to investigate impinging tones. The resolution of the boundary layer was slightly coarsened in order to increase the time steps and save computing time, since no heat transfer is analysed ($\Delta T = 0$). The highest y^+-value at the wall occurs for simulation #3 with $y^+ = 1.01$. Consequently, simulations #1, #2, #4 and #5 have six points (not including the wall) within the viscous sublayer, #3 and #6 have four respectively seven. Thus, an appropriate resolution of the boundary layer is achieved.

4.2 Vortex dynamics

4.2.1 Primary and secondary vortex rings

The vortical structure within the impinging jet is crucial for both, heat transfer as well as noise generation. The development of vortices described in the following applies in general to both Reynolds numbers (3300 and 8000) for sub- and supersonic flow. Some specifics occur for supersonic impinging jets due to the presence of the standoff shock. Those are explained in section 4.4.

Figure 4.4 shows a set of snapshots taken from the subsonic simulations #5 (top left and second row) and #6 (top right). All images contain a plane through the jet axis, which is coloured with the temperature (black: cold, white: hot). Additional contours of Q are indicated. Q is the second invariant of the velocity gradient tensor A_{ij}:

$$Q = \frac{1}{4}\left(P^2 + \Omega_{ij}\Omega_{ij} - s_{ij}s_{ij}\right) \ , \tag{4.5}$$

where s_{ij}, Ω_{ij} and P are the rate-of-strain tensor (equation (2.3)), the rate-of-rotation tensor and the first invariant of the velocity gradient tensor A_{ij}:

$$\begin{aligned} A_{ij} &= \frac{\partial u_i}{\partial x_j} = s_{ij}\Omega_{ij} \\ \Omega_{ij} &= \frac{1}{2}\left(\frac{\partial u_i}{\partial x_j} - \frac{\partial u_j}{\partial x_i}\right) \ , \ P = -s_{jj} \ . \end{aligned} \tag{4.6}$$

For further explanations, see e.g. da Silva & Pereira (2008). Returning to figure 4.4, additional to the plane through the jet axis, the impinging plate is shown and coloured with the Nusselt number (black: high heat transfer, white: no heat transfer). We first concentrate on the top left image: Primary vortices (P) are created within the free jet shear layer as a consequence of the Kelvin-Helmholtz instability. Those vortices are transported downstream with the jet until they are deflected by the high pressure within the region around the stagnation point. The vortices impinge directly next to this region onto the impinging plate. Due to wall friction, a counter-rotating secondary vortex (S) develops. The presence of this one locally enhances heat transfer at the impinging plate indicated by the arrow. The annular shape of the affected area implies that also the primary and secondary vortices are vortex rings. This is proven in section 4.3.1. In the second row of figure 4.4, the temporal evolution (left to right) of the situation is shown. The first picture of this sequence is a crop of the top left. Travelling downstream the primary vortex ring, which was initially behind the secondary, approaches the secondary vortex ring and moves on top of it. This effect is caused by their mutual interacting velocity fields and leads to a change of the direction of motion of the pair from wall-parallel to wall-normal. As a consequence of this separation, the annular area of high heat transfer vanishes and the cycle restarts.

The same mechanism also appears at higher Reynolds number (8000). Contrary to the case of $Re = 3300$, the vortex rings do not develop perfectly periodically. The top right image of figure 4.4 shows two different snapshots of the simulation with $Re = 8000$. In the large image, the previous primary vortex ring was not generated "correctly" and therefore no local enhancement of heat transfer can be observed. A different situation is shown in the framed image detail, belonging to a different snapshot. Here, the above described effect occurs identical to the case with $Re = 3300$.

4.2.2 Leapfrogging and vortex split-off

During the movement of the primary vortices in the streamwise direction, two different phenomenons are observed: leapfrogging and vortex split-offs. Both involve small-scale vortices and therefore appear especially at the higher Reynolds number for sub- and supersonic cases.

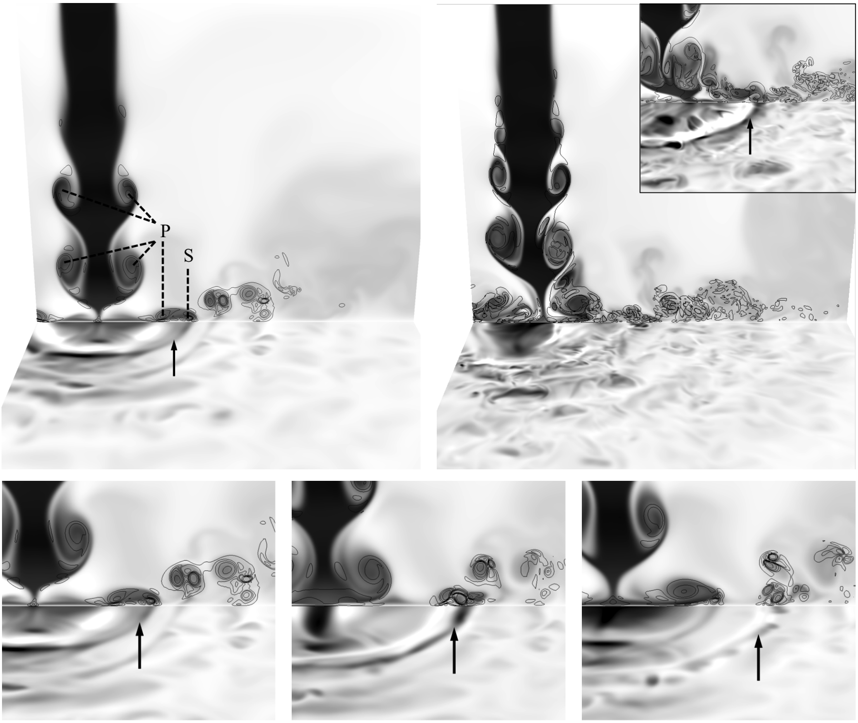

Figure 4.4: Instantaneous flow fields containing a cut through the jet axis (T, black: cold, white: hot and Q contours) and the impinging plate (Nu, black: high heat transfer, white: no heat transfer). Top left: simulation #5 ($Re = 3300$, $Ma = 0.78$), right: #6 ($Re = 8000$, $Ma = 0.78$) at two different time steps. P: primary vortex ring, S: secondary vortex ring. Second row: three consecutive snapshots of #5.

The leapfrogging mechanism is shown in figure 4.5. Three consecutive snapshots (left to right) of Q (normalised) within the jet shear layer are snapped. Two similar vortex rings (1a,1b) and (2a,2b) are travelling downstream one after another (left). Due to their mutual interaction (middle) the frontal vortex decelerates and increases its diameter whereas the rear one accelerates and shrinks in diameter (Riley (1998)). Thereafter

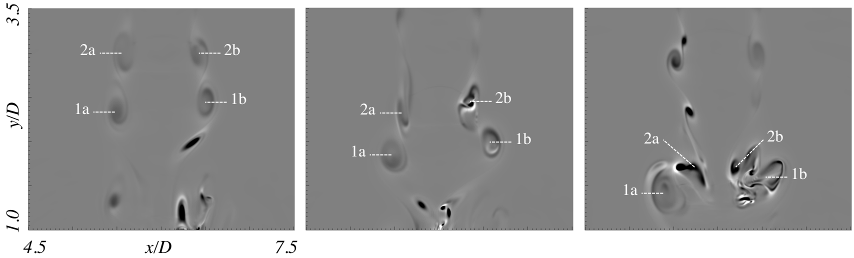

Figure 4.5: Leapfrogging in the shear layer of the free jet region (#6), consecutive snapshots →. Shown is QD/v_∞^2 in the range −85 (white) to 85 (black).

(right), the rear vortex ring (2a,2b) passes through the front ring (1a,1b). Depending on the positions of the vortices , the process can either be complete before the vortices interact with either the impinging plate or the shock (in the supersonic case) or even during the interaction.

In figure 4.4 of the previous section, it can be seen that the primary and secondary vortex rings are very axisymmetrical in the case of the low Reynolds number. With increasing Reynolds number, small-scale vortices overlay and influence these structures. Although, the main flow structure remains axisymmetrical (see section 4.3), temporary asymmetries occur. These asymmetries are also triggered by the acoustic field, especially in the supersonic case. An example of such an asymmetry is the split-off of a vortex as shown in figure 4.6. While the vortex ring on the left side of the axis (1a) is unchanged, the ring splits on the right side into two parts (1b,1c). Thereby, the newly emerged one (1c) takes the position of the original structure (1b), which moves out of the jet and therefore slows down. These asymmetries explain why enhanced heat transfer due to secondary vortex rings decreases in time-average at the higher Reynolds number. Furthermore, the effect plays a role within the sound source mechanism of the impinging tone (section 5.1).

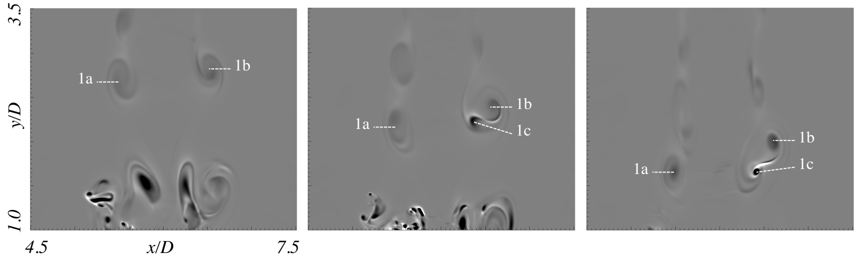

Figure 4.6: Vortex split-off in the shear layer of the free jet region (#6), consecutive snapshots →. Shown is QD/v_∞^2 in the range -85 (white) to 85 (black).

4.3 Modes

4.3.1 Subsonic impinging jets

Since we have seen that the vortices of the impinging jet are closely related to the heat transfer at the impinging plate, we want to study these structures. In order to do that, a dynamic mode decomposition, as explained in section 3.2, was carried out. We saw already that the flow at lower Reynolds number tends to be more regular and less asymmetric (figure 4.4). For this reason, simulation #5 ($Re = 3300, Ma = 0.78$) is analysed first.

The instantaneous flow fields v_i used to build the snapshot matrix V_1^N can contain either the entire domain or a subdomain. A two or three-dimensional field is reshaped to a vector. Furthermore, different flow variables can be included within this vector. It is advisable to scale different variables, so that they lie within the same order of magnitude. For all carried out DMD, the outer area ($r > 4$) was cut in order to save computing time and memory. First, a DMD including all grid points of a plane through the jet axis with the variables p, T, Q and $\frac{\partial T}{\partial dy}$ was carried out. As explained in section 3.2, it is assumed that the vectors become

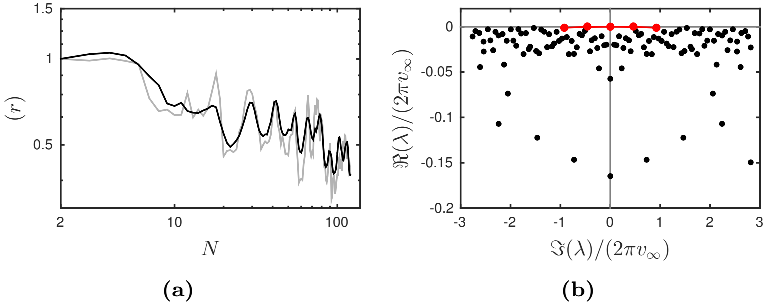

(a) **(b)**

Figure 4.7: Simulation #5 a) Convergence of the residual vector r. Black: r_{RMS}, gray: $r_{\max}$ normalised with the values of $N = 2$. b) Eigenvalue spectrum computed using a DMD. Red marked points correspond to dominant modes.

linearly dependent after a critical number of time steps, e.g. after one period of the main flow characteristics. In Schmid (2010), a cavity flow was shown exemplary where the norm of the residual vector r lost three orders of magnitude when the number of used snapshots N was increased from 2 to 17. The convergence of the present DMD of simulation #5 is shown in figure 4.7a. Despite the fact that the flow looks rather periodical, no similar decline of the residual can be observed. For this reason, 120 snapshots are used which are at an interval of 510 time steps each. The analysed time frame is large enough to reach reasonable convergence with respect to the mean values, as shown in figure 3.1. The highest frequency that can be resolved with this step width is $Sr = 2.81$ assuming two points per period.

Figure 4.7b shows the eigenvalue spectrum of the flow. The eigenvalues are normalised so that one can realise the Strouhal numbers directly from the abscissa. The ordinate indicates growth respectively decay. The modes and eigenvalues usually appear as complex conjugate pairs. Within this thesis, the terms mode and eigenvalue refer to the corresponding pairs. The mode at (0,0) represents the mean flow field since it has no frequency and is not damped. In order to define the dominant modes, each mode of the

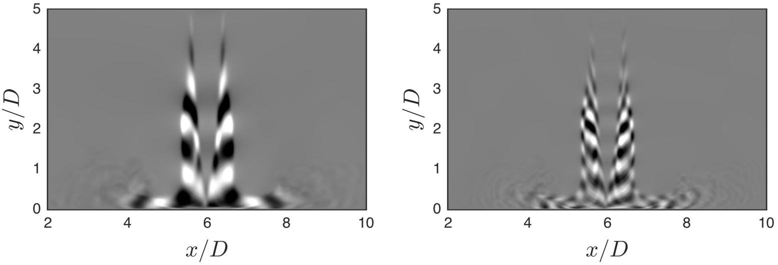

Figure 4.8: Temperature field of the dominant dynamic modes (#5) left: $Sr = 0.46$ (±30 K), right: $Sr = 0.92$ (±20 K).

remaining is multiplied with the corresponding coefficient and $DM_j c_j e^{\lambda_j t^*}$ is compared to the fluctuating flow field $v'(t^*)$ at $t^* = t(n = N/2)$. The 2-norm of the difference is the basis for the sorting of the modes. The dominant modes have the Strouhal numbers ±0.46 and ±0.92 and a low damping.

Figure 4.8 and 4.9 show the temperature field and Q of the two dominant modes. The left images correspond to $Sr = 0.46$ and the right ones to $Sr = 0.92$. For all illustrations, the modes are multiplied with its coefficients to allow a physical interpretation. The structures are symmetrical and are located within the shear layer of the free jet as well as within the wall jet until $r/D \approx 2$. These are the zones where the primary and secondary vortices pass. The reconstruction of the flow field using those two modes as well as the mean flow field is shown in figure 4.10 (right) and compared with the original field (left). A remarkable conformity between both fields can be seen. The DMD proves that vortices develop periodically in the shear layer and are a superposition of a larger and a smaller structure. The larger structure corresponds to the frequency $Sr = 0.46$ and the smaller one oscillates with the double frequency $Sr = 0.92$.

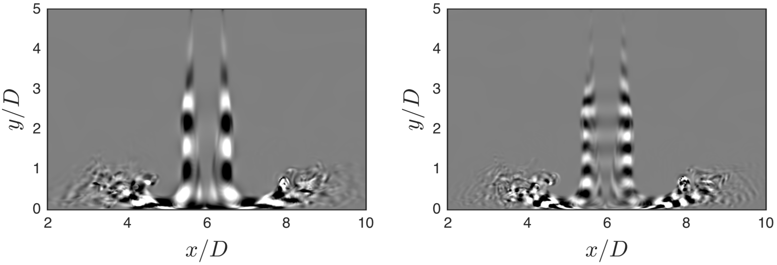

Figure 4.9: Q ($\pm 3.1 v_\infty^2 D$) of the dominant dynamic modes (#5) left: $Sr = 0.46$, right: $Sr = 0.92$.

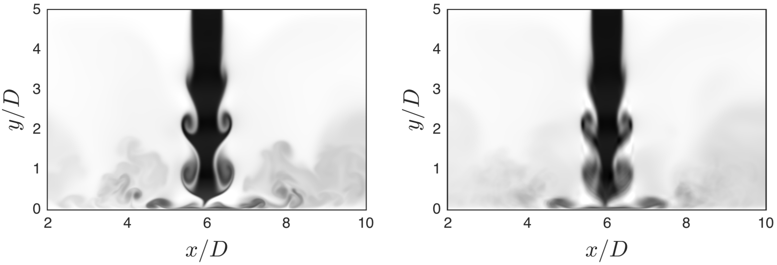

Figure 4.10: Confrontation of original flow field (left) and reconstruction using the mean field and the two dominant modes (right), #5.

Three-dimensional mode. The two dominant modes computed using a plane through the jet axis ($z/D = 6$) are strongly symmetrical. Therefore, the three-dimensional structure can be either axisymmetrical or flapping within the $x/D = 6$-plane. In order to clarify this issue, a three-dimensional DMD was carried out as well.

Since this requires huge amounts of main memory, each fourth grid point was used to build the snapshot matrix. A comparison of two resolutions used for the two-dimensional DMD is presented in appendix A.2.1.2, figures A.8 to A.11. Neither convergence, nor the dominant modes depend on the resolution.

Q-contour plots of the three-dimensional modes are shown in figure 4.11.

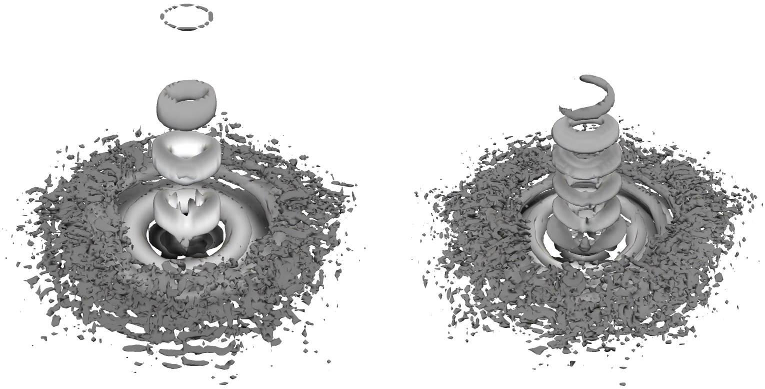

Figure 4.11: Q contours ($\pm 3.1 v_\infty^2 D$) of the tree-dimensional dominant dynamic modes (#5) left: $Sr = 0.46$, right: $Sr = 0.92$ coloured with the pressure ($\pm 0.08 p_\infty$).

Additional contour plots of the pressure can be found in the appendix, figure A.12. They prove that the dominant modes within the subsonic impinging jet (#5) are axisymmetrical. The primary and secondary vortices are toroidal.

Influence of the Mach number. The role of vortex rings with respect to local heat transfer enhancement as well as the modes were described for a simulation within the high subsonic regime ($Ma = 0.78$). For some applications the nozzle pressure ratio and therefore the Mach number are restricted so that the compressibility effects are much lower. For this reason the influence of the Mach number is controlled. The analysis of simulation #4 ($Ma = 0.41$) shows that the evolution of the vortex rings is almost unaffected by the Mach number. However two differences can be observed. The dimensionless frequency of the dominant modes of subsonic impinging jets shifts to higher values with decreasing Mach number. In concrete terms, the Strouhal number increases from 0.46 and

0.92 at $Ma = 0.78$ to 0.54 and 1.08 at $Ma = 0.41$. At higher Mach number, the amplitude of the modes and therefore the strength of the vortices is homogeneous comparing the free jet and the wall jet region. At the lower Mach number however, the strength of the vortices increases from the free- to the wall jet. The reduced intensity of the primary vortices within the free jet leads to a decrease of the constriction between consecutive primary vortex rings. Illustrations can be found in appendix A.2.1.1.

Influence of the Reynolds number. Increasing the Reynolds number means increasing the turbulence. This makes the identification of coherent structures more difficult, since the small vortices are not only superposed on the larger ones, they influence each other. Additional effects such as leapfrogging and vortex split-off occur (section 4.2.2) and decrease the regularity of the flow. For this reason, no convergence of the residual vector r exists, as it can be seen in figure 4.12a. Additionally, the real parts of the dominant modes become strongly negative, the modes are now damped. Nevertheless, the increase of the Reynolds number has no affect on the Strouhal numbers of the dominant modes. They remain at $Sr = 0.46$ and 0.92, but 200 instead of 120 snapshots were needed to find them.

The comparison of the temperature of the modes between #5 (figure 4.8) and #6 (figure 4.13) shows that the structure of the first dominant mode (left, $Sr = 0.46$) is nearly unchanged. The second mode however (right, $Sr = 0.46$), looses its symmetry within the free jet for $y/D \lesssim 1.5$. This is a difficulty in the detection of the mode due to the increased turbulence and does not mean a change of the mode itself, e.g. to helical or flapping. For Q see figure A.13.

The reconstruction of the flow field using the mentioned modes still indicates the vortex rings, even though the quality decreased. The three-dimensional DMD proves that the mode is toroidal. The corresponding structures are shown in appendix A.2.1.3, figures A.14 and A.15.

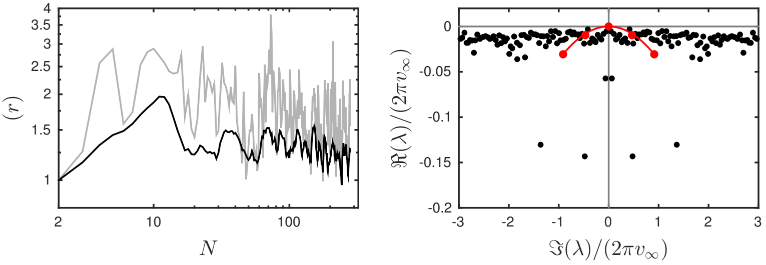

(a) **(b)**

Figure 4.12: Simulation #6 a) Convergence of the residual vector r. Black: r_{RMS}, gray: $r_{\max}$ normalised with the values of $N = 2$. b) Eigenvalue spectrum computed using a DMD. Red marked points correspond to dominant modes.

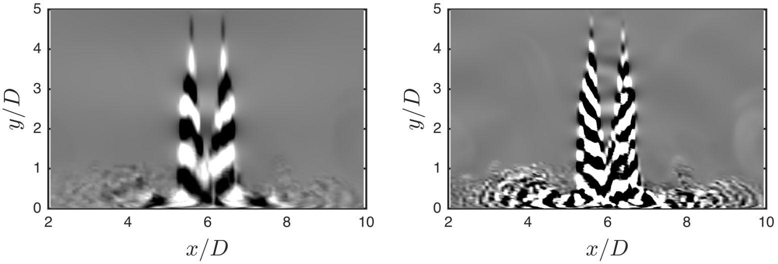

Figure 4.13: Temperature field of the dominant dynamic modes (#6) left: $Sr = 0.46$ (± 30 K), right: $Sr = 0.92$ (± 20 K).

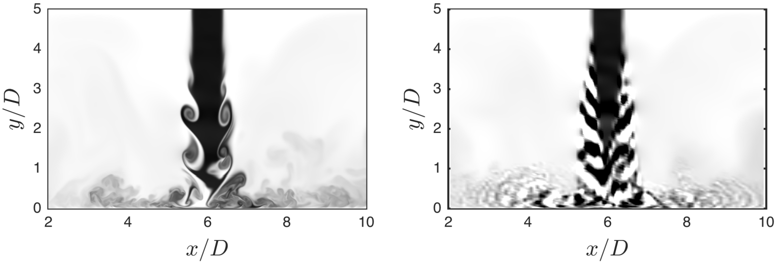

Figure 4.14: Confrontation of original flow field (left) and reconstruction using the mean field and the two dominant modes (right), #6.

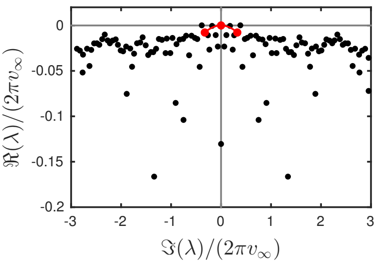

Figure 4.15: Eigenvalue spectrum of simulation #3 computed using a DMD. Red marked points correspond to dominant modes.

4.3.2 Supersonic impinging jets

In section 1.3, it was shown that free jet screech is strongly related to the modal structure of the jet. Such a linkage may exist but is presently not established for impinging jets, since the modes itself are mainly unknown. Furthermore, no consensus regarding the sound source mechanism was found. In order to clarify this issue for the low supersonic regime, a DMD based on simulation #3 ($Re = 8000, Ma = 1.11$) was carried out.

Figure 4.15 shows the eigenvalue spectrum. Similar to the subsonic case with $Re = 8000$, the dominant mode of the supersonic impinging ($Re = 8000$) is slightly damped, indicating a disturbed periodical flow. Its Strouhal number is 0.324. In contrary to the subsonic case, no mode with the double frequency (harmonic) is detected by the DMD.

The flow of a supersonic impinging jet is not only dominated by primary and secondary vortices. The DMD reveals a much more complex flow field that can be seen in figure 4.16. A full period of the cycle including five snapshots is shown. The sixth snapshot, which is not shown, would be again at the same phase point as the first one. For each point in time (each row) three images are depicted. In the left and middle column, the original flow field is shown (Q respectively p). The right column shows the pressure obtained from the reconstruction of the flow field using only the time mean and the dominant dynamic mode.

In the first point in the phase (first row) a highly turbulent area with plenty of small vortices close to the stagnation point ($y/D \lesssim 1$) exists.

These vortices are leftover from the former period and will be explained later. The flow in this area is mainly subsonic. Large vortical structures are present in the upper part of the domain ($y/D \gtrsim 2$) and belong to the new period that we investigate now. The first vortex ring in the streamwise direction ($y/D \approx 2$) is significantly stronger than the following ones. In this specific period a vortex split-off takes place (section 4.2.2), but this is not of relevance for the DMD-cycle. The particular strength of this first vortex ring becomes clear regarding the original pressure field (middle), and especially the reconstructed pressure field (right). Therefore, we will call it head vortex. Slightly in front is the sonic line. Advancing in time (second and third row), the subsequent vortices accelerate, as described in section 4.2.2. Consequently the supersonic area splits into two parts, as indicated by the sonic line. In the fourth row, the supersonic area approaches the deflection zone, encounters areas of high pressure (lumps) and forms standoff shocks. Now, shock-vortex- and shock-vortex-shock-interactions occur. These two phenomenons are described in detail in sections 5.1.1 and 5.1.2. They cause enormous pressure waves that lead to the destruction of the large structures (vortex rings), as it can be seen in the last row of figure 4.16. The breakdown of the large vortices continues in the beginning of the new period, as shown in the first row. The end of the cycle also includes the disappearance of the supersonic area.

In contrary to the subsonic impinging jet, the dominant mode does not correspond with each primary and secondary vortex ring. In fact, it describes a bunch of vortices including a head vortex and multiple subsequent vortices of lower strength that merge into an area of low pressure. The three-dimensional mode shown in figure 4.17 proves that the dominant mode with $Sr = 0.32$ is toroidal.

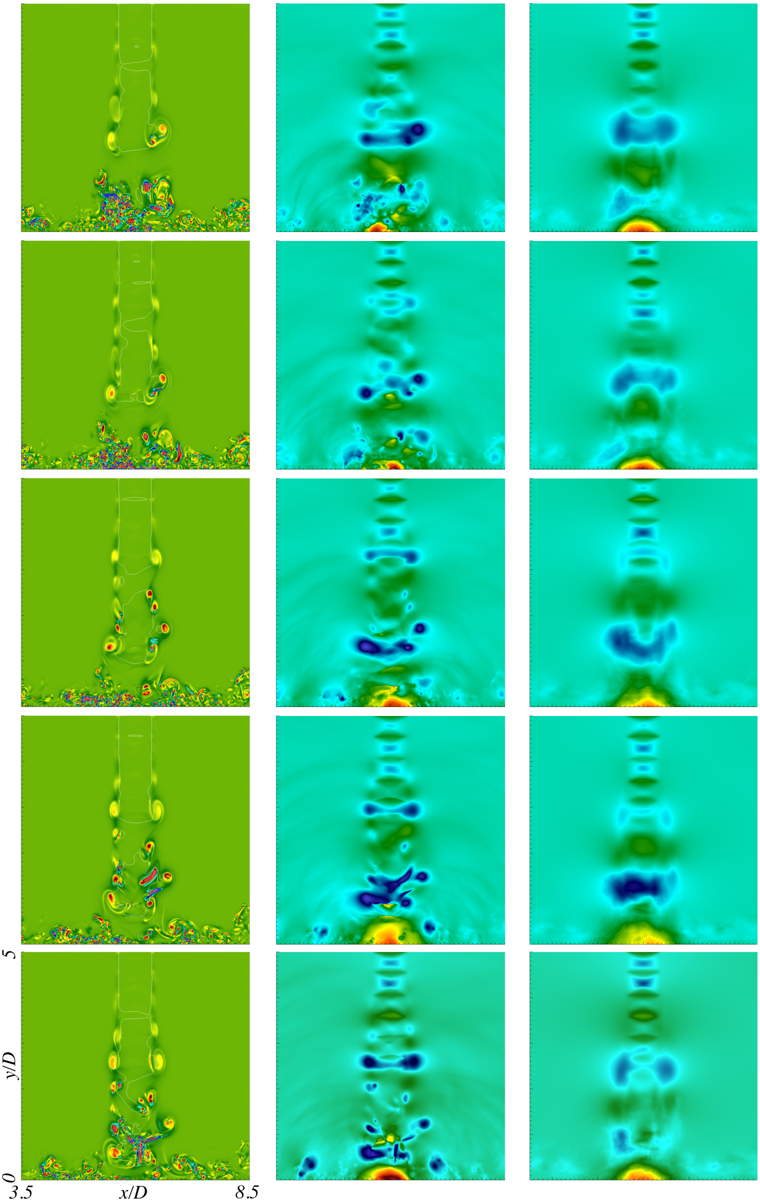
5
y/D
0
3.5
x/D
8.5

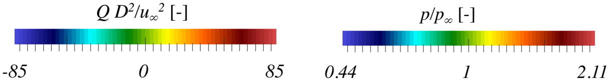

Figure 4.16: Periodical flow of a supersonic impinging (#3). First column: normalised values of Q of the original flow field. Second and third column: p of the original flow field and of the reconstruction using the mean field and the dominant dynamic mode with a Strouhal number of $Sr = 0.32$. The snapshots (rows) are in consecutive order.

Figure 4.17: Pressure contours ($\pm 0.02 p_\infty$) of the tree-dimensional dominant dynamic mode $Sr = 0.32$ (#3) coloured with the temperature ($\pm$30 K).

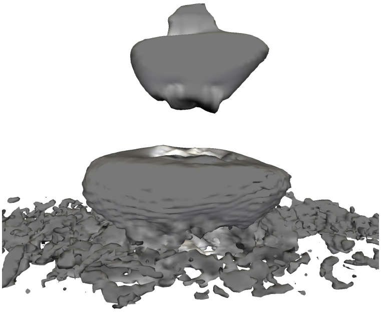

Influence of the Reynolds number. The above described mode of a supersonic impinging jet with a Reynolds number of 8000 (#3) occurs equally at $Re = 3300$ (#2). Only a minor difference can be observed: In the case of $Re = 8000$, the pressure waves emerging due to shock-vortex- and the shock-vortex-shock-interactions lead most commonly to the breakdown of the primary ring vortices. At the lower Reynolds number, these vortices can withstand the attack of the pressure waves. Consequently, the development of secondary vortex rings is much stronger distinct at $Re = 3300$. However, this detail is not relevant for the generation of impinging tones yet it affects heat transfer at the impinging plate. Due to the fact that these two simulations are carried out with $\Delta T = 0$, heat transfer is not investigated.

Influence of the ambient temperature. Simulations #2 and #3 have a total inlet temperature that is equal to the wall and ambient temperature: $T_{t,in} = T_w = T_\infty = 293.15$ K ($\Delta T = 0$ K). In simulation #1, the wall and ambient temperatures differ: $T_w = T_\infty = 373.15$ K, whereas the total inlet temperature was not changed ($\Delta T = 80$ K). The configuration of a cold jet surrounded by hot fluid is typical for cooling configurations. Simulation #1 has a Reynolds number of 3300 and therefore can be compared to #2.

The change of the ambient temperature leads to the introduction of a specific characteristic: the flow changes between two modes, which have the same dimensionless frequency: $Sr \approx 0.35$. Multiple modes for one set of parameters also occur in free jets, as described in section 1.3.2. The two different modes of simulation #1 are denoted A and B, but are different from the labels A and B of free jet screech.

In mode A axisymmetrical vortex rings develop with the characteristic frequency. Those vortex rings are so far from each other that they do not interact and no leapfrogging is observed. Each vortex ring behaves exactly as the head vortex described above (#3, $Re = 8000$). Due to the strongly symmetric flow, the deflection zone is not disturbed as strong as in simulation #3. This area is analysed in section 4.4. Consequently, no high pressure lumps appear. There is only one coherent area of high pressure in the vicinity of the stagnation point. Therefore only one standoff shock is created for each period for this mode. The shock appears at $y/D \approx 0.25$, moves counter-streamwise and interacts with the (only) vortex ring at $y/D \approx 0.75$.

Mode B on the contrary is equal to the mode observed in simulations #2 and #3. Here, the vortex rings develop more frequently and allow leapfrogging. Despite the different appearance of those two modes, the head vortex formates with the same frequency. An interesting aspect would be to investigate the switch between those two modes. Unfortunately this requires too much computing time. Within the time frame necessary in order to reach statistical convergence and obtain sound spectra, the

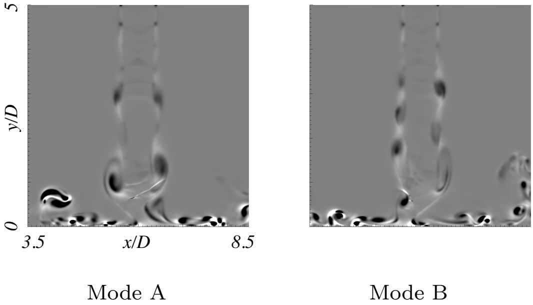

Mode A Mode B

Figure 4.18: Two different modes exist for a cold impinging jet at $Re = 3300$ ($T_0 = 293.15$ K) in a hot environment ($T_\infty = T_W = 373.15$ K) with the same frequency $Sr \approx 0.35$. Shown is QD/v_∞^2 in the range -8.5 (white) to 8.5 (black).

Figure 4.19: Dominant dynamic modes of the impinging jet as function of Ma_∞. Filled squares: dominant modes with $\Delta T = 80$ K, not filled squares: secondary modes with $\Delta T = 80$ K, triangle: dominant mode with $\Delta T = 0$ K.

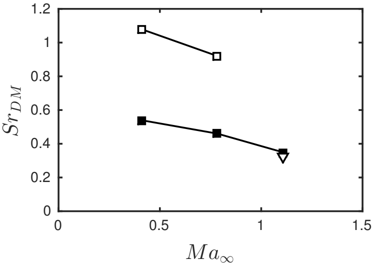

Mode switched from A to B and back to A. This is not enough to find an orderliness, even less a frequency of the switch.

A summary of the dynamic modes of all simulations carried out within this thesis is shown in figure 4.19.

4.3.3 Schlieren imaging

Schlieren imaging is a technique that visualises density gradients. The underlying physical effects are refraction and diffraction of light. Light rays encounter these mechanisms when they pass through materials with changing density, e.g. when they pass a compressible impinging jet. Due to turbulence the velocity and hence the density of the flow is inhomogeneous.

Figure 4.20 shows a sketch of a Toepler Z-type schlieren arrangement that was used for the present investigation. Two concave mirrors on both sides of the jet are used to create parallel rays out of the light emitted by a lamp. A screen with a slit is placed directly in front of the lamp in order to shield the rays that are not orientated in the desired direction. On the other side of the jet, the second mirror bundles the parallel rays and sends them to a camera. Closely in front of the camera is the focal point where a razor blade is installed. Light rays that encounter strong density gradients are refracted and cannot pass through the focal point, since they are stopped by the razor blade. Consequently, the corresponding area within the image is darker. The orientation of the razor blade determines the component of the density gradient that is imaged. The implementation of the set-up is shown in figure 4.21. As recording device, a Vision research Phantom v2512 was used. In this picture, the orifice and the impinging plate are not installed for lucidity. The entire set-up is shown in appendix A.2.1.4, figure A.16. As pressure reservoir a barrel placed in vertical position with the volume of 41.2 dm^3 is used. At the lower end, the supply for compressed air is installed. This means the reservoir is feed by a compressor. This layout ensures a constant pressure for the measurement. The pressure is controlled through a valve between the compressor and the barrel and monitored using a PGP PUM50.2.1.08G.A73.0 sensor. At the upper end of the reservoir, a conical nozzle reducing the diameter from G 1 1/2" to 10 mm within 60 mm is attached. The total length of the nozzle is 238mm.

The visualisation of an impinging jet corresponding to simulations #2

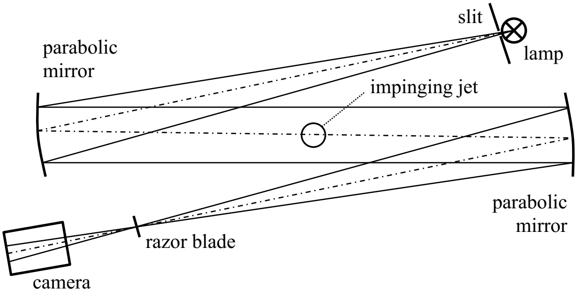

Figure 4.20: Sketch of a Toepler Z-type schlieren arrangement, see Settles (2001).

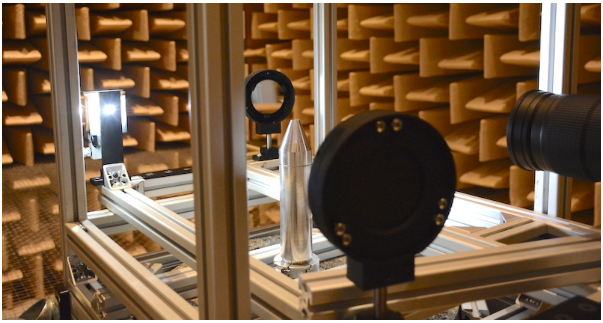

Figure 4.21: Experimental set-up for schlieren visualisation excluding the razor blade bracket.

and #3 was carried out at high Reynolds number: $Re \approx 485000$. The image is depicted in figure 4.22 and shows a helical mode. The simulations however contain a toroidal mode. The difference can either be caused by the huge discrepancy in Reynolds numbers or due to the fact that two different modes may exist for this set of parameters. The latter exists for free jets at similar fully developed Mach numbers of approximately 1.2. Here, we investigate an impinging jet at $Ma_\infty = 1.11$. The answer of this question presently remains open. Since DNS with $Re = 485000$ is not possible, an experiment with a jet at much lower pressure expanding into a low pressure “vacuum” chamber can reach clarification.

Figure 4.22: Schlieren image for a supersonic impinging jet with $NPR = 2.15$ and $h/D = 5$.

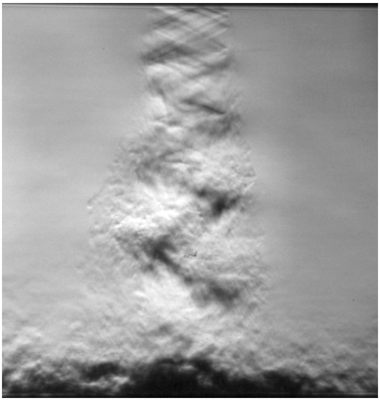

4.4 Deflection zone and standoff shock

The DMD of supersonic impinging jets with $h/D = 5$ (section 4.3.2) showed that the standoff shocks are not continuously present, see e.g. the first two rows of figure 4.16. At a later point in time, the shocks develop and can be clearly seen in the fourth row at $y/D \approx 0.6$ and 0.9.

The shock generation periodically occurs due to the approach of the supersonic area to locations of high pressure ($\gtrsim 1.3p_\infty$) within the deflection zone. Those locations can be either a single coherent zone in the vicinity of the stagnation point or a lump which was split-off from the coherent zone due to strong pressure waves. The nature of the high pressure areas differ between the carried out simulations and determine the movement and number of standoff shocks.

For instance, the supersonic simulation with a heated environment (#1, $\Delta T = 80$ K) features a mode (mode A) that is strictly periodical and axisymmetrical. The area of high pressure within the deflection zone is not disturbed as strongly as in the simulations with $\Delta T = 0$K (#2,3). This observation can be quantified by the pressure at the impinging plate, which is shown in figure 4.23. Comparing simulation #1 and #2, we see that the pressure recovery at the impinging plate $(\overline{p} - p_\infty) / (p_{t,in} - p_\infty)$

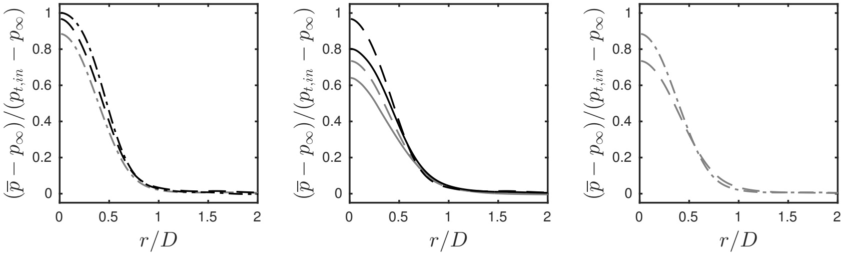

Figure 4.23: Pressure recovery at the impinging plate. Left: influence of the Mach number *Ma*: #4 (0.4), #5 (0.8), #1 (1.1); middle: influence of the Reynolds number *Re*: #2,5 (3300), #3,6 (8000); right: influence of a heated environment: #2 (not heated; $\Delta T = 0$ K), #1 (heated; $\Delta T = 80$ K). –·–·: #1, — —: #2, ——: #3, –·–·: #4, — —: #5, ——: #6.

reaches values of 0.89 respectively 0.74, showing a more stable deflection zone in #1. The pressure recovery decreases with increasing Mach and Reynolds number and increases when the environment is heated.

A simple gedankenexperiment can link the movement of the high pressure within the deflection zone to the pressure recovery at the impinging plate. We approximate the high pressure around the stagnation point as a half-unit circle with the flat side to the bottom and add a normally distributed random movement of the centre in the radial direction. In case of a very small movement the shape of the function is still approximately a half-unit circle and the maximum value is still close to one. This case represents simulation #1. If we increase the variance of the random displacement, representing #2, the shape changes and the maximum value decreases. As a result, the two curves have to cross each other at some point. The crossing can be observed between simulations #4 and #5 as well as (#2, #3) (#5, #6) and (#1, #2). No crossing between (#1, #4) respectively (#1, #5) implies that the lower pressure recovery of the supersonic impinging jet, compared to the subsonic ones, is mainly caused by losses due to increased turbulence as a result of interactions between vortices and shocks, as described in sections 4.3.2 and 5.1.

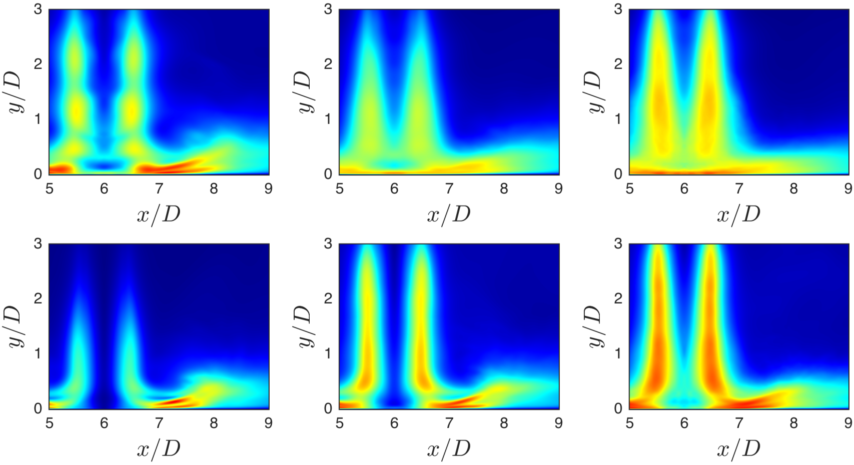

Figure 4.24: Scaled RMS-values of the radial velocity fluctuation $v'_{\mathrm{RMS}}/v_\infty$ from 0 (blue) to 0.3 (red). First row, →: simulation #1, #2, #3. Second row, →: simulation #4, #5, #6.

The RMS-values of the axial velocity fluctuation, which are shown in figure 4.24, confirm the given explanation. Simulation #4 with a pressure recovery of approximately one, has almost no radial velocity fluctuations in the vicinity of the stagnation point. The fluctuations increase with increasing Mach and Reynolds number and decrease when the environment is heated.

Using the adaptive shock-capturing filter (section 2.2.4), the position of the standoff shock can be detected. Figure 4.25 shows the RMS of the filtering strength σ^{sc} computed using 375 snapshots. In the two simulations with $\Delta T = 0$ (#2,3), shocks appear and move mainly in the range $0.25 \lesssim y/D \lesssim 1$, even though they can depart up to two diameters from the impinging plate. Due to the highly turbulent flow field, the stagnation point usually produces multiple high pressure lumps and therefore multiple standoff shocks that are often oblique. This can be realised regarding the filtering strength at around one diameter in front

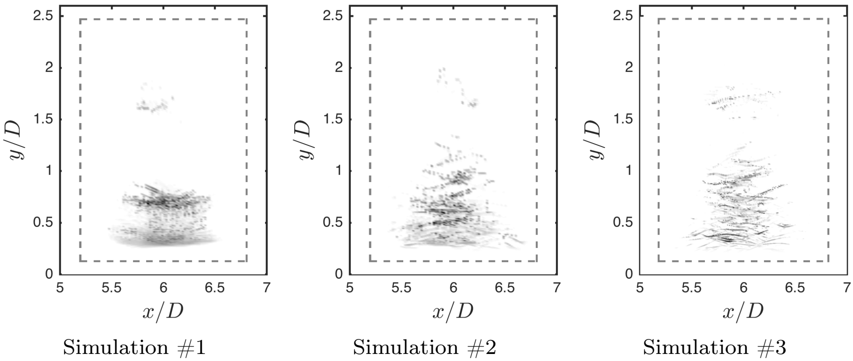

Simulation #1 Simulation #2 Simulation #3

Figure 4.25: Standoff shock position detected using the adaptive shock-capturing filter. Shown is the RMS of the filtering strength σ^{sc}. The gray dashed frame indicates the area of the domain where the filter is enabled.

of the lower wall. Here, the shocks occur less often and therefore oblique positions can be spotted. On the contrary, the strong periodicity of mode A of #1 leads to an oscillation of the shock in the range $0.25 \lesssim y/D \lesssim 0.75$. Although some oblique traces of the shock can be observed, the pattern is mainly parallel to the wall.

The movement of strong gradients related to the shock leads to strong fluctuations of pressure and axial velocity. The clearly defined shock position of mode A within simulation #1 reflects in the RMS-values of p' and u'_r. The corresponding illustrations can be found in appendix A.2.2: figures A.17 and A.18. Plots concerning simulation #6 of figures 4.24 and A.18 were already published in Haucke et al. (2015).

The observed standoff shock locations for $NPR = 2.15$ and $h/D = 5$ are profoundly different from the ones at higher nozzle pressure ratio and lower nozzle-to-plate distance, as investigated by Iwamoto (1990), figure 1.2. In the latter, the impinging plate is placed within the shock cell system leading to a defined position of the shock that varies only through small oscillations.

4.5 Wall jet

This section is taken from Wilke & Sesterhenn (2016c). Minor changes have been applied. According to radial velocity, we divide the wall jet into four zones. The accelerating zone ($0 \leq r/D \lesssim 0.8$), the zone of maximal radial velocity ($r/D \approx 0.8$), the decelerating zone ($r/D \gtrsim 0.8$) and a zone where the influence of the impingement is not dominant any more ($r/D \gtrsim 2.5$). According to the parameters, the position of the maximum radial velocity changes slightly. For the flow description, the radial positions $r/D = 0.3$, 0.8, 1.4 and 3.5 are chosen.

The first row of figure 4.26 shows the radial velocity u_r at the wall distance of $y/D = 0.05$. Starting from the stagnation point it strongly increases due to the stagnation point pressure and reaches a maximum value that is lower than the inlet velocity v_∞. In the first column, the influence of the Mach number is shown. The radial velocity slightly decreases with increasing Ma. The influence of the Reynolds number (second column) is stronger distinct. u_r decreases with increasing Re. The position of the maximum moves to greater r/D. In this plot and for all further comparisons, simulation #2 and #3 have to be compared to each other. Simulations #5 and #6 are another pair. The pairs (#2,3) and (#5,6) differ by the Mach number as well as the ambient and wall temperature (see table 2.3). Another noticeable characteristic is that the maximal radial velocity decreases and the position of the maximum moves closer to the stagnation point when the environment and the walls are heated (third column of figure 4.26).

In the considered height $y/D = 0.05$, all simulations have a negative axial velocity (approximately 10 to 14 % of the inflow velocity) close to the stagnation point (second row of figure 4.26). This means that the flow approaches the wall. Moving in the radial direction, this component turns slightly positive (up to 2 percent of inlet velocity). This is a consequence of the thickening of the wall jet: the flow spreads in the positive y direction.

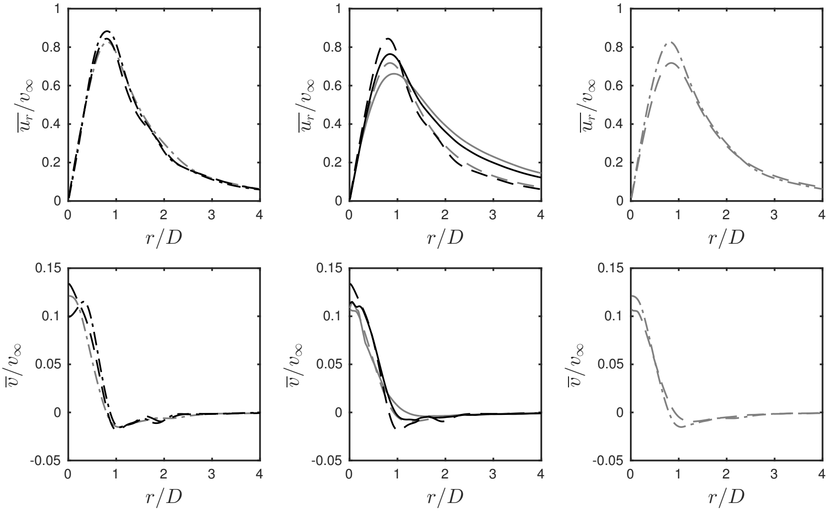

Figure 4.26: Mean profiles of radial velocity u_r (top) and axial velocity v (bottom) at $y/D = 0.05$. Left: influence of the Mach number *Ma*: #4 (0.41), #5 (0.78), #1 (1.11); middle: influence of the Reynolds number *Re*: #2,5 (3300), #3,6 (8000); right: influence of a heated environment: #2 (not heated: $\Delta T = 0$ K), #1 (heated: $\Delta T = 80$ K). – · –: #1, — —: #2, ——: #3, – · –: #4, — —: #5, ——: #6.

The radial position where the direction turns (zero crossing) decreases with increasing *Ma* (first column), decreasing *Re* (second column) and a heated environment (third column). After reaching a maximum value, depending on the configuration, the axial velocity decreases and features weak local maxima. The simulation with the lowest Mach number (#4) differs from those with higher *Ma* in the fact that the maximum axial velocity is not in the stagnation point, but at $r/D \approx 0.32$.

Figure 4.27 shows the mean temperature profiles of the impinging jets. The temperature curve is influenced by three effects: a) the mixing of the wall jet with the hot environment (cases #1,4,5,6). This causes the main trend of increasing temperature with increasing r/D. b) Heat transfer at the isothermal wall, which is discussed in chapter 6, and c) compressibility

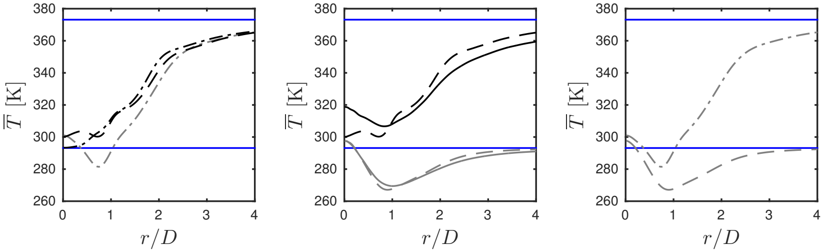

Figure 4.27: Mean profiles of temperature T at $y/D = 0.05$. Left: influence of the Mach number Ma: #4 (0.41), #5 (0.78), #1 (1.11); middle: influence of the Reynolds number Re: #2,5 (3300), #3,6 (8000); right: influence of a heated environment: #2 (not heated: $\Delta T = 0$ K), #1 (heated: $\Delta T = 80$ K). –·–·: #1, – –: #2, ——: #3, –·–·: #4, – –: #5, ——: #6, ——: reference temperatures: wall and total inlet temperature, see table 2.3.

effects. The first column shows the influence of the Mach number. At low Ma (#4; $Ma = 0.41$), the average temperature reaches the value of the total inlet temperature $T_{t,in}$ in the stagnation point. At higher Mach number (sub- and supersonic jets), the stagnation point temperature is higher than $T_{t,in}$. This indicates that the stagnation point is less unsteady when the Mach number is low. An unsteady stagnation point means mixing with the surrounding fluid and in case of a present temperature difference, an increasing temperature in the stagnation point.

The effect of compressibility can be seen in areas with a high (radial) velocity. A high velocity leads to a decreasing temperature, e.g. at $r/D \approx 0.8$, the supersonic case (#1) features a global minimum at the point where the axial velocity is maximal (first column). The same effect is present for the high subsonic jet (#5). The position of the decreased temperature variates, with respect to Ma, Re, and the hot environment, in accordance with the position of the high axial velocity.

4.6 Boundary layer

In section 4.1.3, the appropriate resolution of the viscous sublayer, as part of the boundary layer, was shown. In this section, the influences of the parameters Ma, Re and ΔT on the entire boundary layer are analysed. Therefore, two more dimensionless quantities are needed, since it is common practice to plot the dimensionless velocity u^+ and $\sim$ temperature T^+ as function of the $\sim$ wall distance y^+ (equation (4.3)):

$$\begin{aligned} u^+ &= \frac{\sqrt{u^2 + w^2}}{u_\tau} \\ T^+ &= \frac{T_w - T}{T_\tau} \, , \end{aligned} \tag{4.7}$$

where T_τ is the friction temperature:

$$T_\tau = \frac{q_w}{\rho c_p u_\tau} \, . \tag{4.8}$$

Those profiles are especially known for boundary layers where the fluid flows in one direction of a Cartesian coordinate system. In the case of the impinging jet, the wall-parallel velocity $\sqrt{u^2 + w^2} = \sqrt{u_\theta^2 + u_r^2}$ is used instead of u.

The rest of this section is taken from Wilke & Sesterhenn (2016c). Minor changes have been applied. Figure 4.28 shows the velocity boundary layer. y^+ and u^+ are the dimensionless wall distance and velocity. The u^+-profile of the wall jet is for all computations and r/D lower than the solution of the channel flow. The maximum is caused by the fact that the wall jet has a finite thickness. The fluid above the wall jet is almost at rest, neglecting a slight recirculation. The profile is strongest influenced by the Reynolds number, followed by the heated environment (ΔT). The Mach number has a small influence, except for $r/D = 1.4$. Increasing Ma leads to a movement of the u^+-maximum to higher values of y^+.

Also here, $r/D = 1.4$ forms an exception. For radial distances other than $r/D = 0.8$, the dimensionless velocity increases with increasing Mach number. The entire profile is raised with the Reynolds number. A heated environment has the impact that u^+ decreases in the entire domain. The vertical position (y^+) of the u^+-maximum increases for $r/D = 0.3$ and 0.8 and then decreases for larger radial distances. If we compare the profiles regarding the radial distance, the maximal values of y^+ and u^+ increase until $r/D = 1.4$ and then decrease slightly. Additionally, the drop after the maximum gets sharper until $r/D = 1.4$.

Contrary to the velocity, the thermal boundary layer profile, which is shown in figure 4.29, can be below or exceed the channel flow profile ($T^+ = Pr\ y^+$). In the case of the heated environment, the curves are close to $T^+ = Pr\ y^+$, depending on the radial position either until $y^+ \approx 5$ or until $y^+ \approx 10$. The influence of the Mach number is much stronger than in the velocity profile. The plots in the first row at $r/D = 0.3$ are in the mixing layer. That's why T^+ increases again at high values of y^+. Here, we concentrate on the range before ($y^+ \lesssim 70$). Increasing Mach numbers lead to increasing values of the dimensionless temperature until the maximum is reached, except for the radial distance $r/D = 1.4$. No trend regarding the position of the maximum can be determined. An increasing Reynolds number leads to increasing values of T^+ and the radial position where the maximum is observed. However, when the environment is not heated, the Reynolds number has almost no effect until the maximum is reached and until $r/D \leq 0.8$. The heated environment leads to much higher values of T^+ in the entire domain.

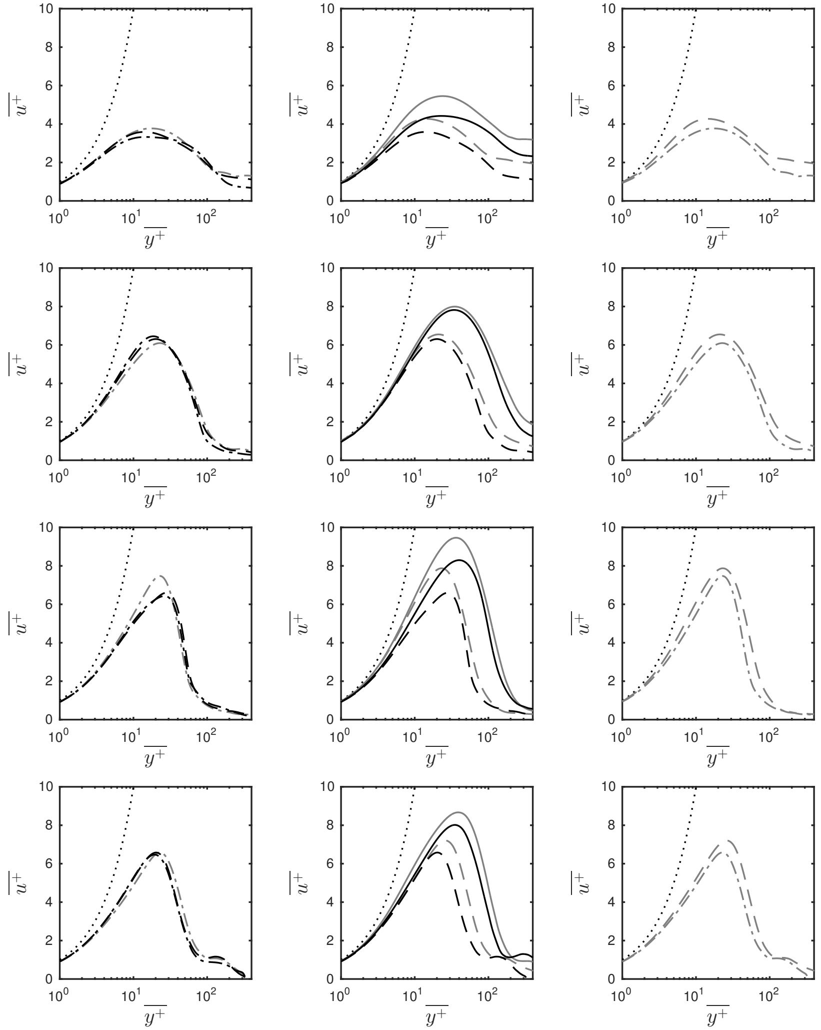

Figure 4.28: Velocity boundary layer for different radial positions (↓: $r/D =$ 0.3, 0.8, 1.4 and 3.5). Left: influence of the Mach number *Ma*: #4 (0.41), #5 (0.78), #1 (1.11); middle: influence of the Reynolds number *Re*: #2,5 (3300), #3,6 (8000); right: influence of a heated environment: #2 (not heated: $\Delta T = 0$ K), #1 (heated: $\Delta T = 80$ K). –·–·–: #1, – –: #2, ——: #3, –·–·–: #4, – –: #5, ——: #6, ……: $u^+ = y^+$.

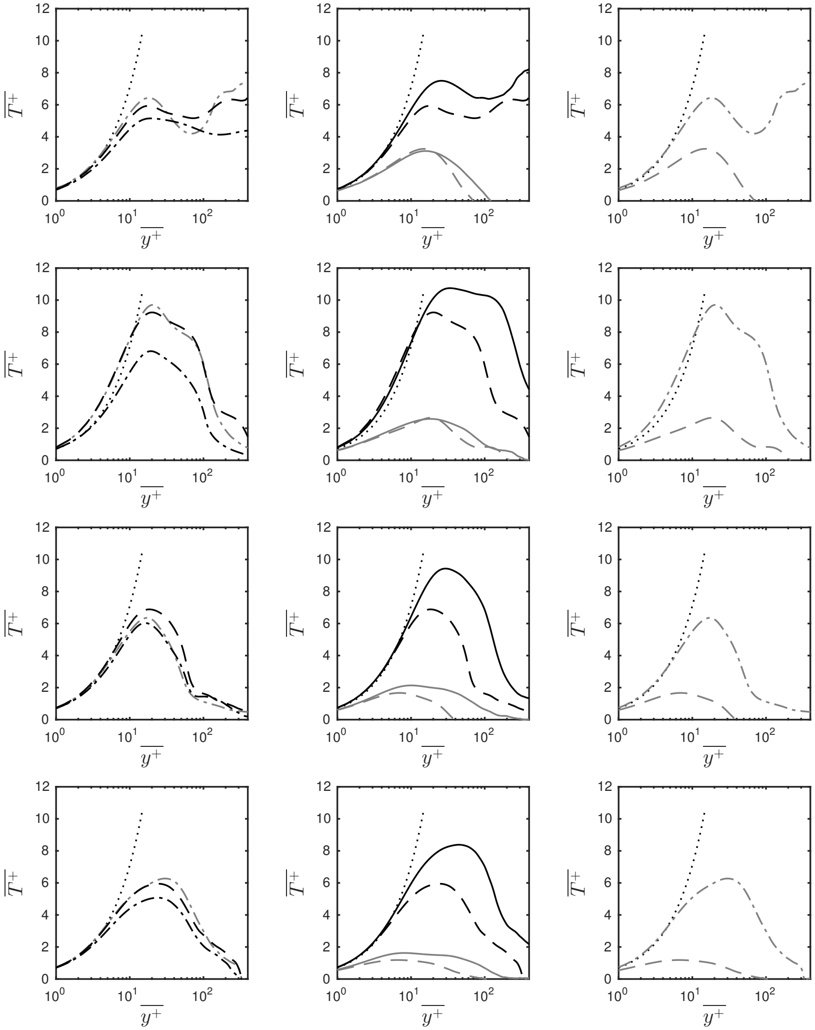

Figure 4.29: Temperature boundary layer for different radial positions (↓: r/D = 0.3, 0.8, 1.4 and 3.5). Left: influence of the Mach number *Ma*: #4 (0.41), #5 (0.78), #1 (1.11); middle: influence of the Reynolds number *Re*: #2,5 (3300), #3,6 (8000); right: influence of a heated environment: #2 (not heated: ΔT = 0 K), #1 (heated: ΔT = 80 K). – · – ·: #1, — —: #2, ——: #3, – · – ·: #4, — —: #5, ——: #6, ...: $T^+ = Pr\, y^+$.

5 The impinging tone

Sections 5.1, 5.2 and 5.4 are taken from Wilke & Sesterhenn (2016b) and Wilke & Sesterhenn (2017). Minor changes have been applied.

5.1 Sound source mechanism for low supersonic flow

In section 4.3.2, we have studied the cycle of the dominant dynamic mode of the supersonic impinging jet. Standoff shocks periodically appear and interact with vortices leading to the creation of very strong pressure waves. In fact, two different types of interaction occur, which are analysed in detail within sections 5.1.1 and 5.1.2.

5.1.1 Type 1: Shock-vortex-interaction

This kind of sound-emitting interaction requires two components: One shock and one vortex or an aggregation of vortices. The computational results show that multiple shocks can occur near by the stagnation point. Usually two or three shocks are simultaneously present. The system of shocks is highly unsteady within a periodical cycle.

Shock-vortex-interactions occur also in free jets, as described by Peña Fernández & Sesterhenn (2015). However, the strength of the shock due to the impinging plate is much stronger than the one in the shock cell system due to the under-expansion of the jet. This results in much higher sound pressure levels in the case of a present impinging plate, on which this thesis is focused. Therefore, the term *shock* refers here always to *standoff-shock*.

This sound source mechanism can involve either the main vortical structure of the impinging jet, which are the vortex rings or a vortex within a turbulent aggregation of vortices. The first case is typical for low Reynolds numbers, like $Re = 3300$ and was found by Wilke & Sesterhenn (2016a). With increasing Reynolds number, the phenomenon shifts to the second case. In the following, the mechanism is explained using figure 5.1, which shows snapshots of simulation #3 with $Re = 8000$. All snapshots are a section of a slice through the jet axis. In the first column, normalised values of Q and of the divergence of the velocity field $\mathrm{div}\,(u)$ are shown. At the starting point (first row) three shocks are present. For this mechanism only the upper one ($y/D \approx 0.85$) plays a role. For simplicity, only that one is shown in the sketch. Additionally, a slightly asymmetric vortex ring (1a,1b) is present. The centre of the ring in the left shear layer (1a) is at the same height of the shock, whereas the centre of the ring in the right side (1b) is closer to the wall. A bunch of turbulent vortices (3) is above the shock. The vortex (2a) is a fragment that is left from the next vortex ring that lost its symmetric structure due to leapfrogging. This process is explained in section 4.3.2. At this point in time, the shock keeps its position due to an equilibrium between the stagnation pressure pushing the shock up and the flow pushing the shock down to the wall. The vortices however are transported by the jet with high velocity and approach the impinging plate. The vortex ring (1a,1b) is transported in the wall-normal direction around the shock without interaction. Vortex (3), on the contrary, crashes into the right end of the shock. As a consequence, the shock looses its equilibrium, turns left and accelerates strongly. This can be seen in the second row of figure 5.1. Now, the vortex bunch (3) already cut the right end of the shock. The shock transformed into a pressure wave and is now (third row of figure 5.1) in between the two vortices (1a) and (3), moving in the north-west direction. At this point there are two possibilities for the pressure wave. The first option is shown in the forth row of figure 5.1: no vortex is in the way and the pressure wave can expand without disturbance.

Here, the wave can pass between vortices (1a) and (2a). In this case, the wave leaves the jet and does not trigger a feedback loop. More often is the case that there is no gap for the wave to escape and the wave interacts with another vortex that changes the direction of the wave. In this case, the wave goes through the whole jet and triggers another instability at the nozzle lip.

Important for this mechanism is a flow field that is at least slightly asymmetric. Within simulation #1 ($Re = 3300$), we observe a flow field that switches between a mainly symmetric and a clear asymmetric state. Also the mainly symmetric state is slightly distorted, so that one side of the vortex ring touches the shock slightly before the other side and leads to the described sound wave. Those two different states are explained in section 4.3.2.

5.1.2 Type 2: Shock-vortex-shock-interaction

The second kind of interaction that produces strong acoustic waves involves two shocks, a vortex ring and a sonic line. Figure 5.2 shows snapshots of simulation #3 ($Re = 8000$). All snapshots are a section of a slice through the jet axis. In the first column, normalised values of Q and of the divergence of the velocity field $\operatorname{div}(u)$ are shown. This mechanism requires a periodical appearance and disappearance of the supersonic zone close to the stagnation point. Details about the entire cycle are given in section 4.3.2. We start from a point in time where the supersonic zone close to the stagnation point was destroyed and a new one is transported downstream by the jet. This zone is circumscribed by the sonic line ($Ma = 1$). As long as no obstacles are in the way, the sonic line travels together with vortex rings, but slightly ahead of them. Travelling further downstream the supersonic zone encounters zones of high pressure, which are fragments of the high pressure at the stagnation point. As mentioned, typically there are multiple of such zones. In our example, we have three of them. Each time the sonic line faces a zone of high pressure, it stops its

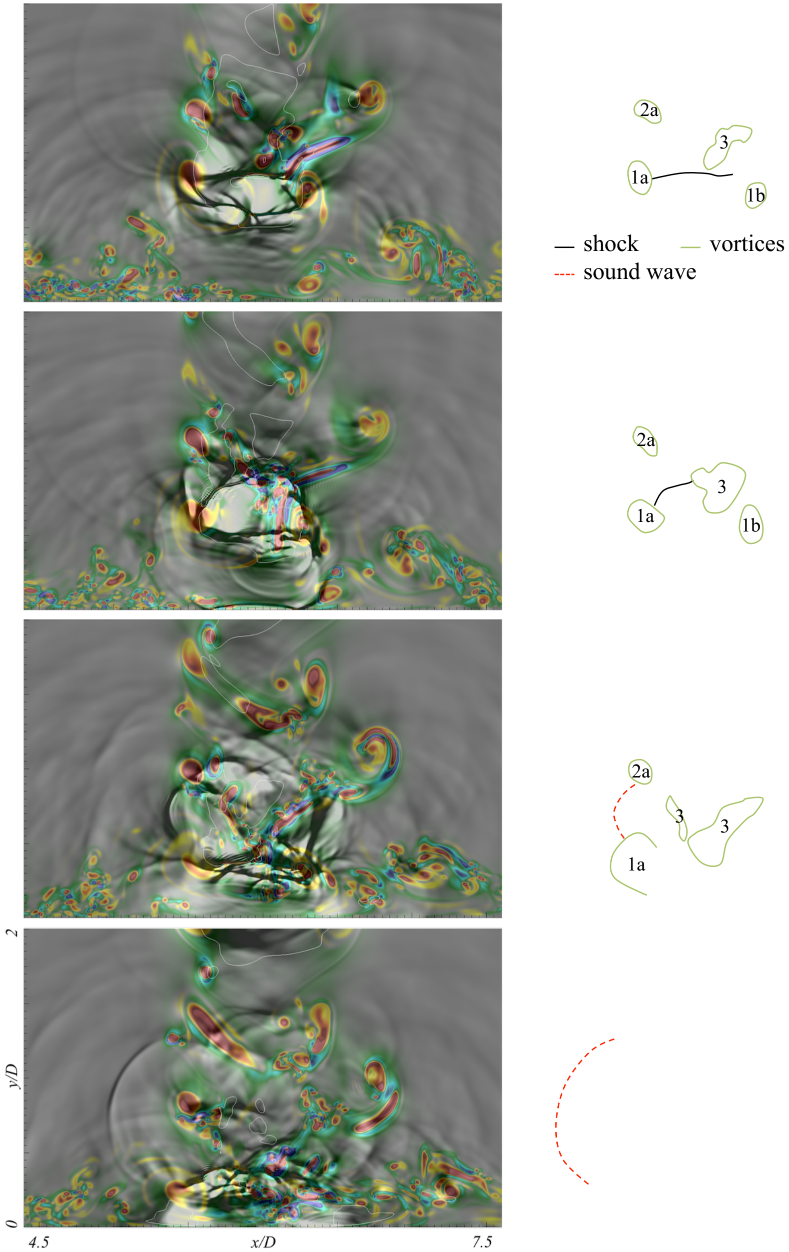
2a
3
1a
1b
shock
vortices
sound wave
2a
3
1a
1b
2a
3
3
1a
2
y/D
0
4.5
x/D
7.5

Figure 5.1: Shock-vortex-interaction (#3, *Re* = 8000). First column: normalised values of Q and of the divergence of the velocity field div (u). Second column: sketch. The snapshots (rows) are in consecutive order.

downstream movement for a while until the jet pushes the sonic line over the shock. The vortex rings travel in the shear layer, which is outside of the high pressure zone formed only in the core of the jet. Thus, they are not affected by those high pressure zones. As a consequence, the vortex rings approach the sonic line and interact. This means they influence the shape of the sonic line due to its rotating velocity components. In the first row of figure 5.2, the sonic line is confined by the shear layer of the jet in the radial direction. Streamwise it consists of three parts: on the left side, the sonic line coincides with the upper shock, whereas on the right side, it coincides with the lower shock. The crossover coincides with the inner border of the left side of the vortex ring. The sound wave is produced when this arrangement collapses: the vortex is not able anymore to separate the sub- and supersonic areas. This can be seen in the following two time steps (second and third row of figure 5.2). The sonic line looses its connection to the vortex ring and the upper shock and jumps to the lower shock so that the upper shock gets embedded in the supersonic zone. Thereby, a subsonic area is initially embedded and then collapses. A strong spheric pressure wave expands from that point. This one goes through the whole jet and reaches the nozzle. The phenomenon therefore triggers new instabilities of the shear layer and is part of a feedback mechanism.

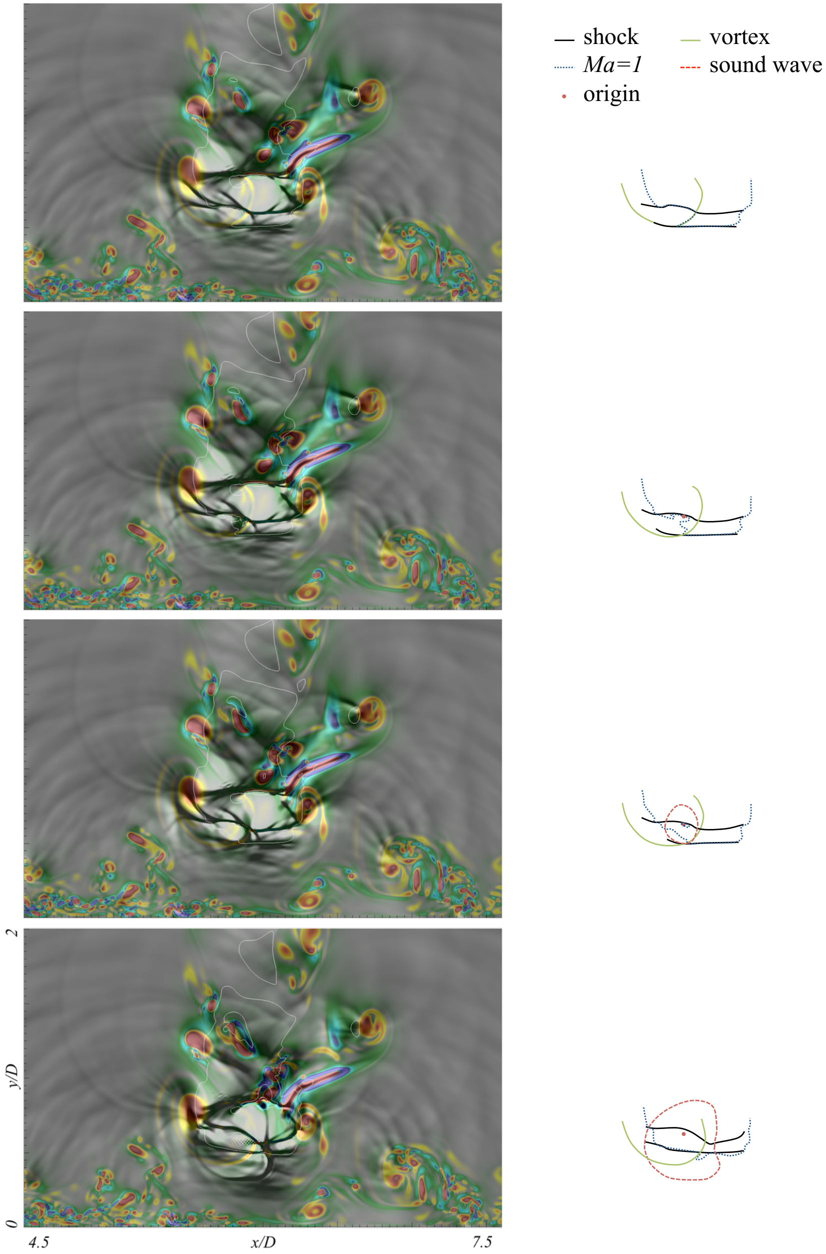
shock
vortex
Ma=1
sound wave
origin
2
y/D
0
4.5
x/D
7.5

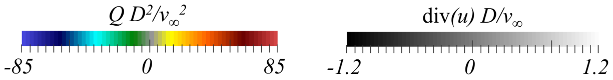

Figure 5.2: Shock-vortex-shock-interaction (#3, Re = 8000). First column: normalised values of Q and of the divergence of the velocity field div (u). Second column: sketch. The snapshots (rows) are in consecutive order.

5.1.3 Closure of the feedback loop

As stated in the introduction, it is generally accepted that a feeedback mechanism similar to the screech feedback loop is responsible for the impinging tones. No agreement could be found on how the loop works in detail: if the primary vortices impinging on the wall or the oscillations of the standoff shock close the feedback loop. Following the description of Raman (1998) of the free jet screech feedback loop, we apply the same steps for the impinging tone feedback loop:

1. Jet instability
2. Feedback wave produced by shock-vortex-interaction
3. Upstream propagation of feedback-wave
4. Receptivity at nozzle lip

Vortex rings (primary vortices) develop axisymmetric in the shear layer of the free jet region due to a Kelvin-Helmholtz instability (1) and perform leapfrogging as well as vortex split-offs, as described in section section 4.2.2. Vortices interact with the standoff shocks, as described in sections 5.1.1 and 5.1.2, in form of shock-vortex- or shock-vortex-shock-interactions and produce strong pressure waves (2). Except for the special case where the wave can leave the jet undisturbed, those waves usually interact again with structures of the jet and propagate as feedback-waves upstream (3).

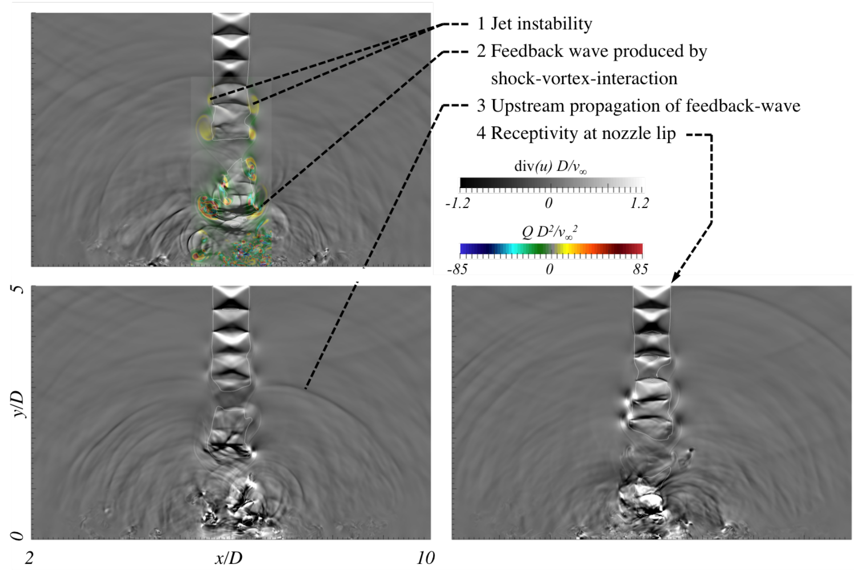

Figure 5.3: Feedback loop of a supersonic impinging jet at $Re = 8000$ (#3), inspired by the nomenclature of Raman (1998), figure 1.

Reaching the nozzle lip, they trigger new instabilities at the shear layer (4). The feedback loop is illustrated in figure 5.3. The DMD showed that it is not only one wave that triggers another wave through a direct feedback. In fact, a much more complex cycle (section 4.3.2) involving a periodical formation of head vortices and a destruction of the supersonic zone close to the stagnation point is responsible for the impinging tones.

5.2 Emanated sound

In order to obtain the sound spectra, the pressure was recorded in the near-field on three different cylinders around the jet axis at distances of two, three and four diameters. For the presented results, the position $r/D = 4$ and $y/D = 5$ was chosen. The upper wall has the advantage that the

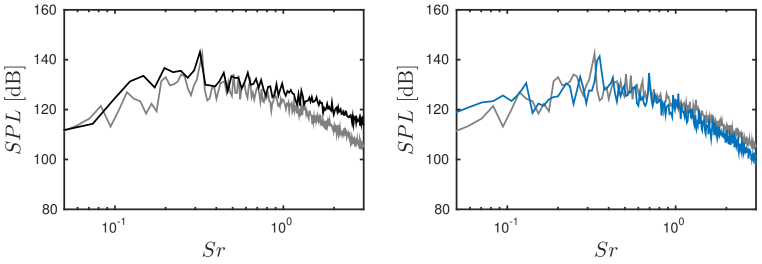

(a) Influence of Re ($\Delta T = 0$ K) **(b)** Influence of ΔT ($Re = 3300$)

Figure 5.4: Sound pressure level (SPL) of different configurations of the impinging jet. Reference pressure: $p_{ref} = 2 \cdot 10^{-5}$ Pa. —: #3 ($Re = 8000$, $\Delta T = 0$ K), —: #2 ($Re = 3300$, $\Delta T = 0$ K), —: #1 ($Re = 3300$, $\Delta T = 80$ K)

velocity is zero and no flow disturbs the acoustic measurements. The choice of the radius does not influence the investigated tones (frequencies), since the different distances only move the sound pressure level up and down. For each of the 256 circumferential positions, the spectra was computed using a fast Fourier transform (FFT). The spectra were then averaged.

Figure 5.4 shows the spectra for all three supersonic simulations. In (a), it can be seen that the frequency of the impinging tone is nearly independent of the Reynolds number in the range $3300 \leq Re \leq 8000$. Both simulations show a peek at $Sr = 0.32$ respectively $Sr = 0.33$. The frequencies of the impinging tones are summarised in table 5.1. The high-frequent noise increases with increasing Reynolds number. Taking a look at the frequencies of the tonal noise, we note that they correspond with the dynamic modes shown in section 4.3.2.

In figure 5.4b two impinging jets at $Re = 3300$ with different wall and ambient temperatures are compared. The values of the cold respectively hot case are $T_w = T_\infty = 293.15$ K and $T_w = T_\infty = 373.15$ K. The total inlet temperature of the jet was kept constant at $T_{t,in} = 293.15$ K. Heating the walls and therewith the ambient fluid leads to a shift of the impinging

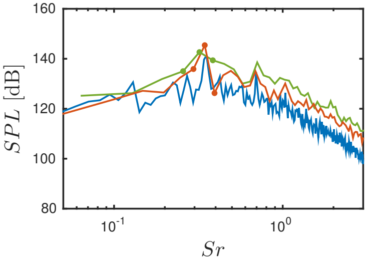

Figure 5.5: Sound pressure level (SPL) of impinging jet #1 ($Re = 3300$, $\Delta T = 80$ K) for different time spans. ——: mode A, ——: mode B, ——entire time span. Reference pressure: $p_{ref} = 2 \cdot 10^{-5}$ Pa.

tone to higher lower frequencies. However, the profile is very similar to the cold case. This is despite the existence of an additional mode in the hot case, as described in section 4.3.2.

In order to compare the noise emitted by those modes, the spectra were generated additionally for the specific time span of each mode. The time spans are identical with the ones used for the dynamic mode decompositions. Figure 5.5 shows these spectra. It can be seen that the impinging tone is present in both cases. Furthermore, the frequency is nearly identical $Sr \approx 0.35$. The small discrepancy can be explained due to the short time spans and the following coarse resolution of the Strouhal number for deeper frequencies. The data points are marked around the impinging tone. Comparing the first harmonics, we see a much smaller discrepancy due to the higher resolution of the Strouhal number on a logarithmic axis. In conclusion, the impinging tone can be either produced by only one shock-vortex-interaction per cycle (mode A) or by multiple interactions per cycle: shock-vortex-interactions and shock-vortex-shock-interactions (mode B). The frequency of the cycle is equal for both cases and is characterised by the formation of a head vortex, which is either one vortex ring or multiple vortices merged due to the leapfrogging mechanism.

N°	$T_\infty = T_w$ [K]	Re	t_{SPL} [s]	Sr_{SPL}	Sr_{DMD}
#1	373.15	3300	0.250	0.353	
#1 A	373.15	3300	0.046	0.352*	0.345
#1 B	373.15	3300	0.060	0.345*	0.340
#2	293.15	3300	0.250	0.330	0.319
#3	293.15	8000	0.120	0.320	0.324

Table 5.1: Dimensionless frequencies of the impinging tones as observed in the spectra Sr_{SPL} and in the dynamic mode decomposition Sr_{DMD}
* computed using the half frequency of the first harmonic of the tone. This is done, because the time span used for the spectrum t_{SPL} is relatively short and therefore the resolution of the impinging tone frequency is coarse.

5.3 Comparison to a free jet

Henderson (2002) proposed that tones generated by impinging jets with $5 \leq h/D \leq 10$ may be related to screech noise. In section 5.1, we could precisely identify the sound sources within the impinging jet. The strongest pressure waves are emitted from interactions between vortices and standoff shocks. Therefore, impinging tones could be clearly delimited from screech. Nevertheless, in this section a brief comparison to free jet screech is given. The supersonic impinging jet #1 with $Re = 3300$ and $\Delta T = 80$ K is compared to a free jet with equal parameters.

5.3.1 Impinging tone and screech

First, we want to compare the emanated sound. As mentioned in the literature review (section 1.3), the source of screech noise is located between the rear edge of the third and the fifth shock cell. The exact position depends on the mode and therefore on the nozzle pressure ratio. For the investigated NPR of 2.15, the free jet modes A and B are relevant. According to Umeda & Ishii (2001), the corresponding cells are the third respectively third or fourth. The supersonic impinging jets investigated in this thesis have a nozzle-to-plate distance of five diameters and a nozzle

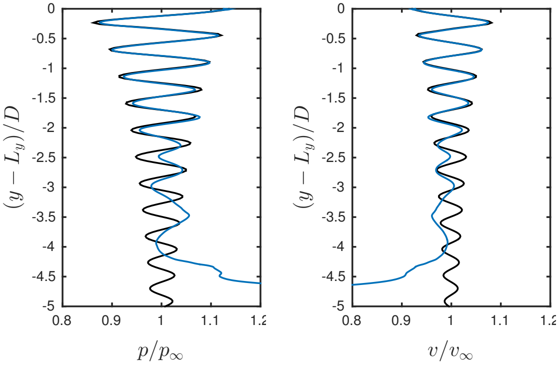

Figure 5.6: Pressure (left) and axial velocity (right) profiles along the axis of the free (——) and the impinging jet (——).

pressure ratio of 2.15. Consequently, more than five shock cells develop and screech can occur. The screech frequency depends on the shock cell spacing. Figure 5.6 shows pressure and axial velocity along the axis of the free and the impinging jet. It can be seen that the first four shock cells have the identical position in both cases. Therefore, we can conclude that if screech occurred within the impinging jet, it would have exactly the same frequency as free jet screech.

The fifth shock cell of the impinging jet is slightly displaced downstream and the sixth cell coincides again. Furthermore, we observe that the amplitude of the oscillation as well as the value around which the axial velocity fluctuates is decreased. For distances from the nozzle larger than three diameters, the shock cells of the impinging jet are stronger and stronger influenced and disappear.

Figure 5.7 confronts the noise spectrum of the impinging jet with the one of the free jet. The former features a discrete tone with a Strouhal number of $Sr = 0.353$ accompanied by the first harmonic, whereas the tone of the latter is at $Sr = 0.375$ and misses its harmonic. The frequency of the impinging tone differs from the screech frequency. Furthermore,

Figure 5.7: Sound pressure level (SPL) of the impinging (——, $\chi = 90°$) and the free jet at different observation angles ——: $\chi = 90°$, ——$\chi = 150°$. Reference pressure: $2 \cdot 10^{-5}$ Pa.

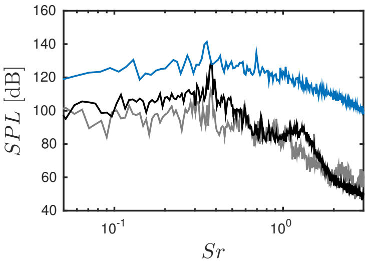

the sound pressure level of the impinging jet is more than 20 dB higher compared to the free jet. Screech may appear additionally to impinging tones, but impinging tones are different from screech. The two main sound source mechanisms within the impinging jet, namely the (standoff) shock-vortex and the (standoff) shock-vortex-(standoff) shock interaction, exceed any possible screech and are of much higher relevance with respect to the emission of noise.

5.3.2 Impinging jet and free jet modes

In figure 5.8, the corresponding three-dimensional modes to the tonal noise components are shown. Contours of pressure are depicted. In the case of the impinging jet (left, $p = \pm 0.05 p_\infty$), the mode is toroidal, as described in section 4.3.2. On the contrary, the observed screech mode of the free jet ($p = \pm 0.002 p_\infty$) with a frequency of $Sr = 0.375$ is a superposition of two helical modes with $Sr = 0.353$ and $Sr = 0.399$.

This observation indicates that the correspondence of the fully-expanded Mach number to modal structure might be distorted caused by a heated environment. From figure 1.6, which is based on the measurements of Panda et al. (1997), one would expect a toroidal mode appearing at $Ma_\infty = 1.11$. The detected mode however fits into the range of mode B, which can be helical as well.

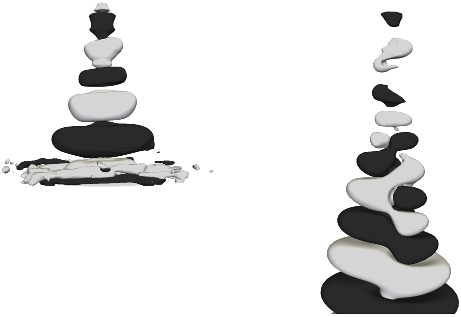

Figure 5.8: Pressure contours of the tree-dimensional dynamic modes corresponding to the impinging tone (left, #1, $Sr = 0.353$, $p = \pm 0.05 p_\infty$) and to screech (right, free jet, $Sr = 0.375$, $p = \pm 0.002 p_\infty$).

5.4 Zone of silence

As stated in the introduction, a hypothesis explaining the sound source mechanism according to Sinibaldi et al. (2015) can be summarised as follows: In the pre-silence region no standoff shock is present. Vortices interact directly with the impinging plate (direct shear layer-plate interaction). In the post-silence region the standoff shock disturbs the vortex-wall-interaction. The tones are only related to strong oscillations of the standoff shock. In the zone of silence, a smooth change between those two behaviours is observed.

The presently described simulations with $h/D = 5$ and $NPR = 2.15$ are located in the pre-silence zone. However, we clearly observe standoff shocks in the numerical data. As described in the previous sections, the impinging tones are not caused by direct vortex-plate interactions, but rather due to shock-vortex- or shock-vortex-shock-interactions. The observation of standoff shocks in the pre-silence zone is supported by the experiments of Buchmann et al. (2012). In their figure 2, schlieren images are shown for such a case ($h/D = 4, NPR = 3.2$) with present standoff shocks.

A hypothesis that explains the observations can be formulated as follows: Standoff shocks are present in both, the pre- and the post-silence zone. However, those shocks differ. In the pre-silence zone there is enough space for the jet shock cell system to damp before the flow reaches the impinging plate. Therefore, shocks can appear, disappear and move between the wall and the shock cell system. Those moving shocks are difficult to detect in statistical values like root-mean-squares of velocity fluctuations. However, they can be observed using DNS or schlieren. In the post-silence zone, the impinging plate is directly located in the strong shock cells of the free jet and form a quasi-stationary system. Hence, they can be detected more easily in statistical data.

6 Heat transfer

Sections 6.1 and 6.2 are taken from Wilke & Sesterhenn (2016c). The sections have been rearranged and slightly modified.

6.1 Modes and heat transfer

6.1.1 Nusselt number

In section 4.2.1, it is shown that the movement of a pair of vortices in the vicinity of the impinging plate temporally enhances the local heat transfer. Furthermore, in section 4.3.1 we saw that those toroidal vortices occur periodically with a dimensionless frequency of $Sr = 0.46$ accompanied by the first harmonic. In the following, we want to analyse the effect on the time-averaged heat transfer.

In figure 6.1, the Nusselt number distribution of the simulations with $T_\infty = T_w > T_{t,in}$ are compared. The influence of the Mach number (left) is strongest in the vicinity of the stagnation point. The simulation with the lowest compressibility ($Ma = 0.41$) has the global maximum at approximately $r/D = 0.3$ and not at the axis. Nu increases with increasing Ma at the stagnation point. This is an indication of stronger fluctuations and consequently an increased contribution of the turbulent heat flux which is quantified in section 6.1.2. This observation is consistent with the remarks concerning the movement of high pressure within the deflection zone, as described in section section 4.4.

Figure 6.1 further shows that Nu decreases with increasing radial distance. Superimposed to this main trend, a shoulder exists at $1 \lesssim$

$r/D \lesssim 2$ where the slope is reduced. Depending on the parameters of the impinging jet, the slope can also be positive in this area and form a secondary maximum. This zone of higher time-averaged heat transfer coincides with the one where temporally enhanced heat transfer occurs, as described in section 4.2.1.

Buchlin (2011) investigated impinging jets with much higher Reynolds numbers up to 60000 where the total inlet temperature is equal to the ambient temperature $T_{t,in} = T_\infty \neq T_w$. This configuration differs to the one used within this section: $T_{t,in} > T_\infty = T_w$. However, both results have in common that a secondary maximum or shoulder of the Nusselt number exists. Within this dissertation the distinctness of the Nu shoulder decreases when Re increases from 3300 to 8000. Buchlin found that the opposite is the case when the Reynolds number increases from 24000 to 60000.

Nusselt number correlations of the shape $Nu \sim Re^m$ are in wide use. According to Lee & Lee (1999), the exponents for plate distances of 4 respectively 6 diameters are: $m = 0.53$ and $m = 0.58$. For the presently investigated simulations with $h/D = 5$ the exponent 0.555 was chosen. The influence of the Reynolds number is illustrated in figure 6.1 (middle and right). As expected, the heat transfer increases with Re. The scaling fits away from the stagnation point $r/D \gtrsim 1$. According to the simple correlation, the heat transfer in the area around the stagnation point is weaker for the higher Reynolds number of 8000 than in the case of $Re = 3300$.

The exponent of Nu-Re-correlations is consistently reported by different authors to be roughly 0.5 to 0.6. On the contrary, the prefactor strongly depends on the cooling configuration, measurement position, method of averaging and especially the shape of the nozzle (Janetzke (2010)). For this reason Nusselt numbers predicted using such correlations differ by a factor of up to 2.4 and can only give a rough estimate of impingement heat transfer. Figure 6.2 shows correlations of different authors estimating the

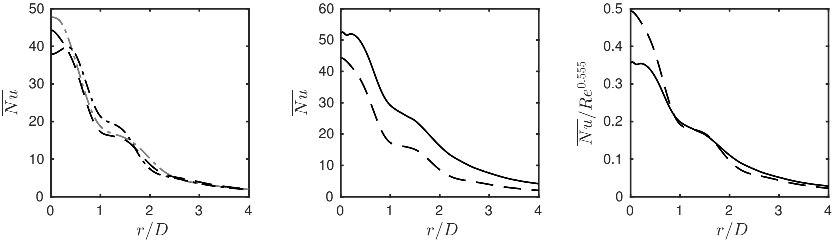

Figure 6.1: Nusselt number Nu for different impinging jet configurations. Left: influence of the Mach number #4 (0.4), #5 (0.8), #1 (1.1), middle: influence of the Reynolds number #5 (3300), #6 (8000), right: scaled Nu profiles. – · – ·: #1, – · – ·: #4, — —: #5, ——: #6.

Figure 6.2: Stagnation point nusselt number depending on Reynolds number. Adapted from Janetzke (2010), experimental data from different autors: — —: single jet, ——: array. Own simulations: square: #4 ($Ma = 0.41$), point: #5, #6 ($Ma = 0.78$), triangle: #1 ($Ma = 1.11$).

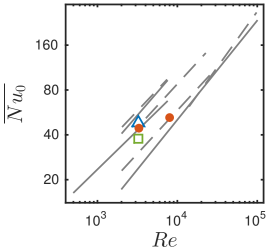

stagnation point Nusselt number Nu_0. The simulations carried out within this dissertation are added. It can be observed that all four simulations lay within the corridor described by experimental data. Further can be seen that the common neglect of the Mach number leads to a variation in Nu_0 of 26% comparing simulations #4 ($Ma = 0.41$) and #1 ($Ma = 1.11$).

6.1.2 Turbulent heat flux

Looking at the turbulent heat flux, we can quantify the contribution of the pair of vortex rings to the time averaged heat transfer. The first row of figure 6.3 shows the turbulent heat flux in the wall-normal direction $\overline{\rho v'' e''}$. Close to the wall, $\overline{\rho v'' e''}$ is positive in the area of the Nu shoulder (left plot, $r/D = 1.4$). This means that the heat is transported in the positive

y-direction (away from the impinging plate). After reaching a maximum at $y^+ \approx 15$ to 20, the heat flux decreases and turns negative. This is due to the fact that vortices present at the upper border of the wall jet entrain hot fluid. The radial distribution at $y^+ = 15$ (middle plot) proves that the zone where the turbulent heat flux is strongly positive coincides with the Nu shoulder. On the right and left of this zone, $\overline{\rho v''e''}$ is negative for the lower Reynolds number. Further can be determined that, in this zone, the influence of $\overline{\rho v''e''}$ is weaker at the higher Reynolds number. This agrees with the fact that the Nu profile is smoother and that the vortex rings are not generated in each cycle.

The second row of figure 6.3 shows the turbulent heat transfer in the radial direction $\overline{\rho u_r''e''}$. It is of the same order of magnitude as the one in the wall-normal direction. Close to the wall, $\overline{\rho v''e''}$ is positive at $r/D = 1.4$ for the case of $Re = 3300$. For the higher Reynolds number, this area of downstream turbulent heat flux is almost not present. $\overline{\rho v''e''}$ is negative at larger wall distances for both cases due to the direction of rotation of the vortices in the shear layers.

Furthermore, the turbulent wall-normal turbulent heat flux can quantify the influence of the fluctuations within the deflection zone. Looking at the top right plot of figure A.19, we see that $\overline{\rho v''e''}$ positively contributes to the cooling of the impinging plate at the axis for simulations with a high Mach number (#5, #1). At low Mach number (#4), no such effect is present. Due to the fact that results are available for multiple parameters ($Re, Ma, \Delta T$) and locations (y^+ or y/D, r/D), not all of them can be discussed within this dissertation. The graphs that give an insight into the physical effects that are of interest in this dissertation are explained. Further diagrams, which are not discussed, can be found in the appendix. However, these additional plots are valuable for validation purposes.

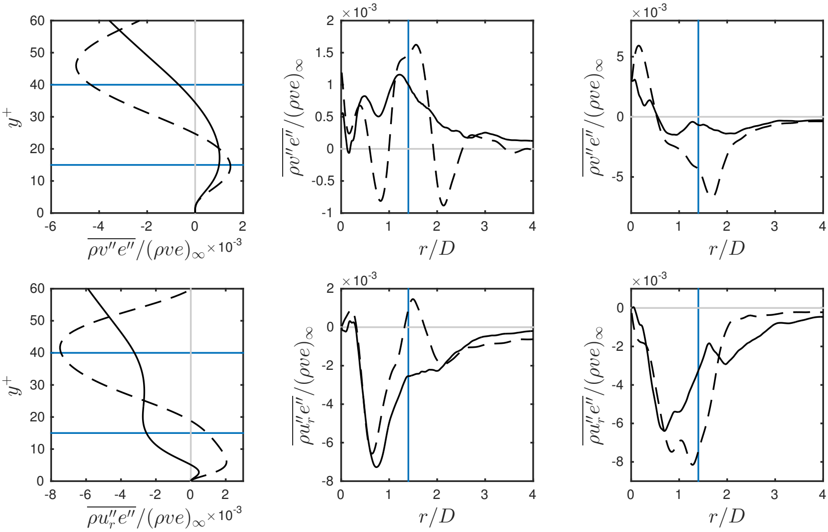

Figure 6.3: Influence of the Reynolds number (#5: 3300, #6: 8000) on the turbulent heat flux in the wall-normal direction $\overline{\rho v''e''}$ (first row) and radial direction $\overline{\rho u_r''e''}$ (second row). Left: $r/D = 1.4$, middle: $y^+ = 15$, right: $y^+ = 40$. — —: #5, ——: #6, ——: locations $r/D = 1.4$, $y^+ = 15$ and $y^+ = 40$.

6.1.3 Pulsating impinging jets

Within the previous sections, we could clearly ascribe an additional heat transfer to a pair of vortex rings that travels within the wall jet parallel to the impinging plate, until a certain axial distance. In Janetzke (2010), an experimental study was carried out in which a pulsation was applied at the inlet of a line array with three nozzles. Three zones according to the Strouhal number were observed. At low values of Sr, multiple ring vortices were generated within one cycle of the actuator. In the range $0.27 \lesssim Sr \lesssim 0.5$, exactly two ring vortices and for higher frequencies until $Sr = 0.95$, a single one was produced. Within that study, the heat transfer caused by the pulsating impinging jet was compared to a stationary reference case. The increase of the heat transfer effectivity (equation (1.9)) is shown in figure 1.3. An increase up to 40% was found for a Strouhal number of approximately 0.85 using the maximal amplitude (on/off). Unfortunately, the test rig did not allow to investigate lower frequencies ($Sr \lesssim 0.75$) with high amplitudes. Looking at figure 1.3, the contours indicate that the optimal Strouhal number lays below 0.8. The experiments were carried out at very low Mach number $Ma < 0.1$.

In this thesis, it is shown that the natural frequency of the vortex rings is $Sr = 0.46$ respectively $Sr = 0.54$ for $Ma = 0.78$ and $Ma = 0.41$. Following this trend, it is likely that a further decrease of the Mach number further increases the Strouhal number of the dominant mode. This means that a significant increase in heat transfer efficiency can be reached when pulsating with the naturally occurring frequency. This is also in agreement with the observation that two or more rings develop when the excitation frequency is too low. For instance, pulsating with half of the natural frequency produces two vortex rings.

In order to show that strong vortex rings can be generated when pulsating with that specific frequency, another simulation (#7) was set-up. First results are shown in Wilke & Sesterhenn (2017). The parameters are chosen, so that the average dynamic viscosity and mass flow are equal to simulation #4. An on/off-pulsation using a piecewise defined function consisting of constant and sinus parts was applied in order to approximate the opening and closing of a valve. Hence, the Reynolds number periodically fluctuates between zero and 6600. In order to avoid supersonic flow, the maximal nozzle pressure ratio for the pulsed impinging jet was chosen equal to simulation #5 and #6.

In the first row of figure 6.4, the vortical structure, represented by Q, of the non-pulsed (left) and the pulsed (right) impinging jet are confronted. A strong increase of the strength of the vortices proves that the eigenfrequency is a reasonable choice for the pulsation frequency. The second row of this figure reveals that a comparison to the unforced case

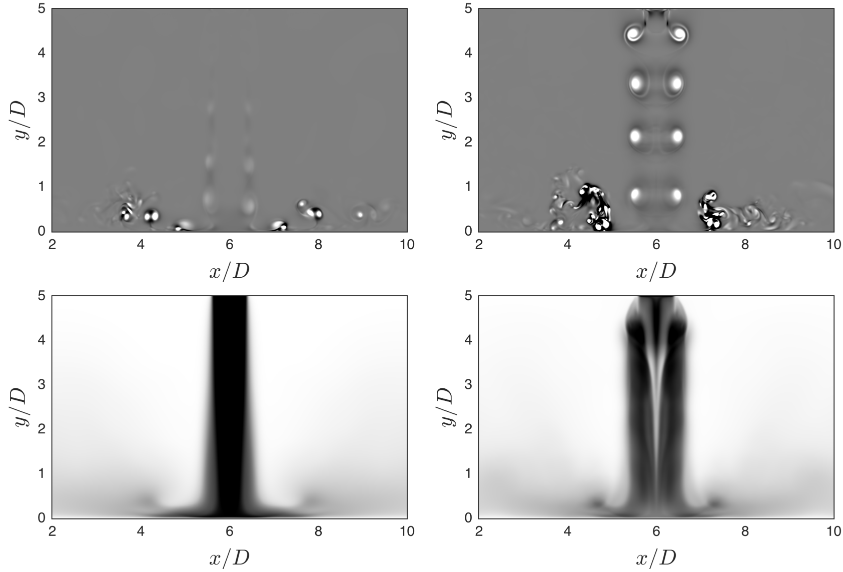

Figure 6.4: Confrontation of an unforced (#4, left) and forced (#7, right) impinging jet. First row: QD/v_∞^2 in the range of -30 (black) to 30 (white). Second row: average temperature from 293 K (black) to 373 K (white).

is not strait forward. The enhanced vortices entrain much more hot surrounding fluid. Therefore, the temperature difference used to compute the Nusselt number needs to be redefined. Within this thesis we pass on a detailed analysis of this simulation and continue with the unforced impinging jet.

6.2 Reynolds analogies and correlations

6.2.1 Mean field

For the development of turbulence models, relations between quantities affiliated to heat transfer and to momentum transfer are of great interest.

Reynolds discovered that the similarity of the momentum and energy equation for incompressible laminar boundary layers can be used to approximate the heat transfer with the use of the fluid friction, see Kakag & Yenner (1995):

$$St = \frac{Nu}{RePr} \approx \frac{C_f}{2} = \frac{\tau_w}{\rho v_\infty^2} \ . \tag{6.1}$$

Equation (6.1) is the well known Reynolds analogy. The assumption made is a Prandtl number equal to one. C_f and τ_w are the skin friction factor and the wall shear stress. This equation was modified by Chilton & Colburn (1934), based on experimental data:

$$StPr^{2/3} = \frac{Nu}{RePr^{1/3}} \approx \frac{C_f}{2} \tag{6.2}$$

and considers Prandtl numbers different from one. Equation 6.2 is referred to as the Chilton Colburn analogy. The first row of figure 6.5 shows the skin friction coefficients of the conducted simulations. The left plot indicates that C_f is almost independent of the Mach number in the range $0.41 \leq Ma \leq 1.11$. As expected, an increasing Reynolds number leads to a decreasing skin friction factor. However, the shape of the profile is not affected. In the middle plot, two pairs of simulations are shown: subsonic impinging jets (black solid line and black dashed line) and supersonic cases (grey solid line and grey dashed line). The difference between the pairs can be explained using the right plot. Comparing a jet with equal total inlet temperature $T_{t,in}$, ambient T_∞ and wall temperature T_w to another one with $T_\infty = T_w > T_{t,in}$, it can be seen that the skin friction factor increases due to the heated environment. The total inlet temperature has been kept constant.

The Reynolds (RA) and the Chilton Colburn analogies (CCA) are shown in figure 6.6. As they are developed for wall-bounded flows, the analogies are not suitable for the stagnation point region. In this region, the relative error is between approximately -80% and -40%. At the position

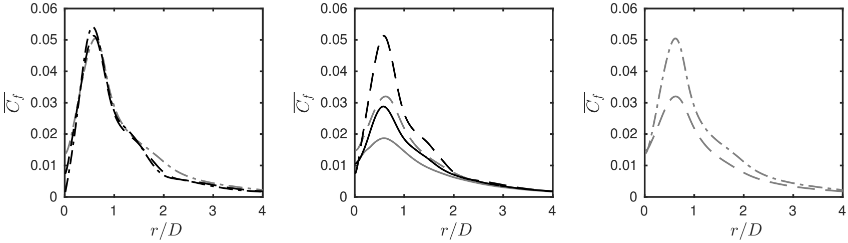

Figure 6.5: Skin friction factor C_f for different impinging jet configurations. Left: influence of the Mach number #4 (0.41), #5 (0.78), #1 (1.11), middle: influence of the Reynolds number #2,5 (3300), #3,6 (8000), right: influence of the ambient and wall temperature #2 ($\Delta T = 0$ K), #1 ($\Delta T = 80$ K). – · – ·: #1, — —: #2, ——: #3, – · – ·: #4, — —: #5, ——: #6.

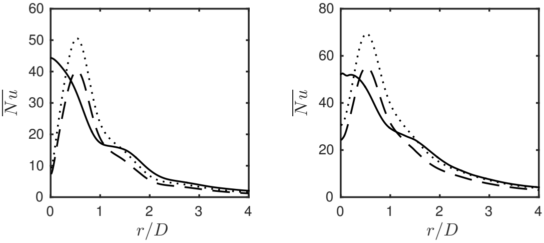

Figure 6.6: Heat transfer at the impinging plate (Nusselt number). Left: simulation #5, right: #6, ——: DNS data, — —: Reynolds analogy (RA), ...: Chilton Colburn analogy (CCA).

where C_f reaches its maximum, both analogies over-predict heat transfer: $\approx +30\%$ (RA) respectively $\approx +65\%$ (CCA). Farther away from the axis, at $r/D \gtrsim 2$, the analogies fit much better. The best agreement is found in the case of the higher Reynolds number using the CCA. Here, the error is between -9% and -4%.

Other relations involving mean temperature and mean velocity were developed by Crocco (1932) and Busemann (1931), Walz (1962) and Zhang et al. (2014). In the latter source, the derivation is explained in detail. All relations have the common form:

$$\frac{\overline{T}}{\overline{T}_\delta} = \frac{\overline{T}_w}{\overline{T}_\delta} + \frac{T_r - \overline{T}_w}{\overline{T}_\delta}\,\frac{\overline{u_r}}{\overline{u_r}_\delta} + \frac{\overline{T}_\delta - T_r}{\overline{T}_\delta}\left(\frac{\overline{u_r}}{\overline{u_r}_\delta}\right)^2 , \tag{6.3}$$

with

$$T_r = \overline{T}_\delta + r\frac{\overline{u_r}_\delta^2}{2c_p} . \tag{6.4}$$

The recovery factor r changes according to the authors. For $r = 1$, the Crocco-Busemann relation (CBR) is derived. In the Walz's equation or modified Crocco-Busemann relation $r = 0.88$. The generalized Reynolds analogy (GRA) proposed by Zhang et al. (2014) uses the general recovery factor according to equation 6.5:

$$r = \left(\overline{T}_w - \overline{T}_\delta\right)\frac{2c_p}{\overline{u_r}_\delta^2} - \frac{2Pr}{\overline{u_r}_\delta}\,\frac{\overline{q}_w}{\overline{\tau}_w} . \tag{6.5}$$

Those three relations were tested for the impinging jet. The difference between the Crocco-Busemann and Walz's equation was found to be negligible for the present simulations. For the reason of lucidity, the approximation according to Walz is not shown. Figure 6.7 shows the DNS data compared to the approximations of Crocco-Busemann and the GRA. The mean temperature and mean wall-parallel (radial) velocity are normalised by the values at the edge of the boundary layer (subscript $\delta = \delta_{99}$) as in Zhang et al. (2014). For both Reynolds numbers, the GRA fits better than the CBR for radial positions close to the stagnation point ($r/D = 0.3$ and $r/D = 0.8$). Farther away ($r/D = 1.4$ and $r/D = 3.5$), the opposite can be observed. This is a consequence of different curvatures of the DNS profiles and the fact that the scaled mean temperature is always predicted higher according to the GRA. Further can be ascertained that for $Re = 8000$ and $r/D = 0.8$, the GRA gives a precise prediction of the temperature field. At this radial position, the radial velocity has its maximum. Given that no de- and acceleration is present, the conditions

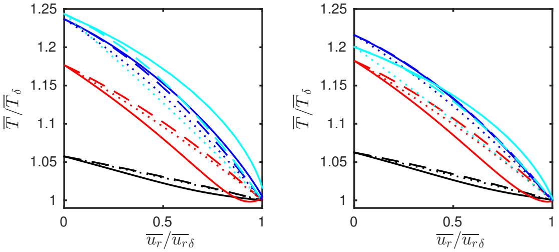

Figure 6.7: Relation between mean temperature and mean velocity in the wall jet. Left: simulation #5, right: #6. colors: —: $r/D = 0.3$, —: $r/D = 0.8$, —: $r/D = 1.4$, —: $r/D = 3.5$. pattern: —: DNS data, ...: Crocco-Busemann relation (CBR) – –: generalized Reynolds analogy (GRA).

are most similar to canonical compressible wall-bounded turbulent flows (CCWTFs), for which the relation was developed. In CCWTFs, the flow can be approximated as quasi-one-dimensional. Examples for such flows are pipes and channels.

6.2.2 Fluctuations

Additional to the relation between the mean temperature and velocity, Zhang et al. (2014) derived a general analogy for fluctuations:

$$T' - \frac{1}{\overline{Pr_t}} \frac{\partial \overline{T}}{\partial \overline{u}} u' + \phi' - \frac{\overline{(\rho v)' \phi'}}{\overline{(\rho v)' u'}} u' = 0 \, , \tag{6.6}$$

where ϕ' is a residual temperature that need to be modelled. The proposed model chosen by Zhang et al. (2014) for "convenience" is:

$$\phi' = \frac{\overline{(\rho v)' \phi'}}{\overline{(\rho v)' u'}} u' \, , \tag{6.7}$$

so that eq. 6.6 is reduced to:

$$T' = \frac{1}{\overline{Pr_t}} \frac{\partial \overline{T}}{\partial \overline{u}} u' \, . \tag{6.8}$$

Zhang et al. (2014) describe further that equation 6.8 is not valid, but the RMS of T' and u' can be approximated in a similar way:

$$\sqrt{\overline{T'^2}} \approx \left| \frac{1}{\overline{Pr_t}} \frac{\partial \overline{T}}{\partial \overline{u}} \right| \sqrt{\overline{u'^2}} \qquad \text{or} \qquad \sqrt{\overline{T'^2}} \approx \pm \frac{\overline{(\rho v)' \, T'}}{\overline{(\rho v)' \, u'}} \sqrt{\overline{u'^2}} \, . \tag{6.9}$$

The plus sign applies to the flow region where wall-normal gradients of mean temperature and velocity have the same sign. The minus sign applies to the opposite situation. This approximation fails in case of the impinging jet. In the boundary layer, the term $\overline{(\rho v)' \, u'}$ changes its sign. The approximation delivers huge values of $\sqrt{\overline{T'^2}}$ in the vicinity of the zero crossing. A further approximation is suggested by Zhang et al. (2014) that reduces the connection between temperature and velocity fluctuations to $R_{v'u'} \approx R_{v'T'}$. Where R is the Bravais-Pearson correlation coefficient. Also this approximation is invalid for the analysed impinging jets. Figure 6.8 exemplary shows scatter plots of simulation #6 ($Re = 8000, Ma \approx 0.78$) in the boundary layer at $13 \leq y^+ \leq 17$. In order to improve the rendering, the data was classified into 250 segments for each variable covering 95% of the velocity and 99% of all other fluctuations. The database consists of 550 equally spaced snapshots (symmetry planes) out of 175000 that have been computed after the flow reached its quasi-stationary state. The corresponding correlation coefficients are given in table 6.1 for the same y^+ value and additional for $38 \leq y^+ \leq 42$. It can be seen that neither the radial velocity nor the temperature is correlated to the axial velocity. Despite both coefficients are close to zero, it cannot be said that they are approximatively equal.

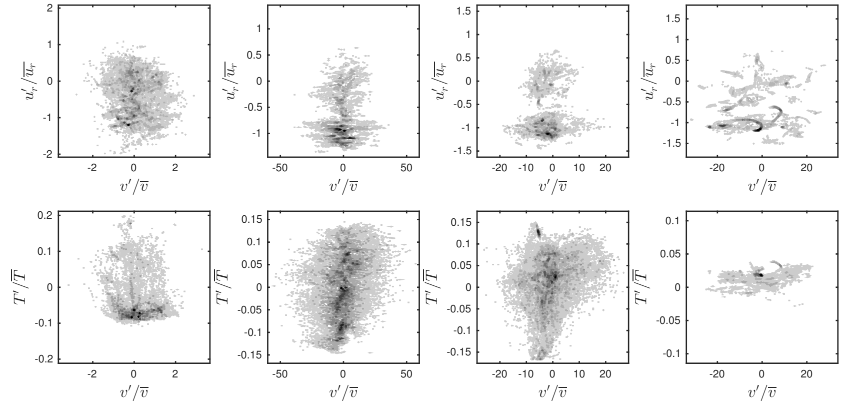

Figure 6.8: Scatter plots of radial velocity (first row) and temperature (second row) fluctuation against axial velocity fluctuation at $13 \leq y^+ \leq 17$ for different radial positions (→: $r/D = 0.3$, 0.8, 1.4 and 3.5), simulation #6.

6.2.3 Additional correlations

The derivation of Reynolds analogies is closely related to the development of models for compressible turbulence. For instance, a similar equation to equation 6.9 was derived by Rubesin (1990). He assumed that thermodynamic fluctuations behave in a polytropic manner:

$$\frac{p'}{\overline{p}} = n\frac{\rho'}{\overline{\rho}} = \frac{n}{n-1}\ \frac{\rho T''}{\overline{\rho}\widetilde{T}}\ . \tag{6.10}$$

After assuming that $T'/\,\overline{T} \approx T''/\,\widetilde{T}$ and linearisation according to Lechner et al. (2001) the relation

$$(n-1)\,\frac{\rho'}{\overline{\rho}} \approx \frac{\rho T'}{\overline{\rho}\ \overline{T}} \tag{6.11}$$

is derived. As suggested, with $n = 0$ it follows that the correlation coefficient $R_{\rho,T}$ is minus one, $R_{\rho,p} \approx 0$ and that pressure fluctuations are unimportant compared to density fluctuations. The correlation coefficient

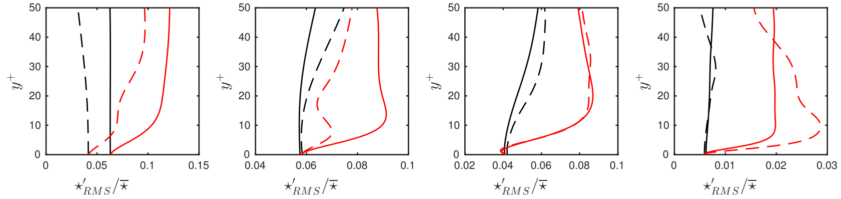

Figure 6.9: RMS values of pressure and density fluctuations for subsonic impinging jets at different radial positions (→: r/D = 0.3, 0.8, 1.4 and 3.5). — —: $p'_{\mathrm{RMS}}/\overline{p}$ (#5), ——: $p'_{\mathrm{RMS}}/\overline{p}$ (#6), — —: $\rho'_{\mathrm{RMS}}/\overline{\rho}$ (#5), ——: $\rho'_{\mathrm{RMS}}/\overline{\rho}$ (#6)

are given in table 6.1, the scatterplots are shown in figure 6.10. $R_{\rho,T}$ is strongly negative for all observation points. Far away from the stagnation point ($r/D = 3.5$), the coefficient reaches a value of -0.94 and justifies the approximations. The correlation between density and pressure is not zero, as proposed. On the contrary, the coefficient is strongly positive (≈ 0.7) close to the axis, but decreases with increasing r/D. Far away from the stagnation point, the approximation $R_{\rho,p} \approx 0$ is valid. Similarly, pressure fluctuations are not unimportant compared to density fluctuations in the entire region where the flow is influenced by the impingement. Farther downstream $\rho_{\mathrm{RMS}}/\overline{\rho}$ is approximately three times as large as $p_{\mathrm{RMS}}/\overline{p}$ for $y^+ \gtrsim 5$, as it can be seen in figure 6.9.

Lechner et al. (2001) assumed a linear relation between thermodynamic fluctuations. Following the entropy definition $s = c_v \ln\left(p/\rho^{\kappa}\right)$, the linearised gas law and the neglect of pressure fluctuations with respect to density fluctuations, the approximation reads:

$$\frac{s'}{c_v} \approx -\kappa \frac{\rho'}{\overline{\rho}} \approx \kappa \frac{T'}{\overline{T}} \; . \tag{6.12}$$

Figure 6.10 shows scatter plots of (s', ρ'), (s', T') and (s', p'). Approximation 6.12 is included in the plots (black solid line) and can be confirmed for all radial positions.

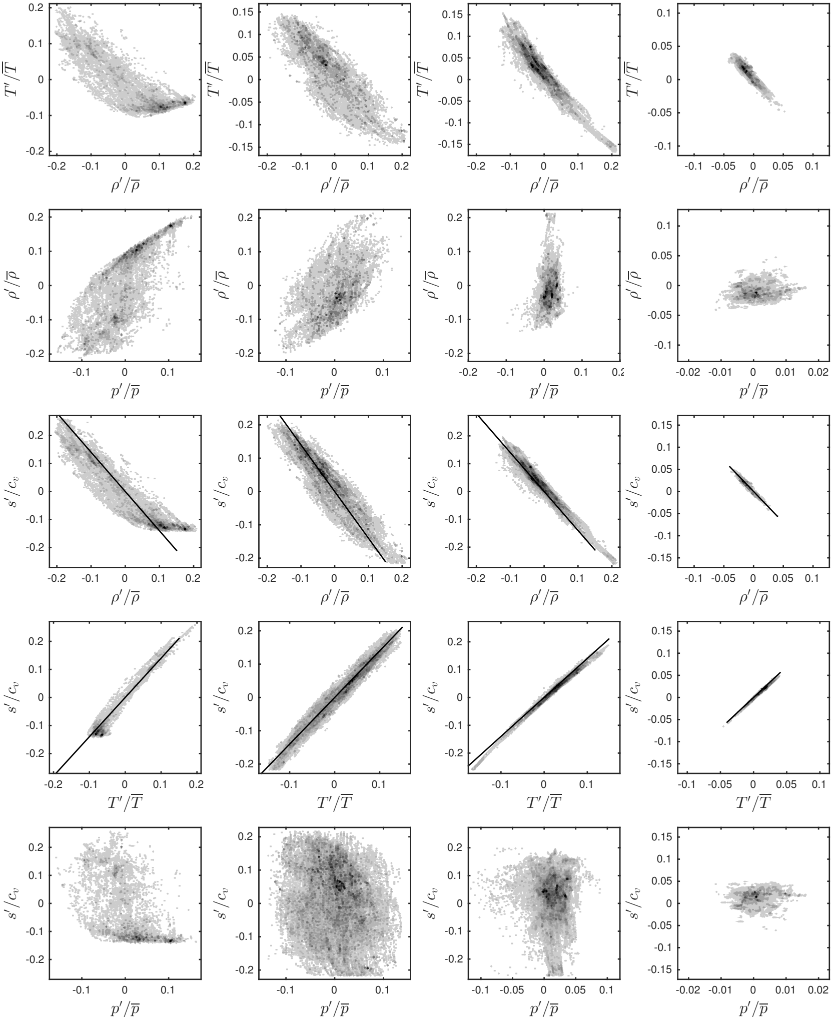

Figure 6.10: Scatter plots at $13 \leq y^+ \leq 17$ for different radial positions (→: $r/D = 0.3$, 0.8, 1.4 and 3.5, simulation #6. Approximation 6.12 is included in row 3 and 4 (black solid line).

		r/D			
R	y^+	0.3 ± 0.05	0.8 ± 0.05	1.4 ± 0.05	3.5 ± 0.05
$R_{v'u'_r}$	15 ± 2	-0.04	0.01	0.04	0.08
$R_{v'T'}$	15 ± 2	-0.08	0.05	0.18	0.24
$R_{T'\rho'}$	15 ± 2	-0.75	-0.80	-0.86	-0.94
$R_{\rho'p'}$	15 ± 2	0.70	0.58	0.41	0.14
$R_{v'u'_r}$	40 ± 2	-0.11	-0.11	0.19	0.18
$R_{v'T'}$	40 ± 2	-0.02	0.11	-0.11	-0.24
$R_{T'\rho'}$	40 ± 2	-0.79	-0.76	-0.75	-0.94
$R_{\rho'p'}$	40 ± 2	0.69	0.40	0.48	0.04

Table 6.1: Correlation coefficients for simulation #6.

6.3 Reynolds stresses

Modern high performance computers allow three-dimensional direct numerical simulations of impinging jets with relevant Reynolds numbers since recently. However, the computations are limited to academic cases for the foreseeable future. For the improvement of turbulence models, which are widely used for industrial applications, our DNS provide a database for validation. An important term that rises among others in the Reynolds-averaged Navier-Stokes equations (RANS) is the Reynolds stress tensor $\overline{\rho u_i'' u_j''}$, at which we look in this section. Since the mean circumferential velocity component is zero, the terms $\overline{\rho u_\theta'' v''}$ and $\overline{\rho u_\theta'' u_r''}$ are not of relevance and therefore not shown. Figure 6.11 shows the four main entries of the tensor. We analyse the flow close to the wall and at the radial distance where the shoulder of the Nusselt number is present. The profiles are taken normal to the wall at $r/D = 1.4$ (left column) and parallel to the wall at $y^+ = 15$ (middle column) and $y^+ = 40$ (right column).

At $r/D = 1.4$, the $\theta\theta$-component (first row, left) increases until $y^+ \approx 10$ and then stays almost constant within the boundary layer.

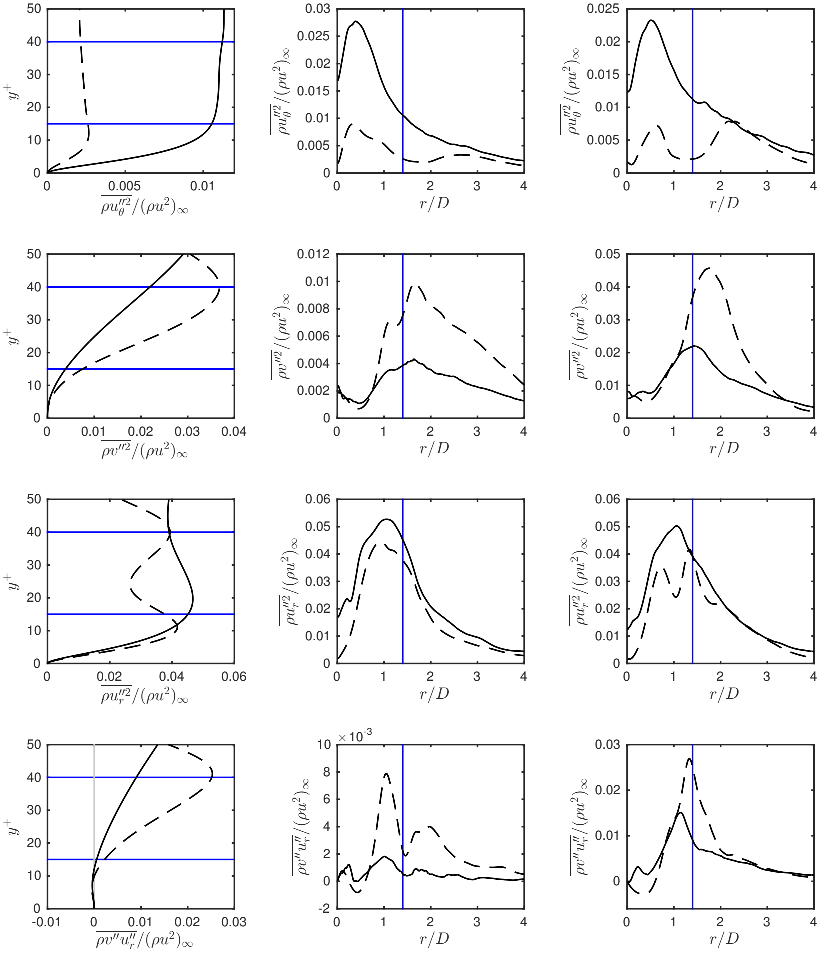

Figure 6.11: Influence of the Reynolds number (#5: 3300, #6: 8000) on the main Reynolds stress tensor components, ↓: $\overline{\rho u_\theta''^2}$, $\overline{\rho v''^2}$, $\overline{\rho u_r''^2}$ and $\overline{\rho v'' u_r''}$. Left: $r/D = 1.4$, middle: $y^+ = 15$, right: $y^+ = 40$. — —: #5, ——: #6, ——: locations $r/D = 1.4$, $y^+ = 15$ and $y^+ = 40$.

The maximum stress occurs around a half-diameter from the jet axis. At low Reynolds number (3300) a second maximum is present around $r/D = 2 - 2.5$. Another difference between the two simulations is that the stress component is higher in the case of the higher Reynolds number (8000). Additional to this area another area of high stress is present farther away from the wall and the jet axis and will be discussed later.

The yy-component is stronger in the case of the low Reynolds number. The strength of this entry of the tensor increases with the distance to the wall, until it decreases again when approaching the upper end of the wall jet. Since the wall jet's centre and upper end are at higher y^+-values in the case of the higher Reynolds number, the maximum of $\overline{\rho v''^2}$ occurs also at a higher dimensionless wall distance. The highest stress occurs at a radial distance of around $1.5 - 1.8$ diameters.

The distribution of the rr-component features two maxima in the wall-normal direction, whereby this characteristic is distinct stronger in the case of the lower Reynolds number. The gap between the two maxima increases with the distance from the jet axis. This shape is directly caused by primary and secondary vortices that move parallel to the wall and increase their diameter. In figure 6.12, the area of the highest $\overline{\rho u_r''^2}$-value is indicated by two dash-dotted lines. Those lines coincide with the path of the primary vortex rings that have their origin in the shear layer of the free jet and the counter-rotating secondary vortices that emerge due to wall friction. The maximal fluctuations occur at $r/D \approx 1$ where the two vortices have the highest radial velocity.

The yr-component has a similar wall-normal distribution as the yy-component. However, the radial location of the highest value is closer to the jet axis at $r/D \approx 1 - 1.3$. The simulation with the lower Reynolds number features higher values of $\overline{\rho v'' u_r''}$ and a stronger distinct maximum.

Figure 6.12 summarises the locations of high stresses. The impingement of primary ring vortices causes strong stress in the $\theta\theta$-direction. The movement of the pair consisting of a primary and a secondary vortex causes

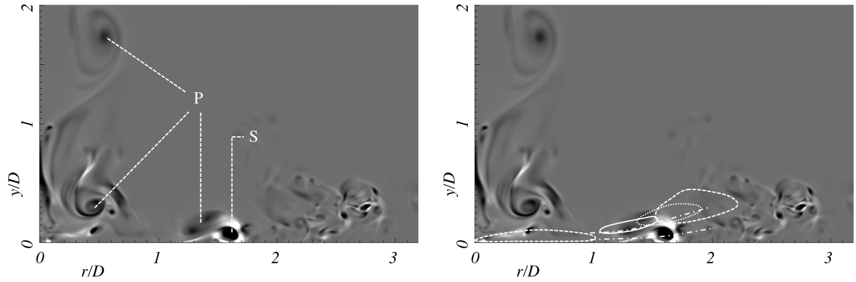

Figure 6.12: Instantaneous flow field of simulation #3: QD^2/v_∞^2 in the range -85 (white) to 85 (black). Left: location of primary (P) and secondary (S) vortices. Right: locations of high Reynolds stress tensor components - - - - -: $\theta\theta$, ·········: yy, -·-·-: rr, ——: yr

strong stress in the rr-direction. The components yr, yy and again $\theta\theta$ are strongly influenced by the movement of the primary vortex and become important in this order with increasing radial distance.

6.4 Reynolds stress budgets

Performing DNS, we are able to compute the terms in the balance equations for the Reynolds stress tensor components according to section 3.1 and appendix A.1.3.1. The budgets are presented for one radial position $r/D = 1.4$ and at one constant dimensionless wall distance $y^+ = 15$.

The budget of $\overline{\rho u_\theta''^2}$ in figure 6.13 shows significant differences between the two different Reynolds numbers. At $r/D = 1.4$, the two dominant terms in the boundary layer, but not at the wall are turbulent diffusion and pressure strain in simulation #5 ($Re = 3300$). Both are of equal strength and opposite sign. At the higher Reynolds number, the turbulent diffusion is of less importance. As counterpart to the pressure strain, also production and turbulent dissipation contribute to the loss of stress. At the wall, stress is produced by viscous diffusion and lost by turbulent dissipation in both

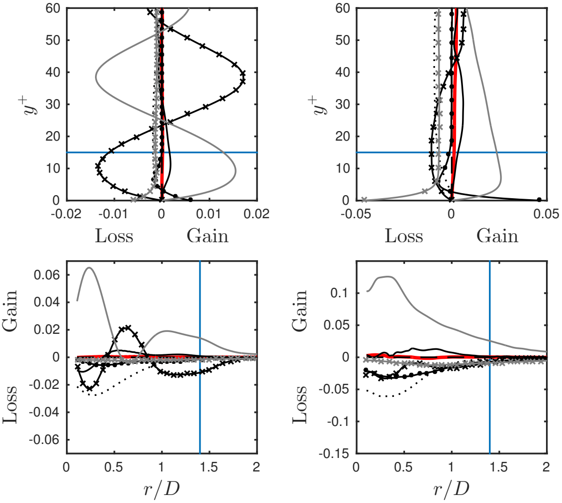

Figure 6.13: Budget of the $\theta\theta$-component $\overline{\rho u_\theta''^2}$. Left column: #5 ($Re = 3300$), right colomn: #6 ($Re = 8000$), first row: $r/D = 1.4$, second row: $y^+ = 15$. ━━: IB, ——: C, ...: PR, -×-×-×-: TD, -●-●-●-: VD, — —: M, ——: PS, -×-×-×-: DS, ——: locations $r/D = 1.4$, $y^+ = 15$.

cases. At $y^+ = 15$, stress is mainly produced by pressure strain and lost by convection (both cases). At $Re = 3300$, turbulent diffusion contributes positively at $r/D \approx 0.6$ and negatively at other radial distances. In contrary, the turbulent diffusion is negative for $Re = 8000$ for all radial distances.

The budget of $\overline{\rho v''^2}$ in figure 6.14 is dominated by turbulent diffusion and pressure strain in both cases and all locations. Except for $y^+ \gtrsim 35$ at $Re = 3300$, TD contributes positively and PS negatively. At this higher dimensionless wall distances, also convection and production become more important and contribute with loss respectively gain. In the radial direction, the two opponents feature maxima at $r/D \approx 0.25$ and $r/D \approx 0.8$.

The rr-component of the Reynolds stress tensor has, compared to the

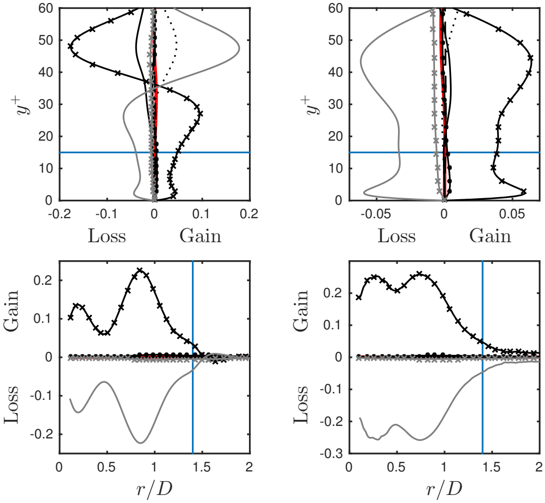

Figure 6.14: Budget of $\overline{\rho v''^2}$. Legend: see figure 6.13.

other components, much more significant terms in its budget. Figure 6.15 shows that the dominant terms at the wall are viscous diffusion (gain) and turbulent dissipation (loss). Farther away from the wall ($y^+ = 15$) pressure strain gains most stress. Its maximum is around $r/D \approx 0.8$. At this location, the stress is likewise decreased by turbulent diffusion.

The budget of $\overline{\rho v'' u_r''}$ in figure 6.16 contains two main terms: pressure strain and turbulent diffusion. The first one gains stress at and nearby the wall and then turns negative at higher dimensionless wall distances. In the boundary layer, the turbulent diffusion behaves opposite. At higher values of y^+, around 35, also production becomes more important in the case of $Re = 3300$. The radial distance of $r/D = 1.4$ is located in a local extremum of the two main terms. Another, stronger extremum with opposite signs occurs at $r/D \approx 0.8$.

The Reynolds stress budgets of simulations #1-4 are not discussed, but they are given in appendix A.3.3 for the sake of completeness.

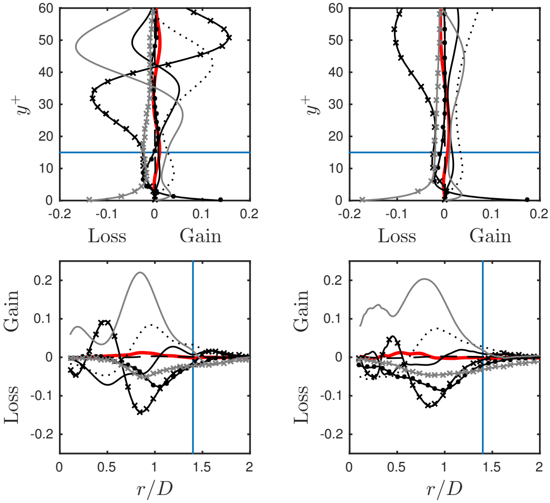

Figure 6.15: Budget of $\overline{\rho u_r''^2}$. Legend: see figure 6.13.

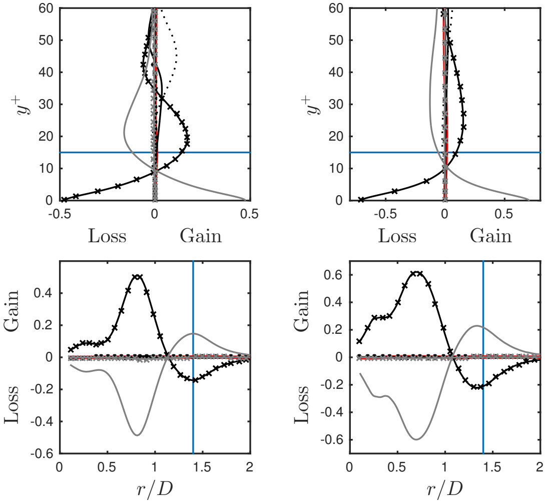

Figure 6.16: Budget of $\overline{\rho v'' u_r''}$. Legend: see figure 6.13.

7 Conclusion and Outlook

Within this dissertation, different direct numerical simulations of impinging jets have been carried out. They differ in Mach and Reynolds number as well as the temperature difference between the ambient fluid and the total inlet temperature. All simulations have a nozzle-to-plate distance of five diameters in common. Concerning the modes of the impinging jet, it was found that:

- The impinging jet features a toroidal dominant mode that is not affected by the Reynolds number in the range $3300 \leq Re \leq 8000$. The dimensionless frequency of that mode decreases with increasing Mach number.

- In the subsonic case, this mode represents the primary and secondary ring vortices that develop in the shear layer of the free respectively wall jet.

- In the supersonic case, this mode represents either again the vortex rings ($Re = 3300$) or the formation of a head vortex due to leapfrogging ($Re = 8000$). The choice of the ambient temperature has an influence of the mode. In case of a hot environment, the impinging jet switches between two modes of the same frequency. Both are toroidal, but one is more strictly axisymmetrical then the other one. Standoff shocks periodically appear and disappear within this cycle. They move between the impinging plate and the shock cell system.

The supersonic configurations fall within the pre-silence zone, since the nozzle pressure ratio is relatively low ($NPR = 2.15$). With regard to impinging tones, the following conclusions can be drawn:

- The existence of a feedback loop can be confirmed. Furthermore, it could be shown that the interaction between vortices and standoff shocks produce the sound waves via two different mechanisms.
- Type 1: shock-vortex-interaction. A vortex crashes asymmetrical into a standoff shock and yanks it out of its stable position. The shock accelerates and transforms into a sound wave that is radiated. This mechanism can analogously be found in free jets and is responsible for screech. The difference however is that not the shock diamonds, but the standoff shock is involved.
- Type 2: shock-vortex-shock-interaction. The interaction between a vortex and two standoff shocks leads to the creation of a subsonic embedding within a supersonic flow. The collapse of this embedding creates a strong spherical pressure wave.

For future work, it is worthwhile to have a closer look on the shock-vortex-shock-interaction. Within this thesis, the origin of the tone could be clarified. However, the question why the collapse of the subsonic embedding leads to the production of such a powerful pressure wave remains open.

The here considered simulations allow the movement of a standoff shock between the impinging plate and the shock cell system. The increase of the NPR at constant h/D leads to an increase of the shock cell spacing of the free jet. At some point the standoff shock will not “have space” to move. Based on the investigations found in the literature and the own results of this thesis, it is possible that the change of the nature of the standoff shock can be a reason for the existence of the zone of silence. In future work, this hypothesis should be checked with DNS of higher NPR

respectively lower h/D. Additional effects due to an oblique position or curvature of the impinging plate are worth to be investigated as well.

The investigation of heat transfer and related quantities lead to the following conclusions:

- The passing of a pair consisting of a primary and a secondary vortex ring parallel to the wall causes a temporal local heat transfer enhancement. This can be observed in the Nusselt number profile and quantified by the wall-normal turbulent heat flux. The latter transports hot fluid away from the wall at a radial distance from the stagnation point of $1 \lesssim r/D \lesssim 2$. This phenomenon is stronger distinct at lower Reynolds numbers.

- The calculation of the dominant mode, which coincides with the above described vortex rings, together with the experimental results of Janetzke (2010) suggest that the enhancement of that mode is the key to an increase in heat transfer efficiency. This is in contrary to Janetzke own statement saying that shear layer instabilities are meaningless for the choice of the pulsation. In this thesis, it could be shown that the excitation with the eigenfrequency leads to the development of one vortex ring per cycle that is much stronger than in the unforced case.

- Reynolds analogies were tested for the subsonic compressible cases. The Nusselt number approximations according to the Reynolds and the Chilton Colburn analogies deliver useful values if the distance to the jet axis is larger than one diameter. In the stagnation point region, both relations deliver big errors and cannot be recommended.

- The generalized Reynolds analogy (GRA) was applied and compared to the Crocco-Busemann relation. Both approximations relate the mean temperature field to the mean velocity field with inaccurate results. Only the GRA can predict the temperature field with good precision, in the area where the radial acceleration is zero

($r/D = 0.8$). Since the wall jet exhibits in most of the domain different flow conditions that do not meet the assumed quasi-one-dimensional flow (canonical compressible wall-bounded turbulent flows), the relation cannot be applied reliably to the impinging jet.

- The relation between the fluctuating temperature and velocity according to the GRA is not applicable at all. The reason for this lies in the change of sign of the term $\overline{(\rho v)' u'}$, which creates singularities in the predicted temperature fluctuations.

- The linear relation between thermodynamic fluctuations of entropy, density and temperature as suggested by Lechner et al. (2001) can be confirmed for the entire wall jet.

- The main components of the Reynolds stress tensor could be conciliated with the primary and secondary vortex rings of the wall jet. The budget terms are given in order to allow the improvement of RANS and LES models.

In further investigations, the effect of the pulsation on the time-averaged heat transfer should be analysed. Within this thesis, it was found out that the increased vortex rings due to pulsation entrain much more surrounding fluid and lead to a decrease of the temperature difference used for the definition of the Nusselt number. Either a redefinition of Nu needs to be applied or the configuration should be adapted so that the ambient temperature is equal to the total inlet temperature and only the plate is heated. The pulsation with a too low frequency, compared to the eigenfrequency, leads to the development of multiple vortex rings per cycle (Janetzke (2010)). In addition, the opening and closing of a valve is far away from a harmonic excitation. It is an important aspect to investigate the influence of the excitation function on the development of the vortex rings. The investigation of the influence of cross flow and curvature are as well important for technical applications. Given so many vital aspects that still need to be researched, it is hoped that this study will stimulate further investigations in this field.

A Appendix

A.1 Methods for flow analysis

A.1.1 Calculation rules for averages

$$\overline{\alpha'} = 0 \tag{A.1a}$$

$$\overline{\alpha'} = \overline{\alpha - \overline{\alpha}} = \overline{\alpha} - \overline{\alpha} = 0 \tag{A.1b}$$

$$\overline{\alpha''} \text{ gen. } \neq 0 \tag{A.2a}$$

$$\overline{\alpha''} = \overline{\alpha - \widetilde{\alpha}} = \overline{\alpha} - \widetilde{\alpha} = \overline{\alpha} - \frac{\overline{\rho\alpha}}{\overline{\rho}} \text{ gen. } \neq 0 \tag{A.2b}$$

$$\overline{\rho\alpha''} = 0 \tag{A.3a}$$

$$\begin{aligned} \alpha'' &= \alpha - \widetilde{a} \\ \overline{\rho\alpha''} &= \overline{\rho\left(\alpha - \widetilde{\alpha}\right)} \\ &= \overline{\rho\alpha} - \overline{\rho\,\widetilde{\alpha}} \\ &= \overline{\rho\alpha} - \overline{\rho\,\underbrace{\frac{\overline{\rho\alpha}}{\overline{\rho}}}_{=\,\text{const.}}} \\ &= \overline{\rho\alpha} - \overline{\rho}\frac{\overline{\rho\alpha}}{\overline{\rho}} = 0 \end{aligned} \tag{A.3b}$$

$$\overline{\alpha\beta} = \overline{\alpha}\,\overline{\beta} + \overline{\alpha'\beta'} \tag{A.4a}$$

$$\begin{aligned} \overline{\alpha\beta} &= \overline{\left(\overline{\alpha} + \alpha'\right)\left(\overline{\beta} + \beta'\right)} = \overline{\overline{\alpha}\,\overline{\beta}} + \overline{\overline{\alpha}\beta'} + \overline{\alpha'\,\overline{\beta}} + \overline{\alpha'\beta'} \\ &= \overline{\alpha}\,\overline{\beta} + \overline{\alpha}\,\cancelto{0}{\overline{\beta'}} + \cancelto{0}{\overline{\alpha'}}\,\overline{\beta} + \overline{\alpha'\beta'} = \overline{\alpha}\,\overline{\beta} + \overline{\alpha'\beta'} \end{aligned} \tag{A.4b}$$

$$\overline{\rho\alpha\beta} = \overline{\rho}\,\widetilde{\alpha}\,\widetilde{\beta} + \overline{\rho\alpha''\beta''} \tag{A.5a}$$

$$\overline{\rho\alpha\beta} = \overline{\rho\left(\widetilde{\alpha} + \alpha''\right)\left(\widetilde{\beta} + \beta''\right)} = \overline{\rho}\,\widetilde{\alpha}\,\widetilde{\beta} + \overline{\rho\alpha''\beta''} + \widetilde{\alpha}\,\cancelto{0}{\overline{\rho\beta''}} + \widetilde{\beta}\,\cancelto{0}{\overline{\rho\alpha''}} \tag{A.5b}$$

$$\overline{\alpha''} = \overline{\alpha} - \widetilde{\alpha} \tag{A.6a}$$

$$\begin{aligned} \alpha'' &= \alpha - \widetilde{\alpha} \\ \overline{\alpha''} &= \overline{\alpha - \widetilde{\alpha}} = \overline{\alpha} - \widetilde{\alpha} \end{aligned} \tag{A.6b}$$

$$\frac{\partial}{\partial t}\left(\rho\alpha\beta\right) = \beta\frac{\partial}{\partial t}\left(\rho\alpha\right) + \alpha\frac{\partial}{\partial t}\left(\rho\beta\right) - \alpha\beta\frac{\partial}{\partial t}\left(\rho\right) \tag{A.7a}$$

$$\begin{aligned} \frac{\partial}{\partial t}\left(\rho\alpha\beta\right) &= \beta\frac{\partial}{\partial t}\left(\rho\alpha\right) + \rho\alpha\frac{\partial}{\partial t}\left(\beta\right) \\ \alpha\frac{\partial}{\partial t}\left(\rho\beta\right) &= \rho\alpha\frac{\partial}{\partial t}\left(\beta\right) + \alpha\beta\frac{\partial}{\partial t}\left(\rho\right) \end{aligned} \tag{A.7b}$$

A.1.2 Cylindrical coordinates

A.1.2.1 Partial derivatives

$$\begin{aligned}\frac{\partial \alpha}{\partial \theta} &= -r \sin(\theta) \frac{\partial \alpha}{\partial x} + r \cos(\theta) \frac{\partial \alpha}{\partial z} \\ \frac{\partial \alpha}{\partial r} &= \cos(\theta) \frac{\partial \alpha}{\partial x} + \sin(\theta) \frac{\partial \alpha}{\partial z}\end{aligned} \tag{A.8}$$

A.1.2.2 Gradient

$$\operatorname{grad} \alpha = \left\{ \frac{1}{r} \frac{\partial \alpha}{\partial \theta}, \frac{\partial \alpha}{\partial y}, \frac{\partial \alpha}{\partial r} \right\} \tag{A.9}$$

$$\begin{aligned}\left(\operatorname{grad} \underline{\underline{\alpha}}\right)_{\theta\theta} &= \frac{1}{r} \frac{\partial \alpha_\theta}{\partial \theta} + \frac{\alpha_r}{r} \\ \left(\operatorname{grad} \underline{\underline{\alpha}}\right)_{y\theta} &= \frac{1}{r} \frac{\partial \alpha_y}{\partial \theta} \\ \left(\operatorname{grad} \underline{\underline{\alpha}}\right)_{r\theta} &= \frac{1}{r} \frac{\partial \alpha_r}{\partial \theta} - \frac{\alpha_\theta}{r}\end{aligned} \tag{A.10}$$

The other six components comply with the respective ones of the Cartesian coordinates.

A.1.2.3 Divergence

In this section, the divergence of tensors of order one and two are taken from Schade & Neemann (2006). The divergence of tensors of third order are derived, following the description of Schade & Neemann (2006).

$$\operatorname{div} \underline{a} = \frac{\partial a_r}{\partial r} + \frac{1}{r} \frac{\partial a_\theta}{\partial \theta} + \frac{1}{r} a_r + \frac{\partial a_y}{\partial y} \tag{A.11}$$

$$
\begin{aligned}
\left(\operatorname{div}\underline{\underline{a}}\right)_r &= \frac{\partial a_{rr}}{\partial r} + \frac{1}{r}\frac{\partial a_{r\theta}}{\partial \theta} + \frac{\partial a_{ry}}{\partial y} + \frac{a_{rr} - a_{\theta\theta}}{r} \\
\left(\operatorname{div}\underline{\underline{a}}\right)_\theta &= \frac{\partial a_{\theta r}}{\partial r} + \frac{1}{r}\frac{\partial a_{\theta\theta}}{\partial \theta} + \frac{\partial a_{\theta y}}{\partial y} + \frac{a_{r\theta} + a_{\theta r}}{r} \\
\left(\operatorname{div}\underline{\underline{a}}\right)_y &= \frac{\partial a_{yr}}{\partial r} + \frac{1}{r}\frac{\partial a_{y\theta}}{\partial \theta} + \frac{\partial a_{yy}}{\partial y} + \frac{a_{yr}}{r}
\end{aligned}
\tag{A.12}
$$

$$
\begin{aligned}
\left(\operatorname{div}\underline{\underline{\underline{a}}}\right)_{rr} &= \frac{\partial a_{rrr}}{\partial r} + \frac{1}{r}\frac{\partial a_{rr\theta}}{\partial \theta} + \frac{\partial a_{rry}}{\partial y} + \frac{a_{rrr} - a_{\theta r\theta} - a_{r\theta\theta}}{r} \\
\left(\operatorname{div}\underline{\underline{\underline{a}}}\right)_{r\theta} &= \frac{\partial a_{r\theta r}}{\partial r} + \frac{1}{r}\frac{\partial a_{r\theta\theta}}{\partial \theta} + \frac{\partial a_{r\theta y}}{\partial y} + \frac{a_{rr\theta} + a_{r\theta r} - a_{\theta\theta\theta}}{r} \\
\left(\operatorname{div}\underline{\underline{\underline{a}}}\right)_{ry} &= \frac{\partial a_{ryr}}{\partial r} + \frac{1}{r}\frac{\partial a_{ry\theta}}{\partial \theta} + \frac{\partial a_{ryy}}{\partial y} + \frac{a_{ryr} - a_{\theta y\theta}}{r} \\
\left(\operatorname{div}\underline{\underline{\underline{a}}}\right)_{\theta r} &= \frac{\partial a_{\theta rr}}{\partial r} + \frac{1}{r}\frac{\partial a_{\theta r\theta}}{\partial \theta} + \frac{\partial a_{\theta ry}}{\partial y} + \frac{a_{rr\theta} + a_{\theta rr} - a_{\theta\theta\theta}}{r} \\
\left(\operatorname{div}\underline{\underline{\underline{a}}}\right)_{\theta\theta} &= \frac{\partial a_{\theta\theta r}}{\partial r} + \frac{1}{r}\frac{\partial a_{\theta\theta\theta}}{\partial \theta} + \frac{\partial a_{\theta\theta y}}{\partial y} + \frac{a_{r\theta\theta} + a_{\theta r\theta} + a_{\theta\theta r}}{r} \\
\left(\operatorname{div}\underline{\underline{\underline{a}}}\right)_{\theta y} &= \frac{\partial a_{\theta yr}}{\partial r} + \frac{1}{r}\frac{\partial a_{\theta y\theta}}{\partial \theta} + \frac{\partial a_{\theta yy}}{\partial y} + \frac{a_{\theta yr} + a_{ry\theta}}{r} \\
\left(\operatorname{div}\underline{\underline{\underline{a}}}\right)_{yr} &= \frac{\partial a_{yrr}}{\partial r} + \frac{1}{r}\frac{\partial a_{yr\theta}}{\partial \theta} + \frac{\partial a_{yry}}{\partial y} + \frac{a_{yrr} - a_{y\theta\theta}}{r} \\
\left(\operatorname{div}\underline{\underline{\underline{a}}}\right)_{y\theta} &= \frac{\partial a_{y\theta r}}{\partial r} + \frac{1}{r}\frac{\partial a_{y\theta\theta}}{\partial \theta} + \frac{\partial a_{y\theta y}}{\partial y} + \frac{a_{yr\theta} + a_{y\theta r}}{r} \\
\left(\operatorname{div}\underline{\underline{\underline{a}}}\right)_{yy} &= \frac{\partial a_{yyr}}{\partial r} + \frac{1}{r}\frac{\partial a_{yy\theta}}{\partial \theta} + \frac{\partial a_{yyy}}{\partial y} + \frac{a_{yyr}}{r}
\end{aligned}
\tag{A.13}
$$

A.1.3 Transport equations in cylindrical coordinates

All terms involving a derivative in circumferential direction are omitted, since they are zero due to the circumferential average.

A.1.3.1 Reynolds stresses

Convection

$$
\begin{aligned}
C_{\theta\theta} = &- \left[\frac{1}{r}\frac{\partial}{\partial\theta}\left(\widetilde{u_\theta}\,\overline{\rho}\,\widetilde{u''_\theta u''_\theta}\right) + \frac{\partial}{\partial y}\left(\widetilde{v}\,\overline{\rho}\,\widetilde{u''_\theta u''_\theta}\right) + \frac{\partial}{\partial r}\left(\widetilde{u_r}\,\overline{\rho}\,\widetilde{u''_\theta u''_\theta}\right) \right. \\
&\left. + \frac{\overline{\rho}}{r}\left(2\,\widetilde{u''_r u''_\theta}\,\widetilde{u_\theta} + \widetilde{u''_\theta u''_\theta}\,\widetilde{u_r}\right) \right] \\
C_{\theta y} = &- \left[\frac{1}{r}\frac{\partial}{\partial\theta}\left(\widetilde{u_\theta}\,\overline{\rho}\,\widetilde{u''_\theta v''}\right) + \frac{\partial}{\partial y}\left(\widetilde{v}\,\overline{\rho}\,\widetilde{u''_\theta v''}\right) + \frac{\partial}{\partial r}\left(\widetilde{u_r}\,\overline{\rho}\,\widetilde{u''_\theta v''}\right) \right. \\
&\left. + \frac{\overline{\rho}}{r}\left(\widetilde{u''_\theta v''}\,\widetilde{u_r} + \widetilde{u''_r v''}\,\widetilde{u_\theta}\right) \right] \\
C_{\theta r} = &- \left[\frac{1}{r}\frac{\partial}{\partial\theta}\left(\widetilde{u_\theta}\,\overline{\rho}\,\widetilde{u''_\theta u''_r}\right) + \frac{\partial}{\partial y}\left(\widetilde{v}\,\overline{\rho}\,\widetilde{u''_\theta u''_r}\right) + \frac{\partial}{\partial r}\left(\widetilde{u_r}\,\overline{\rho}\,\widetilde{u''_\theta u''_r}\right) \right. \\
&\left. + \frac{\overline{\rho}}{r}\left(\widetilde{u''_r u''_r}\,\widetilde{u_\theta} + \widetilde{u''_\theta u''_r}\,\widetilde{u_r} - \widetilde{u''_\theta u''_\theta}\,\widetilde{u_\theta}\right) \right] \\
C_{yy} = &- \left[\frac{1}{r}\frac{\partial}{\partial\theta}\left(\widetilde{u_\theta}\,\overline{\rho}\,\widetilde{v''v''}\right) + \frac{\partial}{\partial y}\left(\widetilde{v}\,\overline{\rho}\,\widetilde{v''v''}\right) + \frac{\partial}{\partial r}\left(\widetilde{u_r}\,\overline{\rho}\,\widetilde{v''v''}\right) + \frac{\overline{\rho}}{r}\,\widetilde{v''v''}\,\widetilde{u_r} \right] \\
C_{yr} = &- \left[\frac{1}{r}\frac{\partial}{\partial\theta}\left(\widetilde{u_\theta}\,\overline{\rho}\,\widetilde{v''u''_r}\right) + \frac{\partial}{\partial y}\left(\widetilde{v}\,\overline{\rho}\,\widetilde{v''u''_r}\right) + \frac{\partial}{\partial r}\left(\widetilde{u_r}\,\overline{\rho}\,\widetilde{v''u''_r}\right) \right. \\
&\left. + \frac{\overline{\rho}}{r}\left(\widetilde{v''u''_r}\,\widetilde{u_r} - \widetilde{v''u''_\theta}\,\widetilde{u_\theta}\right) \right] \\
C_{rr} = &- \left[\frac{1}{r}\frac{\partial}{\partial\theta}\left(\widetilde{u_\theta}\,\overline{\rho}\,\widetilde{u''_r u''_r}\right) + \frac{\partial}{\partial y}\left(\widetilde{v}\,\overline{\rho}\,\widetilde{u''_r u''_r}\right) + \frac{\partial}{\partial r}\left(\widetilde{u_r}\,\overline{\rho}\,\widetilde{u''_r u''_r}\right) \right. \\
&\left. + \frac{\overline{\rho}}{r}\left(\widetilde{u''_r u''_r}\,\widetilde{u_r} - 2\,\widetilde{u''_\theta u''_r}\,\widetilde{u_\theta}\right) \right] \qquad \text{(A.14)}
\end{aligned}
$$

Production

$$
\begin{aligned}
PR_{\theta\theta} &= -2\,\overline{\rho}\left[\widetilde{u''_\theta u''_\theta}\left(\frac{1}{r}\frac{\partial\,\widetilde{u_\theta}}{\partial\theta}+\frac{\widetilde{u_r}}{r}\right)+\widetilde{u''_\theta v''}\frac{\partial\,\widetilde{u_\theta}}{\partial y}+\widetilde{u''_\theta u''_r}\frac{\partial\,\widetilde{u_\theta}}{\partial r}\right] \\
PR_{\theta y} &= -\,\overline{\rho}\left[\widetilde{u''_\theta u''_\theta}\frac{1}{r}\frac{\partial\,\widetilde{v}}{\partial\theta}+\widetilde{u''_\theta v''}\frac{\partial\,\widetilde{v}}{\partial y}+\widetilde{u''_\theta u''_r}\frac{\partial\,\widetilde{v}}{\partial r}+\widetilde{v'' u_{\theta''}}\left(\frac{1}{r}\frac{\partial\,\widetilde{u_\theta}}{\partial\theta}+\frac{\widetilde{u_r}}{r}\right)\right. \\
&\qquad \left.+\,\widetilde{v''v''}\frac{\partial\,\widetilde{u_\theta}}{\partial y}+\widetilde{v''u''_r}\frac{\partial\,\widetilde{u_\theta}}{\partial r}\right] \\
PR_{\theta r} &= -\,\overline{\rho}\left[\widetilde{u''_\theta u''_\theta}\left(\frac{1}{r}\frac{\partial\,\widetilde{u_r}}{\partial\theta}-\frac{\widetilde{u_\theta}}{r}\right)+\widetilde{u''_\theta v''}\frac{\partial\,\widetilde{u_r}}{\partial y}+\widetilde{u''_\theta u''_r}\frac{\partial\,\widetilde{u_r}}{\partial r}\right. \\
&\qquad \left.+\,\widetilde{u''_r u''_\theta}\left(\frac{1}{r}\frac{\partial\,\widetilde{u_\theta}}{\partial\theta}+\frac{\widetilde{u_r}}{r}\right)+\widetilde{u''_r v''}\frac{\partial\,\widetilde{u_\theta}}{\partial y}+\widetilde{u''_r u''_r}\frac{\partial\,\widetilde{u_\theta}}{\partial r}\right] \\
PR_{yy} &= -2\,\overline{\rho}\left[\widetilde{v''u''_\theta}\frac{1}{r}\frac{\partial\,\widetilde{v}}{\partial\theta}+\widetilde{v''v''}\frac{\partial\,\widetilde{v}}{\partial y}+\widetilde{v''u''_r}\frac{\partial\,\widetilde{v}}{\partial r}\right] \\
PR_{yr} &= -\,\overline{\rho}\left[\widetilde{v''u''_\theta}\left(\frac{1}{r}\frac{\partial\,\widetilde{u_r}}{\partial\theta}-\frac{\widetilde{u_\theta}}{r}\right)+\widetilde{v''v''}\frac{\partial\,\widetilde{u_r}}{\partial y}+\widetilde{v''u''_r}\frac{\partial\,\widetilde{u_r}}{\partial r}+\widetilde{u''_r u''_\theta}\frac{1}{r}\frac{\partial\,\widetilde{v}}{\partial\theta}\right. \\
&\qquad \left.+\,\widetilde{u''_r v''}\frac{\partial\,\widetilde{v}}{\partial y}+\widetilde{u''_r u''_\theta}\frac{\partial\,\widetilde{v}}{\partial r}\right] \\
PR_{rr} &= -2\,\overline{\rho}\left[\widetilde{u''_r u''_\theta}\left(\frac{1}{r}\frac{\partial\,\widetilde{u_r}}{\partial\theta}-\frac{\widetilde{u_\theta}}{r}\right)+\widetilde{u''_r v''}\frac{\partial\,\widetilde{u_r}}{\partial y}+\widetilde{u''_r u''_r}\frac{\partial\,\widetilde{u_r}}{\partial r}\right] \qquad \text{(A.15)}
\end{aligned}
$$

Turbulent Diffusion

$$
\begin{aligned}
TD_{\theta\theta} &= \frac{\partial\,\overline{\rho u''_\theta u''_\theta u''_r}}{\partial r}+\frac{1}{r}\frac{\partial\,\overline{\rho u''_\theta u''_\theta u''_\theta}}{\partial\theta}+\frac{\partial\,\overline{\rho u''_\theta u''_\theta v''}}{\partial y}+3\,\frac{\overline{\rho u''_r u''_\theta u''_\theta}}{r} \\
&\qquad +2\left(\frac{1}{r}\frac{\partial\,\overline{p'u'_\theta}}{\partial\theta}+\frac{\overline{p'u'_r}}{r}\right) \\
TD_{\theta y} &= \frac{\partial\,\overline{\rho u''_\theta v'' u''_r}}{\partial r}+\frac{1}{r}\frac{\partial\,\overline{\rho u''_\theta v'' u''_\theta}}{\partial\theta}+\frac{\partial\,\overline{\rho u''_\theta v'' v''}}{\partial y}+\frac{2\,\overline{\rho u''_\theta v'' u''_r}}{r}+\frac{1}{r}\frac{\partial\,\overline{p'v'}}{\partial\theta}
\end{aligned}
$$

$$+\frac{\partial\,\overline{p'u'_\theta}}{\partial y}$$

$$TD_{\theta r}=\frac{\partial\,\overline{\rho u''_\theta u''_r u''_r}}{\partial r}+\frac{1}{r}\frac{\partial\,\overline{\rho u''_\theta u''_r u''_\theta}}{\partial\theta}+\frac{\partial\,\overline{\rho u''_\theta u''_r v''}}{\partial y}+\frac{2\,\overline{\rho u''_\theta u''_r u''_r}-\overline{\rho u''_\theta u''_\theta u''_\theta}}{r}$$

$$+\frac{1}{r}\frac{\partial\,\overline{p'u'_r}}{\partial\theta}-\frac{\overline{p'u'_\theta}}{r}+\frac{\partial\,\overline{p'u'_\theta}}{\partial r}$$

$$TD_{yy}=\frac{\partial\,\overline{\rho v''v''u''_r}}{\partial r}+\frac{1}{r}\frac{\partial\,\overline{\rho v''v''u''_\theta}}{\partial\theta}+\frac{\partial\,\overline{\rho v''v''v''}}{\partial y}+\frac{\overline{\rho v''v''u''_r}}{r}+2\frac{\partial\,\overline{p'v'}}{\partial y}$$

$$TD_{yr}=\frac{\partial\,\overline{\rho v''u''_r u''_r}}{\partial r}+\frac{1}{r}\frac{\partial\,\overline{\rho v''u''_r u''_\theta}}{\partial\theta}+\frac{\partial\,\overline{\rho v''u''_r v''}}{\partial y}+\frac{\overline{\rho v''u''_r u''_r}-\overline{\rho v''u''_\theta u''_\theta}}{r}$$

$$+\frac{\partial\,\overline{p'v'}}{\partial r}+\frac{\partial\,\overline{p'u'_r}}{\partial y}$$

$$TD_{rr}=\frac{\partial\,\overline{\rho u''_r u''_r u''_r}}{\partial r}+\frac{1}{r}\frac{\partial\,\overline{\rho u''_r u''_r u''_\theta}}{\partial\theta}+\frac{\partial\,\overline{\rho u''_r u''_r v''}}{\partial y}+\frac{\overline{\rho u''_r u''_r u''_r}-2\,\overline{\rho u''_r u''_\theta u''_\theta}}{r}$$

$$+2\frac{\partial\,\overline{p'u'_r}}{\partial r}\tag{A.16}$$

Viscous Diffusion

$$VD_{\theta\theta}=2\left(\frac{\partial\,\overline{u'_\theta\tau'_{\theta r}}}{\partial r}+\frac{1}{r}\frac{\partial\,\overline{u'_\theta\tau'_{\theta\theta}}}{\partial\theta}+\frac{\partial\,\overline{u'_\theta\tau'_{\theta y}}}{\partial y}+\frac{\overline{u'_r\tau'_{\theta\theta}}+2\,\overline{u'_\theta\tau'_{r\theta}}}{r}\right)$$

$$VD_{\theta y}=\frac{\partial\,\overline{u'_\theta\tau'_{yr}}}{\partial r}+\frac{1}{r}\frac{\partial\,\overline{u'_\theta\tau'_{y\theta}}}{\partial\theta}+\frac{\partial\,\overline{u'_\theta\tau'_{yy}}}{\partial y}+\frac{\overline{u'_\theta\tau'_{yr}}+\overline{u'_r\tau'_{y\theta}}}{r}+\frac{\partial\,\overline{v'\tau'_{\theta r}}}{\partial r}$$

$$+\frac{1}{r}\frac{\partial\,\overline{v'\tau'_{\theta\theta}}}{\partial\theta}+\frac{\partial\,\overline{v'\tau'_{\theta y}}}{\partial y}+\frac{2\,\overline{v'\tau'_{r\theta}}}{r}$$

$$VD_{\theta r}=\frac{\partial\,\overline{u'_\theta\tau'_{rr}}}{\partial r}+\frac{1}{r}\frac{\partial\,\overline{u'_\theta\tau'_{r\theta}}}{\partial\theta}+\frac{\partial\,\overline{u'_\theta\tau'_{ry}}}{\partial y}+\frac{3\,\overline{u'_r\tau'_{r\theta}}+\overline{u'_\theta\tau'_{rr}}-2\,\overline{u'_\theta\tau'_{\theta\theta}}}{r}$$

$$+\frac{\partial\,\overline{u'_r\tau'_{\theta r}}}{\partial r}+\frac{1}{r}\frac{\partial\,\overline{u'_r\tau'_{\theta\theta}}}{\partial\theta}+\frac{\partial\,\overline{u'_r\tau'_{\theta y}}}{\partial y}$$

$$\begin{aligned}
VD_{yy} &= 2\left(\frac{\partial\,\overline{v'\tau'_{yr}}}{\partial r} + \frac{1}{r}\frac{\partial\,\overline{v'\tau'_{y\theta}}}{\partial\theta} + \frac{\partial\,\overline{v'\tau'_{yy}}}{\partial y} + \frac{\overline{v'\tau'_{yr}}}{r}\right)\\
VD_{yr} &= \frac{\partial\,\overline{v'\tau'_{rr}}}{\partial r} + \frac{1}{r}\frac{\partial\,\overline{v'\tau'_{r\theta}}}{\partial\theta} + \frac{\partial\,\overline{v'\tau'_{ry}}}{\partial y} + \frac{\overline{v'\tau'_{rr}} - \overline{v'\tau'_{\theta\theta}}}{r} + \frac{\partial\,\overline{u'_r\tau'_{yr}}}{\partial r}\\
&\quad + \frac{1}{r}\frac{\partial\,\overline{u'_r\tau'_{y\theta}}}{\partial\theta} + \frac{\partial\,\overline{u'_r\tau'_{yy}}}{\partial y} + \frac{\overline{u'_r\tau'_{yr}} - \overline{u'_\theta\tau'_{y\theta}}}{r}\\
VD_{rr} &= 2\left(\frac{\partial\,\overline{u'_r\tau'_{rr}}}{\partial r} + \frac{1}{r}\frac{\partial\,\overline{u'_r\tau'_{r\theta}}}{\partial\theta} + \frac{\partial\,\overline{u'_r\tau'_{ry}}}{\partial y} + \frac{\overline{u'_r\tau'_{rr}} - \overline{u'_\theta\tau'_{r\theta}} - \overline{u'_r\tau'_{\theta\theta}}}{r}\right)
\end{aligned} \tag{A.17}$$

Mass-Flux Variation

$$\begin{aligned}
M_{\theta\theta} &= 2\,\overline{u''_\theta}\left(\frac{\partial\,\overline{\tau_{\theta r}}}{\partial r} + \frac{1}{r}\frac{\partial\,\overline{\tau_{\theta\theta}}}{\partial\theta} + \frac{\partial\,\overline{\tau_{\theta y}}}{\partial y} + \frac{\overline{\tau_{r\theta}} + \overline{\tau_{\theta r}}}{r} - \frac{1}{r}\frac{\partial\,\overline{p}}{\partial\theta}\right)\\
M_{\theta y} &= \ \overline{u''_\theta}\left(\frac{\partial\,\overline{\tau_{yr}}}{\partial r} + \frac{1}{r}\frac{\partial\,\overline{\tau_{y\theta}}}{\partial\theta} + \frac{\partial\,\overline{\tau_{yy}}}{\partial y} + \frac{\overline{\tau_{yr}}}{r} - \frac{\partial\,\overline{p}}{\partial y}\right)\\
&\quad + \overline{v''}\left(\frac{\partial\,\overline{\tau_{\theta r}}}{\partial r} + \frac{1}{r}\frac{\partial\,\overline{\tau_{\theta\theta}}}{\partial\theta} + \frac{\partial\,\overline{\tau_{\theta y}}}{\partial y} + \frac{\overline{\tau_{r\theta}} + \overline{\tau_{\theta r}}}{r} - \frac{1}{r}\frac{\partial\,\overline{p}}{\partial\theta}\right)\\
M_{\theta r} &= \ \overline{u''_\theta}\left(\frac{\partial\,\overline{\tau_{rr}}}{\partial r} + \frac{1}{r}\frac{\partial\,\overline{\tau_{r\theta}}}{\partial\theta} + \frac{\partial\,\overline{\tau_{ry}}}{\partial y} + \frac{\overline{\tau_{rr}} - \overline{\tau_{\theta\theta}}}{r} - \frac{\partial\,\overline{p}}{\partial r}\right)\\
&\quad + \overline{u''_r}\left(\frac{\partial\,\overline{\tau_{\theta r}}}{\partial r} + \frac{1}{r}\frac{\partial\,\overline{\tau_{\theta\theta}}}{\partial\theta} + \frac{\partial\,\overline{\tau_{\theta y}}}{\partial y} + \frac{\overline{\tau_{r\theta}} + \overline{\tau_{\theta r}}}{r} - \frac{1}{r}\frac{\partial\,\overline{p}}{\partial\theta}\right)\\
M_{yy} &= 2\,\overline{v''}\left(\frac{\partial\,\overline{\tau_{yr}}}{\partial r} + \frac{1}{r}\frac{\partial\,\overline{\tau_{y\theta}}}{\partial\theta} + \frac{\partial\,\overline{\tau_{yy}}}{\partial y} + \frac{\overline{\tau_{yr}}}{r} - \frac{\partial\,\overline{p}}{\partial y}\right)\\
M_{yr} &= \ \overline{v''}\left(\frac{\partial\,\overline{\tau_{rr}}}{\partial r} + \frac{1}{r}\frac{\partial\,\overline{\tau_{r\theta}}}{\partial\theta} + \frac{\partial\,\overline{\tau_{ry}}}{\partial y} + \frac{\overline{\tau_{rr}} - \overline{\tau_{\theta\theta}}}{r} - \frac{\partial\,\overline{p}}{\partial r}\right)\\
&\quad + \overline{u''_r}\left(\frac{\partial\,\overline{\tau_{yr}}}{\partial r} + \frac{1}{r}\frac{\partial\,\overline{\tau_{y\theta}}}{\partial\theta} + \frac{\partial\,\overline{\tau_{yy}}}{\partial y} + \frac{\overline{\tau_{yr}}}{r} - \frac{\partial\,\overline{p}}{\partial y}\right)\\
M_{rr} &= 2\,\overline{u''_r}\left(\frac{\partial\,\overline{\tau_{rr}}}{\partial r} + \frac{1}{r}\frac{\partial\,\overline{\tau_{r\theta}}}{\partial\theta} + \frac{\partial\,\overline{\tau_{ry}}}{\partial y} + \frac{\overline{\tau_{rr}} - \overline{\tau_{\theta\theta}}}{r} - \frac{\partial\,\overline{p}}{\partial r}\right)
\end{aligned} \tag{A.18}$$

Pressure Strain

$$
\begin{aligned}
PS_{\theta\theta} &= \frac{2}{r}\overline{p'\left(\frac{\partial u'_\theta}{\partial \theta} + u'_r\right)} \\
PS_{\theta r} &= \overline{p'\left(\frac{\partial u'_\theta}{\partial r} + \frac{1}{r}\frac{\partial u'_r}{\partial \theta} - \frac{u'_\theta}{r}\right)} \\
PS_{\theta y} &= \overline{p'\left(\frac{\partial u'_\theta}{\partial y} + \frac{1}{r}\frac{\partial v'}{\partial \theta}\right)} \\
PS_{rr} &= 2\,\overline{p'\frac{\partial u'_r}{\partial r}} \\
PS_{ry} &= \overline{p'\left(\frac{\partial u'_r}{\partial y} + \frac{\partial v'}{\partial r}\right)} \\
PS_{yy} &= 2\,\overline{p'\frac{\partial v'}{\partial y}}
\end{aligned}
\tag{A.19}
$$

Turbulent Dissipation

$$
\begin{aligned}
DS_{\theta\theta} &= -2\left[\overline{\tau'_{\theta\theta}\left(\frac{1}{r}\frac{\partial u'_\theta}{\partial \theta} + \frac{u'_r}{r}\right) + \tau'_{\theta y}\frac{\partial u'_\theta}{\partial y} + \tau'_{\theta r}\frac{\partial u'_\theta}{\partial r}}\right] \\
DS_{\theta r} &= -\left[\overline{\tau'_{\theta\theta}\left(\frac{1}{r}\frac{\partial u'_r}{\partial \theta} - \frac{u'_\theta}{r}\right) + \tau'_{\theta y}\frac{\partial u'_r}{\partial y} + \tau'_{\theta r}\frac{\partial u'_r}{\partial r}}\right. \\
&\qquad \left.\overline{+\,\tau'_{r\theta}\left(\frac{1}{r}\frac{\partial u'_\theta}{\partial \theta} + \frac{u'_r}{r}\right) + \tau'_{ry}\frac{\partial u'_\theta}{\partial y} + \tau'_{rr}\frac{\partial u'_\theta}{\partial r}}\right] \\
DS_{\theta y} &= -\left[\overline{\tau'_{\theta\theta}\frac{1}{r}\frac{\partial v'}{\partial \theta} + \tau'_{\theta y}\frac{\partial v'}{\partial y} + \tau'_{\theta r}\frac{\partial v'}{\partial r}}\right. \\
&\qquad \left.\overline{+\,\tau'_{y\theta}\left(\frac{1}{r}\frac{\partial u'_\theta}{\partial \theta} + \frac{u'_r}{r}\right) + \tau'_{yy}\frac{\partial u'_\theta}{\partial y} + \tau'_{yr}\frac{\partial u'_\theta}{\partial r}}\right] \\
DS_{yy} &= -2\left[\overline{\tau'_{y\theta}\frac{1}{r}\frac{\partial v'}{\partial \theta} + \tau'_{yy}\frac{\partial v'}{\partial y} + \tau'_{yr}\frac{\partial v'}{\partial r}}\right]
\end{aligned}
$$

$$DS_{yr} = -\left[\overline{\tau'_{y\theta}\left(\frac{1}{r}\frac{\partial u'_r}{\partial \theta} - \frac{u'_\theta}{r}\right) + \tau'_{yy}\frac{\partial u'_r}{\partial y} + \tau'_{yr}\frac{\partial u'_r}{\partial r}}\right.$$
$$\left.+\overline{\tau'_{r\theta}\frac{1}{r}\frac{\partial v'}{\partial \theta} + \tau'_{ry}\frac{\partial v'}{\partial y} + \tau'_{rr}\frac{\partial v'}{\partial r}}\right]$$
$$DS_{rr} = -2\left[\overline{\tau'_{r\theta}\left(\frac{1}{r}\frac{\partial u'_r}{\partial \theta} - \frac{u'_\theta}{r}\right) + \tau'_{ry}\frac{\partial u'_r}{\partial y} + \tau'_{rr}\frac{\partial u'_r}{\partial r}}\right] \tag{A.20}$$

A.1.3.2 Turbulent heat flux

Since the aggregation of the terms is not unique, the components are given separately in some cases (C, PR, DS).

Convection

$$C_i = -C_i^* - J_i \tag{A.21}$$

$$C_\theta^* = \frac{\widetilde{u_\theta}}{r}\left(\frac{\partial\,\overline{\rho e'' u''_\theta}}{\partial \theta} + \overline{\rho e'' u''_r}\right) + \widetilde{v}\frac{\partial\,\overline{\rho e'' u''_\theta}}{\partial y} + \widetilde{u_r}\frac{\partial\,\overline{\rho e'' u''_\theta}}{\partial r}$$
$$C_y^* = \frac{\widetilde{u_\theta}}{r}\frac{\partial\,\overline{\rho e'' v''}}{\partial \theta} + \widetilde{v}\frac{\partial\,\overline{\rho e'' v''}}{\partial y} + \widetilde{u_r}\frac{\partial\,\overline{\rho e'' v''}}{\partial r}$$
$$C_r^* = \frac{\widetilde{u_\theta}}{r}\left(\frac{\partial\,\overline{\rho e'' u''_r}}{\partial \theta} - \overline{\rho e'' u''_\theta}\right) + \widetilde{v}\frac{\partial\,\overline{\rho e'' u''_r}}{\partial y} + \widetilde{u_r}\frac{\partial\,\overline{\rho e'' u''_r}}{\partial r} \tag{A.22}$$

$$J_\theta = \overline{\rho e'' u''_\theta}\left(\frac{\partial\,\widetilde{u_r}}{\partial r} + \frac{1}{r}\frac{\partial\,\widetilde{u_\theta}}{\partial \theta} + \frac{\partial\,\widetilde{v}}{\partial y} + \frac{\widetilde{u_r}}{r}\right)$$
$$J_y = \overline{\rho e'' v''}\left(\frac{\partial\,\widetilde{u_r}}{\partial r} + \frac{1}{r}\frac{\partial\,\widetilde{u_\theta}}{\partial \theta} + \frac{\partial\,\widetilde{v}}{\partial y} + \frac{\widetilde{u_r}}{r}\right)$$
$$J_r = \overline{\rho e'' u''_r}\left(\frac{\partial\,\widetilde{u_r}}{\partial r} + \frac{1}{r}\frac{\partial\,\widetilde{u_\theta}}{\partial \theta} + \frac{\partial\,\widetilde{v}}{\partial y} + \frac{\widetilde{u_r}}{r}\right) \tag{A.23}$$

Turbulent diffusion

$$
\begin{aligned}
TD_\theta &= -\left[\frac{\partial\,\overline{\rho e'' u_\theta'' u_r''}}{\partial r} + \frac{1}{r}\frac{\partial\,\overline{\rho e'' u_\theta'' u_\theta''}}{\partial \theta} + \frac{\partial\,\overline{\rho e'' u_\theta'' v''}}{\partial y} + 2\frac{\overline{\rho e'' u_r'' u_\theta''}}{r}\right] \\
TD_y &= -\left[\frac{\partial\,\overline{\rho e'' v'' u_r''}}{\partial r} + \frac{1}{r}\frac{\partial\,\overline{\rho e'' v'' u_\theta''}}{\partial \theta} + \frac{\partial\,\overline{\rho e'' v'' v''}}{\partial y} + \frac{\overline{\rho e'' v'' u_r''}}{r}\right] \\
TD_r &= -\left[\frac{\partial\,\overline{\rho e'' u_r'' u_r''}}{\partial r} + \frac{1}{r}\frac{\partial\,\overline{\rho e'' u_r'' u_\theta''}}{\partial \theta} + \frac{\partial\,\overline{\rho e'' u_r'' v''}}{\partial y} + \frac{\overline{\rho e'' u_r'' u_r''} - \overline{\rho e'' u_\theta'' u_\theta''}}{r}\right]
\end{aligned}
\tag{A.24}
$$

Production

$$
PR_i = -PR_{e,i} - PR_{u,i} - E_i + G_i \tag{A.25}
$$

$$
\begin{aligned}
PR_{e,\theta} &= \frac{\overline{\rho u_\theta'' u_\theta''}}{r}\frac{\partial\,\widetilde{e}}{\partial \theta} + \overline{\rho u_\theta'' v''}\frac{\partial\,\widetilde{e}}{\partial y} + \overline{\rho u_\theta'' u_r''}\frac{\partial\,\widetilde{e}}{\partial r} \\
PR_{e,y} &= \frac{\overline{\rho v'' u_\theta''}}{r}\frac{\partial\,\widetilde{e}}{\partial \theta} + \overline{\rho v'' v''}\frac{\partial\,\widetilde{e}}{\partial y} + \overline{\rho v'' u_r''}\frac{\partial\,\widetilde{e}}{\partial r} \\
PR_{e,r} &= \frac{\overline{\rho u_r'' u_\theta''}}{r}\frac{\partial\,\widetilde{e}}{\partial \theta} + \overline{\rho u_r'' v''}\frac{\partial\,\widetilde{e}}{\partial y} + \overline{\rho u_r'' u_r''}\frac{\partial\,\widetilde{e}}{\partial r}
\end{aligned}
\tag{A.26}
$$

$$
\begin{aligned}
PR_{u,\theta} &= \frac{\overline{\rho e'' u_\theta''}}{r}\left(\frac{\partial\,\widetilde{u_\theta}}{\partial \theta} + \widetilde{u_r}\right) + \overline{\rho e'' v''}\frac{\partial\,\widetilde{u_\theta}}{\partial y} + \overline{\rho e'' u_r''}\frac{\partial\,\widetilde{u_\theta}}{\partial r} \\
PR_{u,y} &= \frac{\overline{\rho e'' u_\theta''}}{r}\frac{\partial\,\widetilde{v}}{\partial \theta} + \overline{\rho e'' v''}\frac{\partial\,\widetilde{v}}{\partial y} + \overline{\rho e'' u_r''}\frac{\partial\,\widetilde{v}}{\partial r} \\
PR_{u,r} &= \frac{\overline{\rho e'' u_\theta''}}{r}\left(\frac{\partial\,\widetilde{u_r}}{\partial \theta} - \widetilde{u_\theta}\right) + \overline{\rho e'' v''}\frac{\partial\,\widetilde{u_r}}{\partial y} + \overline{\rho e'' u_r''}\frac{\partial\,\widetilde{u_r}}{\partial r}
\end{aligned}
\tag{A.27}
$$

$$
\begin{aligned}
E_\theta &= \overline{p u''_\theta}\left(\frac{1}{r}\frac{\partial \widetilde{u_\theta}}{\partial \theta} + \frac{\partial \widetilde{u_r}}{\partial r} + \frac{\partial \widetilde{v}}{\partial y} + \frac{\widetilde{u_r}}{r}\right) \\
E_y &= \overline{p v''}\left(\frac{1}{r}\frac{\partial \widetilde{u_\theta}}{\partial \theta} + \frac{\partial \widetilde{u_r}}{\partial r} + \frac{\partial \widetilde{v}}{\partial y} + \frac{\widetilde{u_r}}{r}\right) \\
E_r &= \overline{p u''_r}\left(\frac{1}{r}\frac{\partial \widetilde{u_\theta}}{\partial \theta} + \frac{\partial \widetilde{u_r}}{\partial r} + \frac{\partial \widetilde{v}}{\partial y} + \frac{\widetilde{u_r}}{r}\right) \qquad \text{(A.28)}
\end{aligned}
$$

$$
\begin{aligned}
G_0 = {} & \frac{\tau_{\theta\theta}}{r}\left(\frac{\partial \widetilde{u_\theta}}{\partial \theta} + \widetilde{u_r}\right) + \tau_{\theta y}\frac{\partial \widetilde{u_\theta}}{\partial y} + \tau_{\theta r}\frac{\partial \widetilde{u_\theta}}{\partial r} \\
& + \frac{\tau_{y\theta}}{r}\frac{\partial \widetilde{v}}{\partial \theta} + \tau_{yy}\frac{\partial \widetilde{v}}{\partial y} + \tau_{yr}\frac{\partial \widetilde{v}}{\partial r} \\
& + \frac{\tau_{r\theta}}{r}\left(\frac{\partial \widetilde{u_r}}{\partial \theta} - \widetilde{u_\theta}\right) + \tau_{ry}\frac{\partial \widetilde{u_r}}{\partial y} + \tau_{rr}\frac{\partial \widetilde{u_r}}{\partial r} \\
G_\theta = {} & \overline{u''_\theta G_0} \\
G_y = {} & \overline{v'' G_0} \\
G_r = {} & \overline{u''_r G_0} \qquad \text{(A.29)}
\end{aligned}
$$

Turbulent dissipation

$$
DS_i = -A_i + D_i + H_i \qquad \text{(A.30)}
$$

$$
\begin{aligned}
A_\theta &= \overline{u''_\theta\left(\frac{1}{r}\frac{\partial q_\theta}{\partial \theta} + \frac{q_r}{r} + \frac{\partial q_r}{\partial r} + \frac{\partial q_y}{\partial y}\right)} \\
A_y &= \overline{v''\left(\frac{1}{r}\frac{\partial q_\theta}{\partial \theta} + \frac{q_r}{r} + \frac{\partial q_r}{\partial r} + \frac{\partial q_y}{\partial y}\right)}
\end{aligned}
$$

$$A_r = \overline{u_r''\left(\frac{1}{r}\frac{\partial q_\theta}{\partial \theta} + \frac{q_r}{r} + \frac{\partial q_r}{\partial r} + \frac{\partial q_y}{\partial y}\right)} \tag{A.31}$$

$$\begin{aligned}
D_\theta &= \overline{e''\left(\frac{1}{r}\frac{\partial \tau_{\theta\theta}}{\partial \theta} + \frac{\partial \tau_{\theta r}}{\partial r} + \frac{\partial \tau_{\theta y}}{\partial y} + 2\frac{\tau_{\theta r}}{r}\right)} \\
D_y &= \overline{e''\left(\frac{1}{r}\frac{\partial \tau_{y\theta}}{\partial \theta} + \frac{\partial \tau_{yr}}{\partial r} + \frac{\partial \tau_{yy}}{\partial y} + \frac{\tau_{yr}}{r}\right)} \\
D_r &= \overline{e''\left(\frac{1}{r}\frac{\partial \tau_{r\theta}}{\partial \theta} + \frac{\partial \tau_{rr}}{\partial r} + \frac{\partial \tau_{ry}}{\partial y} + \frac{\tau_{rr} - \tau_{\theta\theta}}{r}\right)}
\end{aligned} \tag{A.32}$$

$$\begin{aligned}
H_0 &= \frac{\tau_{\theta\theta}}{r}\left(\frac{\partial u_\theta''}{\partial \theta} + u_r''\right) + \tau_{\theta y}\frac{\partial u_\theta''}{\partial y} + \tau_{\theta r}\frac{\partial u_\theta''}{\partial r} \\
&+ \frac{\tau_{y\theta}}{r}\frac{\partial v''}{\partial \theta} + \tau_{yy}\frac{\partial v''}{\partial y} + \tau_{yr}\frac{\partial v''}{\partial r} \\
&+ \frac{\tau_{r\theta}}{r}\left(\frac{\partial u_r''}{\partial \theta} - u_\theta''\right) + \tau_{ry}\frac{\partial u_r''}{\partial y} + \tau_{rr}\frac{\partial u_r''}{\partial r} \\
H_\theta &= \overline{u_\theta'' H_0} \\
H_y &= \overline{v'' H_0} \\
H_r &= \overline{u_r'' H_0}
\end{aligned} \tag{A.33}$$

Term containing pressure gradient

$$\begin{aligned}
PG_\theta &= -\frac{1}{r}\,\overline{e''\frac{\partial p}{\partial \theta}} \\
PG_y &= -\,\overline{e''\frac{\partial p}{\partial y}} \\
PG_r &= -\,\overline{e''\frac{\partial p}{\partial r}}
\end{aligned} \tag{A.34}$$

Term containing fluctuating dilatation

$$
\begin{aligned}
FD_\theta &= -\overline{p u_\theta'' \left(\frac{1}{r} \frac{\partial u_\theta''}{\partial \theta} + \frac{\partial u_r''}{\partial r} + \frac{\partial v''}{\partial y} + \frac{u_r''}{r} \right)} \\
FD_y &= -\overline{p v'' \left(\frac{1}{r} \frac{\partial u_\theta''}{\partial \theta} + \frac{\partial u_r''}{\partial r} + \frac{\partial v''}{\partial y} + \frac{u_r''}{r} \right)} \\
FD_r &= -\overline{p u_r'' \left(\frac{1}{r} \frac{\partial u_\theta''}{\partial \theta} + \frac{\partial u_r''}{\partial r} + \frac{\partial v''}{\partial y} + \frac{u_r''}{r} \right)}
\end{aligned}
\tag{A.35}
$$

A.1.4 Convergence

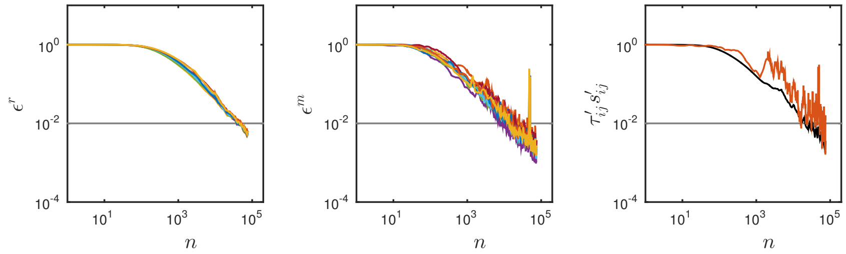

Figure A.1: Convergence of the averaging for simulation #3. ϵ^r and ϵ^m are the RMS and the maximum value of the residuum within the domain, normalised with the respective value of the first time step of the averaging. Left: ϵ^r of Reynolds stress tensor and turbulent heat flux, middle: corresponding ϵ^m, right: ϵ^r (black) and ϵ^m (red) of $\tau'_{ij}s'_{ij}$.

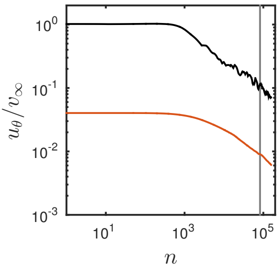

Figure A.2: Convergence of the circumferential velocity u_θ for simulation #5. Black line: maximum within the domain, red line: RMS. The vertical gray line indicates the start of averaging step two.

A.2 Description of the flow

A.2.1 Modes

A.2.1.1 Simulation #4

Figure A.3: Eigenvalue spectrum of simulation #4 computed using a DMD. Red marked points correspond to dominant modes.

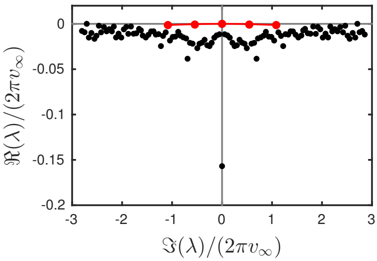

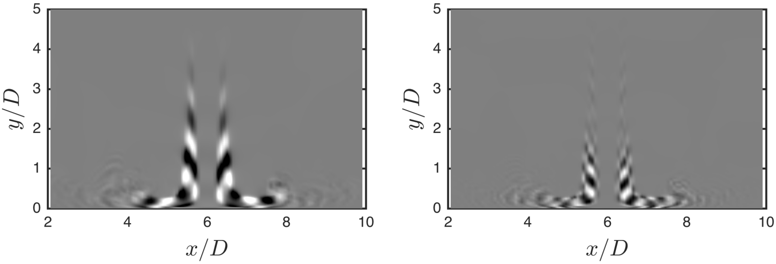

Figure A.4: Temperature field of the dominant dynamic modes (#4) left: $Sr = 0.54$ (±30 K), right: $Sr = 1.08$ (±20 K).

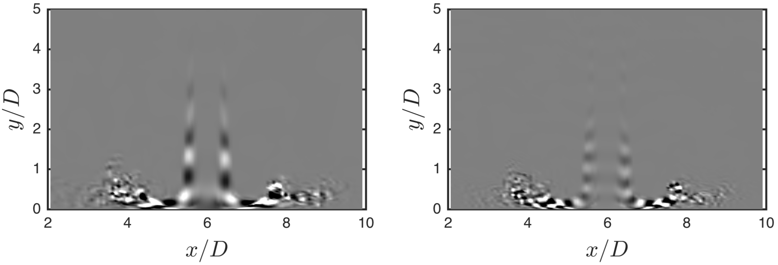

Figure A.5: Q ($\pm 3.1 v_\infty^2 D$) of the dominant dynamic modes (#4) left: $Sr = 0.54$, right: $Sr = 1.08$.

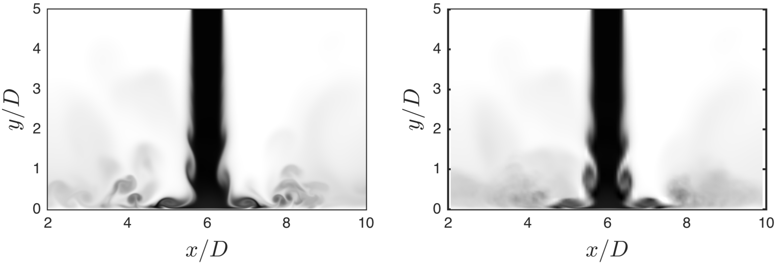

Figure A.6: Confrontation of original flow field (left) and reconstruction using the mean field and the two dominant modes (right), #4.

A.2.1.2 Simulation #5

Two DMD of simulation #5 are confronted within figures A.8 to A.11. The first one uses each grid point of the plane $z/D = 6$ which is resolved with 512×512 points and the second one uses each fourth grid point. Since the area $r/D > 4$ are cut, the resulting resolution is 392×512 respectively 103×128.

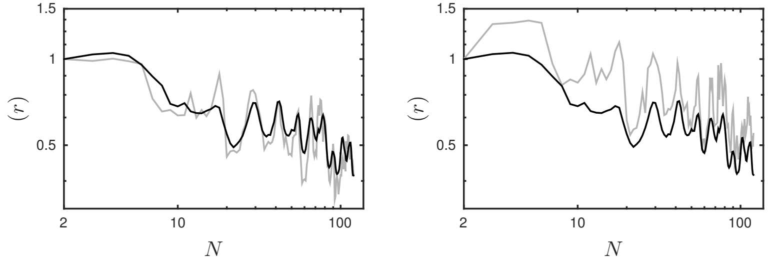

Figure A.7: Convergence of the residual vector r (#5). Black: r_{RMS}, gray: $r_{\max}$ normalised with the values of $N = 2$. Left: 392×512 grid points, right: 103×128.

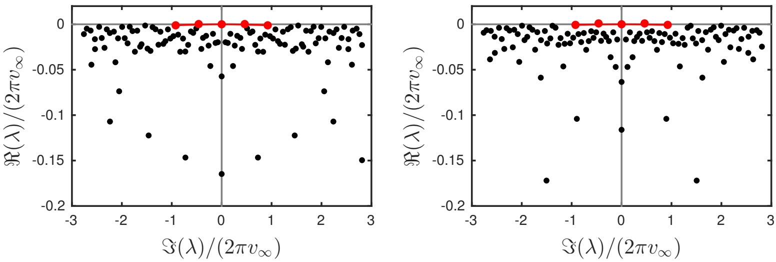

Figure A.8: Eigenvalue spectrum of simulation #5 computed using a DMD. Left: 392×512 grid points, right: 128×103. Red marked points correspond to dominant modes.

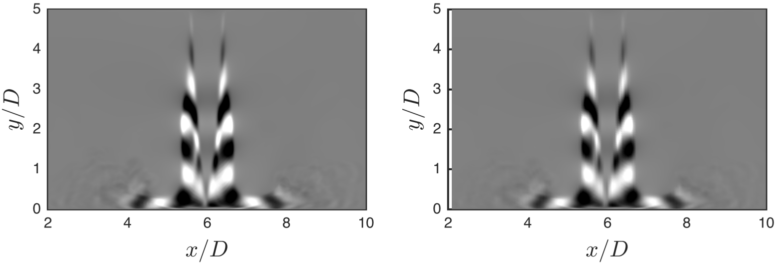

Figure A.9: Temperature field (±30 K) of the dominant dynamic mode $Sr = 0.46$ of simulation #5. Left: 392 × 512 grid points, right: 103 × 128.

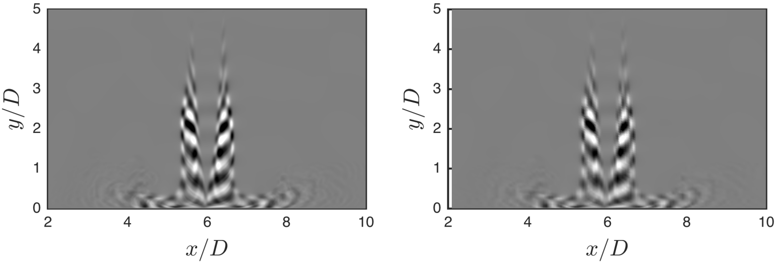

Figure A.10: Temperature field (±20 K) of the dominant dynamic mode $Sr = 0.92$ of simulation #5. Left: 392 × 512 grid points, right: 103 × 128.

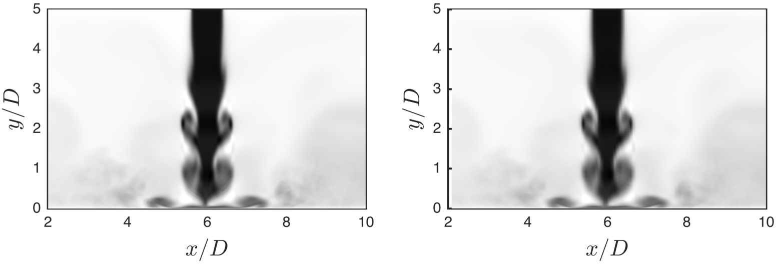

Figure A.11: Reconstruction using the mean field and the two dominant modes. Left: 392 × 512 grid points, right: 103 × 128, #5.

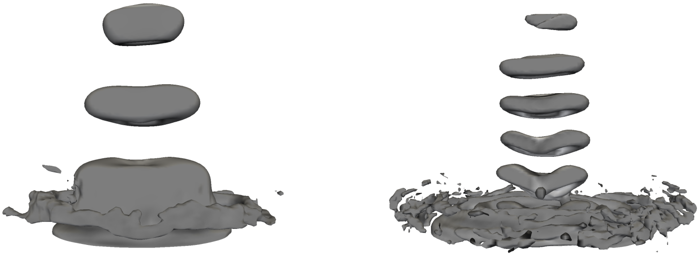

Figure A.12: Pressure contours of the tree-dimensional dominant dynamic modes of simulation #5 performed on 103×128×103 grid points. Left: $Sr = 0.46$ ($\pm 0.01 p_\infty$), right: $Sr = 0.92$ ($\pm 0.005 p_\infty$) coloured with temperature (±50 K respectively ±30 K).

A.2.1.3 Simulation #6

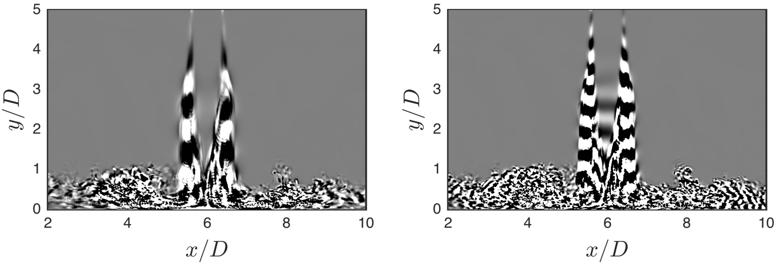

Figure A.13: Q $(\pm 3.1 v_\infty^2 D)$ of the dominant dynamic modes (#6) left: $Sr = 0.46$, right: $Sr = 0.92$.

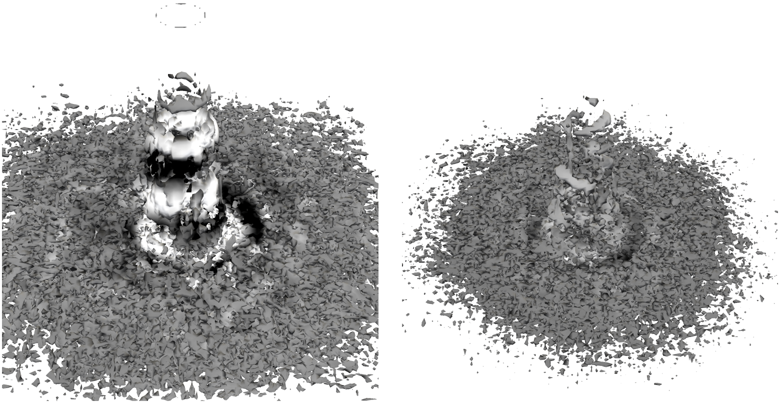

Figure A.14: Q contours $(\pm 3.1 v_\infty^2 D)$ of the tree-dimensional dominant dynamic modes (#6) left: $Sr = 0.46$, right: $Sr = 0.92$ coloured with pressure $(\pm 0.08 p_\infty)$.

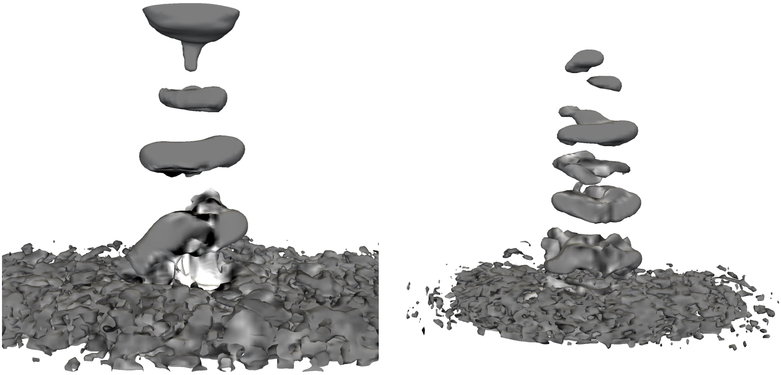

Figure A.15: Pressure contours of the tree-dimensional dominant dynamic modes (#6) left: $Sr = 0.46$ ($\pm 0.01 p_\infty$), right: $Sr = 0.92$ ($\pm 0.005 p_\infty$) coloured with temperature (±50 K respectively ±30 K).

A.2.1.4 Schlieren set-up

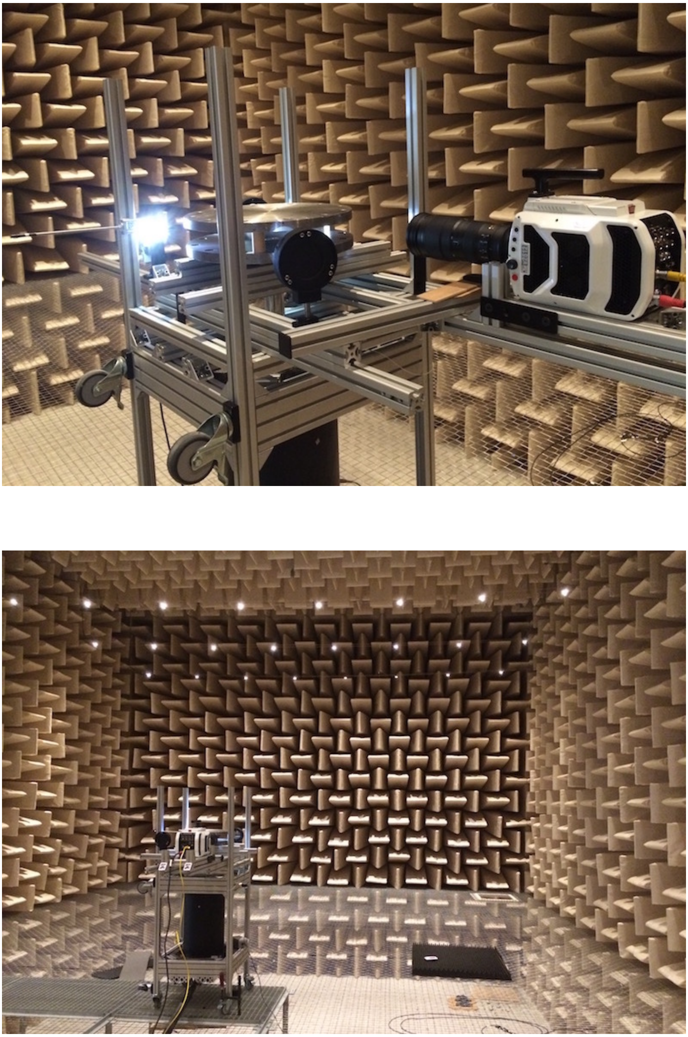

Figure A.16: Experimental set-up for schlieren visualisation within an anechoic room.

A.2.2 Deflection zone and standoff shock

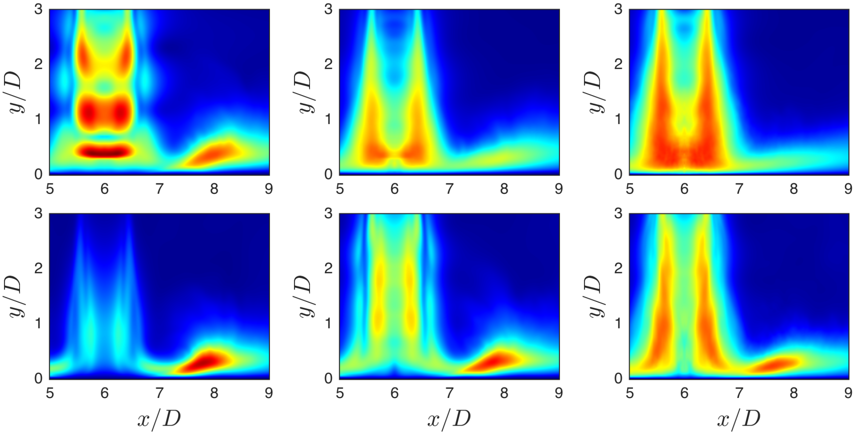

Figure A.17: $v'_{\mathrm{RMS}}/v_\infty$ from 0 (blue) to 0.3 (red). First row, →: simulation #1, #2, #3. Second row, →: simulation #4, #5, #6.

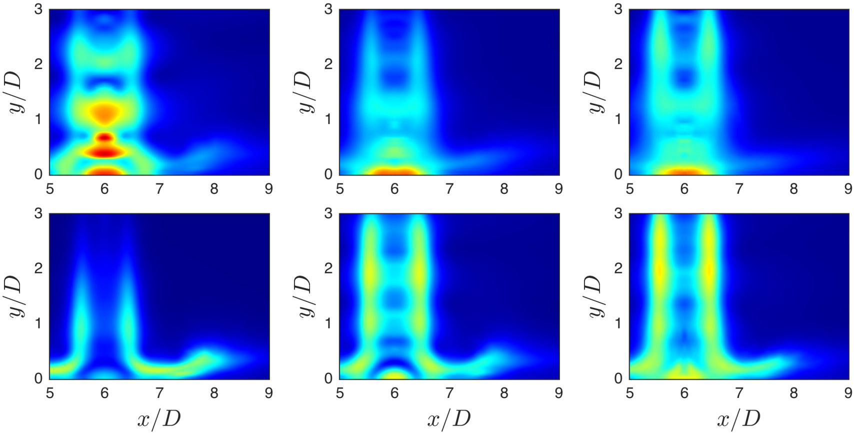

Figure A.18: $p'_{\mathrm{RMS}}/\left(p_{t,in}-p_\infty\right)$ from 0 (blue) to 0.3 (red). First row, →: simulation #1, #2, #3. Second row, →: simulation #4, #5, #6.

A.3 Heat transfer

A.3.1 Turbulent heat flux

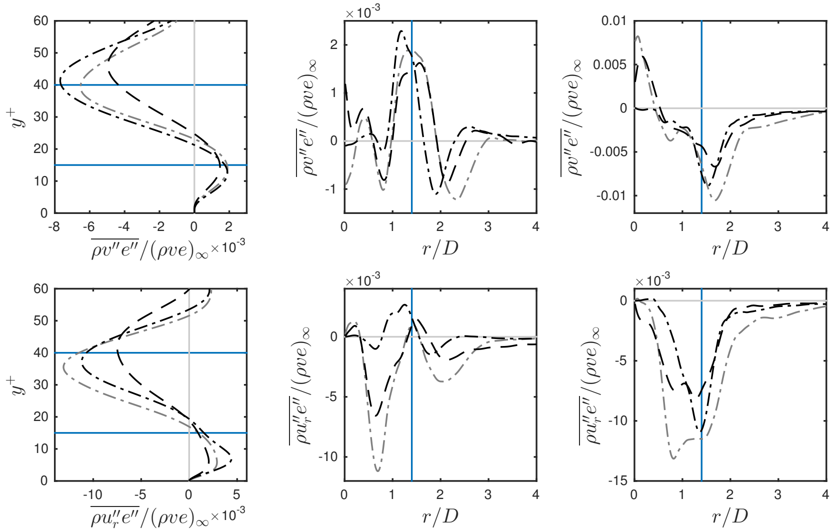

Figure A.19: Influence of the Mach number (#4: 0.41, #5: 0.78, #1: 1.11) on the turbulent heat flux in the wall-normal direction $\overline{\rho v''e''}$ (first row) and radial direction $\overline{\rho u_r''e''}$ (second row). Left: $r/D = 1.4$, middle: $y^+ = 15$, right: $y^+ = 40$. -·-·-: #1, -·-·-: #4, — —: #5, ——: locations $r/D = 1.4$, $y^+ = 15$ and $y^+ = 40$.

A.3.2 Fluctuations

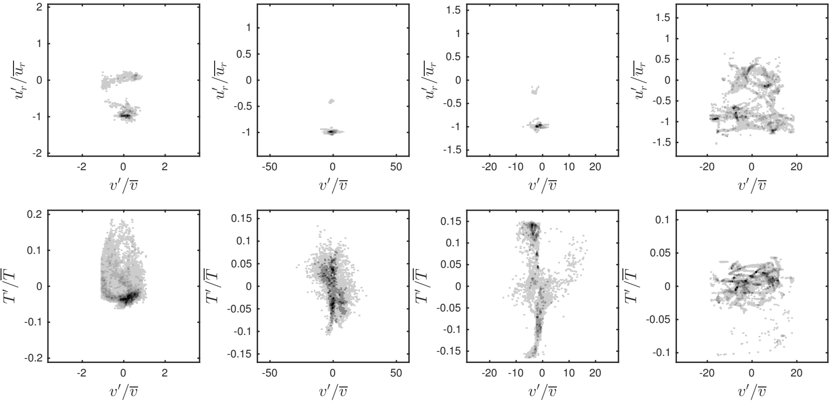

Figure A.20: Scatter plots of radial velocity (first row) and temperature (second row) fluctuation against axial velocity fluctuation at $13 \leq y^+ \leq 17$ for different radial positions (→: $r/D = 0.3$, 0.8, 1.4 and 3.5), simulation #5.

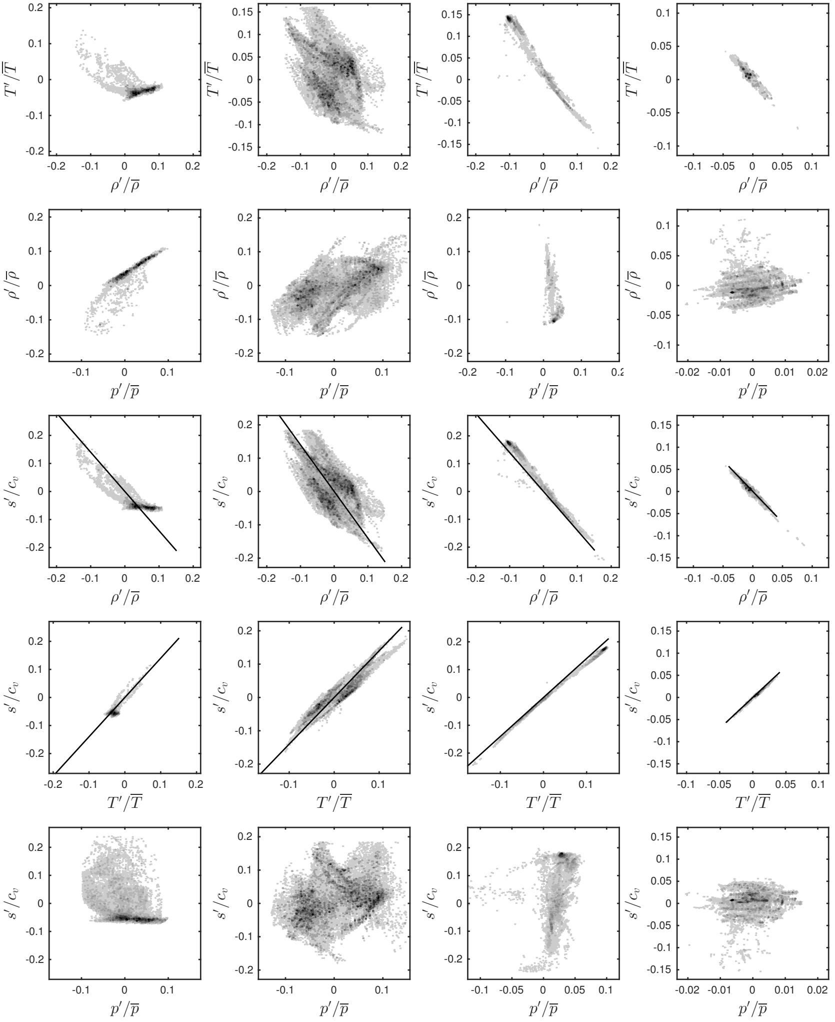

Figure A.21: Scatter plots at $13 \leq y^+ \leq 17$ for different radial positions (→: $r/D = 0.3$, 0.8, 1.4 and 3.5, simulation #5. Approximation 6.12 is included in row 3 and 4 (black solid line).

A.3.3 Reynolds stress budgets

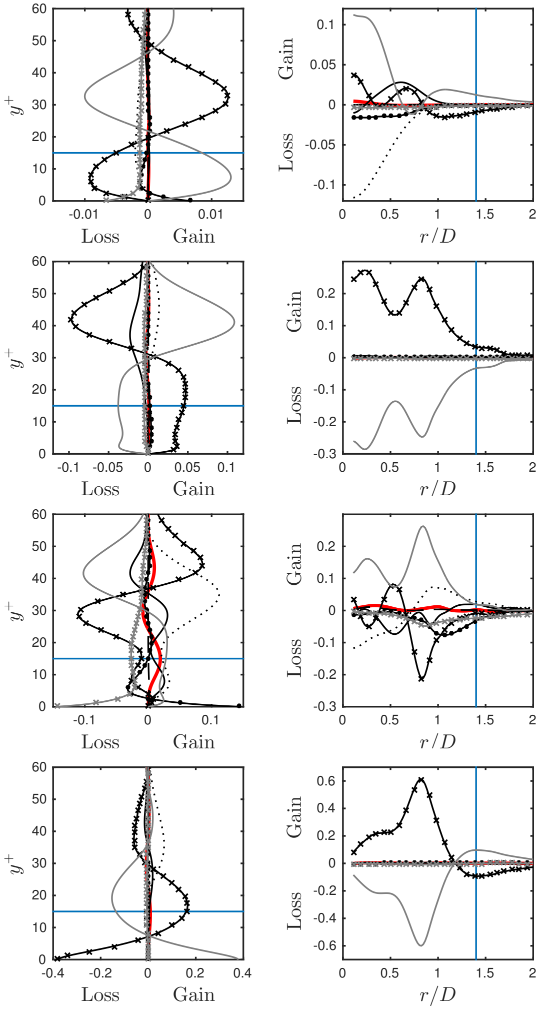

Figure A.22: RST budget of simulation #1. Legend: see figure A.23

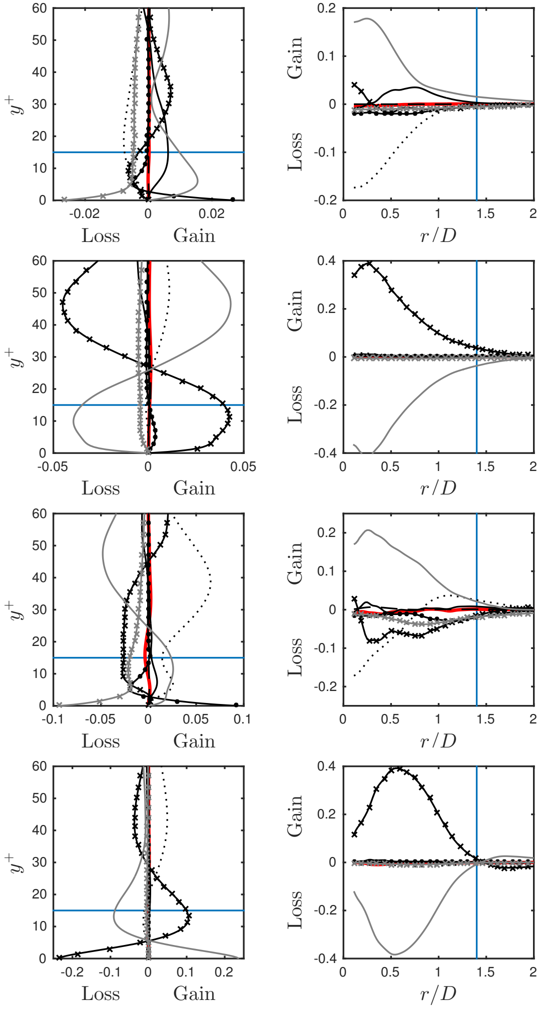

Figure A.23: RST budget of simulation #2. ↓: $\overline{\rho u_\theta''^2}$, $\overline{\rho v''^2}$, $\overline{\rho u_r''^2}$, $\overline{\rho v'' u_r''}$. Left: $r/D = 1.4$, right: $y^+ = 15$. —: IB, —: C, ……: PR, -×-×-: TD, -●-●-: VD, – –: M, —: PS, -×-×-: DS, —: locations $r/D = 1.4$, $y^+ = 15$.

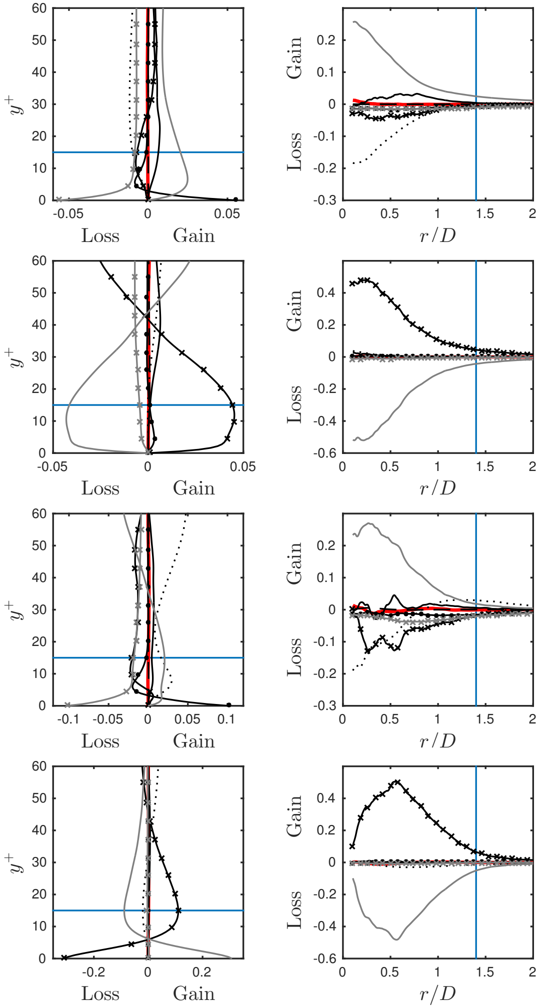

Figure A.24: RST budget of simulation #3. Legend: see figure A.23

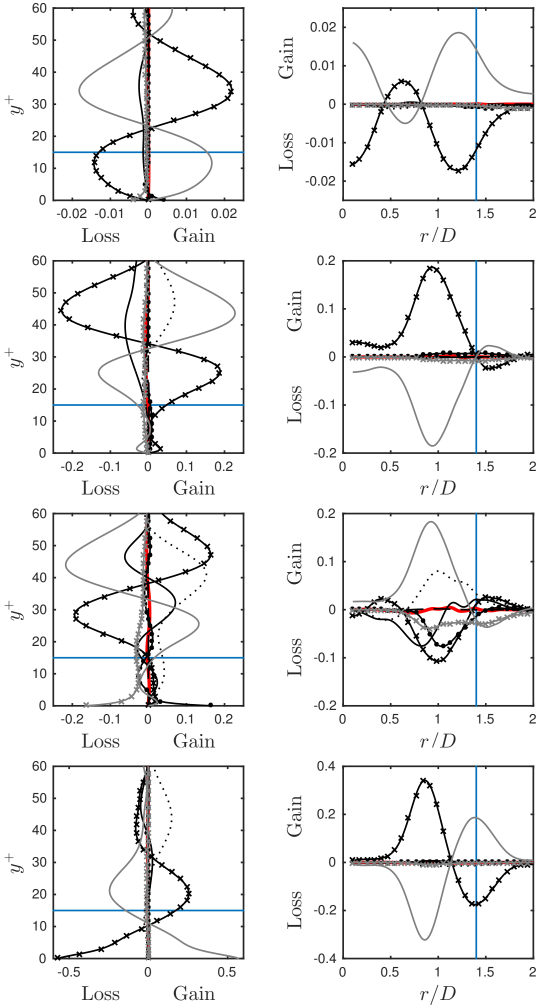

Figure A.25: RST budget of simulation #4. Legend: see figure A.23

References

N. A. Adams and K. Shariff. A High-Resolution Hybrid Compact-ENO Scheme for Shock-Turbulence Interaction Problems. *Journal of Computational Physics*, 127:27–51, 1996.

T. C. Adamson and J. A. Nicholls. On the structure of jets from highly underexpanded nozzles into still air. *Journal of the Aerospace Sciences*, 26 (1):16–24, 1959.

C. Bogey, N. de Cacqueray, and C. Bailly. A shock-capturing methodology based on adaptative spatial filtering for high-order non-linear computations. *Journal of Computational Physics*, 228(5):1447–1465, 2009.

J. Buchlin. Convective heat transfer in impinging-gas-jet arrangements. *Journal of Applied Fluid Mechanics*, 4(3), 2011.

N. Buchmann, D. Mitchell, K. M. Ingvorsen, D. Honnery, and J. Soria. High spatial resolution imaging of a supersonic underexpanded jet impinging on a flat plate. In *6th Australian Conference on Laser Diagnostics in Fluid Mechanics and Combustion*, 2012.

A. Busemann. *Handbuch der Experimentalphysik*, volume 4. Geest und Portig, 1931.

T. H. Chilton and A. P. Colburn. Mass transfer (absorption) coefficients prediction from data on heat transfer and fluid friction. *Industrial & engineering chemistry*, 26(11):1183–1187, 1934.

Y. M. Chung and K. H. Luo. Unsteady heat transfer analysis of an impinging jet. *Journal of Heat Transfer*, 124(6):1039–1048, 12 2002.

L. Crocco. Sulla trasmissione del calore da una lamina piana a un fluido scorrente ad alta velocita. *L'Aerotecnica*, 12:181–197, 1932.

T. Cziesla, G. Biswas, H. Chattopadhyay, and N. Mitra. Large-eddy simulation of flow and heat transfer in an impinging slot jet. *International Journal of Heat and Fluid Flow*, 22(5):500–508, 2001.

C. B. da Silva and J. C. F. Pereira. Invariants of the velocity-gradient, rate-of-strain, and rate-of-rotation tensors across the turbulent/nonturbulent interface in jets. *Physics of Fluids*, 20(5):055101, 2008.

T. Dairay, V. Fortuné, E. Lamballais, and L. Brizzi. LES of a turbulent jet impinging on a heated wall using high-order numerical schemes. *International Journal of Heat and Fluid Flow*, 50(0):177–187, 2014.

T. Dairay, V. Fortuné, E. Lamballais, and L.-E. Brizzi. Direct numerical simulation of a turbulent jet impinging on a heated wall. *Journal of Fluid Mechanics*, 764:362–394, 2 2015.

L. Davidson. Inlet boundary conditions for embedded les. In *First CEAS European Air and Space Conference*, pages 10–13, 2007.

J. Eggels, F. Unger, M. Weiss, J. Westerweel, R. Adrian, R. Friedrich, and F. Nieuwstadt. Fully developed turbulent pipe flow: a comparison between direct numerical simulation and experiment. *Journal of Fluid Mechanics*, 268: 175–210, 1994.

T. M. Eidson and G. Erlebacher. Implementation of a fully balanced periodic tridiagonal solver on a parallel distributed memory architecture. *Concurrency: Practice and Experience*, 7(4):273–302, 1995.

O. Frederich. *Numerische Simulation und Analyse turbulenter Strömungen am Beispiel der Umströmung eines Zylinderstumpfes mit Endscheibe*. PhD thesis, Technische Universität Berlin, 2010.

J. Freund. Noise sources in a low-reynolds-number turbulent jet at mach 0.9. *Journal of Fluid Mechanics*, 438:277–305, Jul 2001.

R. Friedrich. Modelling of turbulence in compressible flows. In *Transition, Turbulence and Combustion Modelling*, volume 6 of *ERCOFTAC Series*, pages 243–348. Kluwer Academic Publishers, 1999.

G. Gerolymos and I. Vallet. Pressure, density, temperature and entropy fluctuations in compressible turbulent plane channel flow. *Journal of Fluid Mechanics*, 757:701, 2014.

H. Hattori and Y. Nagano. Direct numerical simulation of turbulent heat transfer in plane impinging jet. *International Journal of Heat and Fluid Flow*, 25(5): 749–758, 2004.

B. Henderson. The connection between sound production and jet structure of the supersonic impinging jet. *The Journal of the Acoustical Society of America*, 111(2):735–747, 2002.

B. Henderson and A. Powell. Experiments concerning tones produced by an axisymmetric choked jet impinging on flat plates. *Journal of Sound and Vibration*, 168(2):307–326, 1993.

M. Hirata, Y. Kukita, and T. Nakatogawa. Disintegration of a supersonic jet impinging normally on a flat plate. *Journal of Spacecraft and Rockets*, 8(4): 410–411, 1971.

C.-M. Ho and N. S. Nosseir. Dynamics of an impinging jet. part 1. the feedback phenomenon. *Journal of Fluid Mechanics*, 105:119–142, 4 1981.

P. Hrycak. Heat transfer from impinging jets. a literature review. Technical report, New Jersey Institute of Technology, 1981.

J. Iwamoto. Impingement of under-expanded jets on a flat plate. *Journal of Fluids Engineering*, 112(2):179–184, 1990.

K. Jambunathan, E. Lai, M. Moss, and B. Button. A review of heat transfer data for single circular jet impingement. *International Journal of Heat and Fluid Flow*, 13(2):106–115, 1992.

T. Janetzke. *Experimentelle Untersuchungen zur Effizienzsteigerung von Prallkühlkonfigurationen durch dynamische Ringwirbel hoher Amplitude*. PhD thesis, TU Berlin, 2010.

S. Kakag and Y. Yenner. *Convective Heat Transfer*. Crc Pr Inc, 2 edition, 1995.

C. A. Kennedy, M. H. Carpenter, and R. M. Lewis. Low-storage, explicit runge–kutta schemes for the compressible navier–stokes equations. *Applied Numerical Mathematics*, 35(3):177–219, 2000.

N. Kharoua and L. Khezzar. Flow asymmetry in symmetric multiple impinging jets: A large eddy simulation approach. *Journal of Engineering Research*, 8: 40–48, 2011.

A. Krothapalli, E. Rajkuperan, F. Alvi, and L. Lourenco. Flow field and noise characteristics of a supersonic impinging jet. *Journal of Fluid Mechanics*, 392: 155–181, 8 1999.

R. Lechner, J. Sesterhenn, and R. Friedrich. Turbulent supersonic channel flow. *Journal of Turbulence*, 2(1):001–001, 2001.

J. Lee and S.-J. Lee. Stagnation region heat transfer of a turbulent axisymmetric jet impingement. *Experimental Heat Transfer*, 12(2):137–156, 1999.

S. K. Lele. Compact finite difference schemes with spectral-like resolution.

Journal of Computational Physics, 103(1):16–42, November 1992.

J. N. B. Livingood and P. Hrycak. Impingement heat transfer from turbulent air jets to flat plates: a literature survey. *NASA, Lewis Research Center*, 1973.

A. H. Marsh. Noise measurements around a subsonic air jet impinging on a plane, rigid surface. *The Journal of the Acoustical Society of America*, 33(8): 1065–1066, 1961.

H. Martin. Heat and mass transfer between impinging gas jets and solid surfaces. In *Advances in heat transfer*, volume 13, pages 1–60, 1977.

D. M. Mitchell, D. R. Honnery, and J. Soria. The visualization of the acoustic feedback loop in impinging underexpanded supersonic jet flows using ultra-high frame rate schlieren. *Journal of Visualization*, 15(4):333–341, 2012.

R. Moser and P. Moin. Direct numerical simulation of curved turbulent channel flow. *NASA, Ames Research Center*, 1984.

G. Neuwerth. Acoustic feedback of a subsonic and supersonic free jet which impinges on an obstacle. *NASA TTF-15719*, 1974.

G. Neuwerth. Flow field and noise sources of jet impingement on flaps and ground surface. *AGARD CCP*, 308:13.1–13.7, 1981.

M. L. Norman, L. Smarr, K.-H. A. Winkler, and M. D. Smith. Structure and dynamics of supersonic jets. *Astronomy and Astrophysics*, 113:285–302, 1982.

N. S. Nosseir and C.-M. Ho. Dynamics of an impinging jet. part 2. the noise generation. *Journal of Fluid Mechanics*, 116:379–391, 3 1982.

J. Panda. Shock oscillation in underexpanded screeching jets. *Journal of Fluid Mechanics*, 363:173–198, 1998.

J. Panda, G. Raman, K. Zaman, J. Panda, G. Raman, and K. Zaman. Underexpanded screeching jets from circular, rectangular and elliptic nozzles. In *3rd AIAA/CEAS Aeroacoustics Conference*, number 97-1623. AIAA, 1997.

J. J. Peña Fernández and J. Sesterhenn. Interaction between the shear layer, shock-wave and vortex ring in a starting free jet injecting into a plenum. In *European Turbulence Conference*, 2015.

S. Pirozzoli, M. Bernardini, and F. Grasso. Characterization of coherent vortical structures in a supersonic turbulent boundary layer. *Journal of Fluid Mechanics*, 613:205–231, 10 2008.

T. Poinsot and D. Veynante. *Theoretical and numerical combustion.* RT Edwards, Inc., 2005.

S. B. Pope. *Turbulent flows.* Cambridge university press, 2000.

A. Powell. On the mechanism of choked jet noise. *Proceedings of the Physical Society. Section B*, 66(12):1039, 1953.

A. Powell. The sound-producing oscillations of round underexpanded jets impinging on normal plates. *The Journal of the Acoustical Society of America*, 83:515–533, 1988.

A. Powell, Y. Umeda, and R. Ishii. Observations of the oscillation modes of choked circular jets. *The Journal of the Acoustical Society of America*, 92(5): 2823–2836, 1992.

G. Raman. Cessation of screech in underexpanded jets. *Journal of Fluid Mechanics*, 336:69–90, 1997.

G. Raman. Advances in understanding supersonic jet screech: review and perspective. *Progress in Aerospace Sciences*, 34(1–2):45–106, 1998.

N. Riley. *In Fascination of Fluid Dynamics: A Symposium in Honour of Leen van Wijngaarden*, chapter The Fascination of Vortex Rings, pages 169–189. Springer Netherlands, Dordrecht, 1998.

D. Rockwell and E. Naudascher. Self-sustained oscillations of impinging free shear layers. *Annual Review of Fluid Mechanics*, 11(1):67–94, 1979.

M. W. Rubesin. Extra compressibility terms for favre-averaged two-equation models of inhomogeneous turbulent flows. *NASA STI/Recom Tech. Rep. N 90, 23701*, 1990.

S.-i. Satake and T. Kunugi. Direct numerical simulation of an impinging jet into parallel disks. *International Journal of Numerical Methods for Heat & Fluid Flow*, 8(7):768–780, 1998.

H. Schade and K. Neemann. *Tensoranalysis.* De Gruyter, 2 edition, 2006.

H. Schlichting and K. Gersten. *Grenzschicht-Theorie.* Springer-Verlag, 2006.

P. Schmid. Application of the dynamic mode decomposition to experimental data. *Experiments in Fluids*, 50(4):1123–1130, 2011.

P. J. Schmid. Dynamic mode decomposition of numerical and experimental data. *Journal of Fluid Mechanics*, 656:5–28, 8 2010.

P. J. Schmid and J. Sesterhenn. Dynamic mode decomposition of numerical and experimental data. In *Amer. Phys. Soc., 61st APS meeting*, page 208, San Antonio, 2008.

J. Schulze. *Adjoint based jet-noise minimization.* PhD thesis, TU Berlin, 2013.

J. Seiner and J. C. Yu. Acoustic near-field properties associated with broadband shock noise. *AIAA Journal*, 22(9):1207–1215, 1984.

J. Sesterhenn. A characteristic–type formulation of the Navier–Stokes equations for high order upwind schemes. *Computers & Fluids*, 30(1):37–67, 2001.

J. Sesterhenn, F. C. Miranda, and J. J. Peña Fernández. Numerical simulation of starting, particle-laden jets from pressurised containments. In *EGU General Assembly Conference Abstracts*, volume 15, page 4817, 2013.

G. S. Settles. *Schlieren and shadowgraph techniques: visualizing phenomena in transparent media*. Springer Science & Business Media, 2001.

G. Sinibaldi, G. Lacagnina, L. Marino, and G. P. Romano. Aeroacoustics and aerodynamics of impinging supersonic jets: Analysis of the screech tones. *Physics of Fluids*, 25(8):–, 2013.

G. Sinibaldi, L. Marino, and G. P. Romano. Sound source mechanisms in under-expanded impinging jets. *Experiments in Fluids*, 56(5):1–14, 2015.

T. Suzuki and S. K. Lele. Shock leakage through an unsteady vortex-laden mixing layer: application to jet screech. *Journal of Fluid Mechanics*, 490: 139–167, 2003.

C. K. W. Tam. Supersonic jet noise. *Annual Review of Fluid Mechanics*, 27(1): 17–43, 1995.

C. K. W. Tam and K. K. Ahuja. Theoretical model of discrete tone generation by impinging jets. *Journal of Fluid Mechanics*, 214:67–87, 5 1990.

C. K. W. Tam and H. K. Tanna. Shock associated noise of supersonic jets from convergent-divergent nozzles. *Journal of Sound and Vibration*, 81(3):337–358, 1982.

G. I. Taylor. The conditions necessary for discontinuous motion in gases. *Proceedings of the Royal Society of London. Series A*, 84(571):371–377, 1910.

M. Tsubokura, T. Kobayashi, N. Taniguchi, and W. Jones. A numerical study on the eddy structures of impinging jets excited at the inlet. *International Journal of Heat and Fluid Flow*, 24(4):500–511, 2003.

K. Tsujimoto, T. Ishikura, T. Shakouchi, and T. Ando. Direct numerical simulation of active-controlled impinging jets. *Journal of Fluid Science and Technology*, 4(2):279–291, 2009.

H.-G. Uhlmann. *Früherkennung aerodynamischer Verdichterinstabilitäten mittels Wavelet-Transformationsregeln*. PhD thesis, Universität München, 2003.

Y. Umeda and R. Ishii. On the sound sources of screech tones radiated from choked circular jets. *The Journal of the Acoustical Society of America*, 110 (4):1845–1858, 2001.

A. Uzun, R. Kumar, M. Y. Hussaini, and F. S. Alvi. Simulation of tonal noise generation by supersonic impinging jets. *AIAA Journal*, 51(7):1593–1611, 2013.

R. Viskanta. Heat transfer to impinging isothermal gas and flame jets. *Experimental Thermal and Fluid Science*, 6(2):111–134, 1993.

A. Walz. *Compressible turbulent boundary layers.* Ed. du Centre National de la Recherche scientifique, 1962.

B. Weigand and S. Spring. Multiple jet impingement - a review. *Heat Transfer Research*, 42(2):101–142, 2011.

Y.-S. Zhang, W.-T. Bi, F. Hussain, and Z.-S. She. A generalized reynolds analogy for compressible wall-bounded turbulent flows. *Journal of Fluid Mechanics*, 739:392–420, 2014.

N. Zuckerman and N. Lior. Impingement heat transfer: Correlations and numerical modeling. *Journal of Heat Transfer*, 127(5):544–552, 05 2005.

Publications related to this thesis

Parts of this thesis have been published in:

F. Haucke, W. Nitsche, R. Wilke, and J. L. Sesterhenn. Experimental and numerical investigations regarding pulsed impingement cooling. In *Deutscher Luft- und Raumfahrt Kongress*, Rostock, Germany, 2015.

R. Wilke and J. Sesterhenn. Direct numerical simulation of heat transfer of a round subsonic impinging jet. In *Active Flow and Combustion Control 2014*, pages 147–159. Springer, 2015a.

R. Wilke and J. Sesterhenn. Numerical simulation of impinging jets. In *High Performance Computing in Science and Engineering '14*, pages 275–287. Springer, 2015b.

R. Wilke and J. Sesterhenn. Numerical simulation of subsonic and supersonic impinging jets. In *High Performance Computing in Science and Engineering '15*, pages 349–369. Springer, 2016a.

R. Wilke and J. Sesterhenn. On the origin of impinging tones at low supersonic flow. *arXiv preprint arXiv:1604.05624*, 2016b.

R. Wilke and J. Sesterhenn. Statistics of fully turbulent impinging jets. *arXiv preprint arXiv:1606.09167*, 2016c.

R. Wilke and J. Sesterhenn. Numerical simulation of subsonic and supersonic impinging jets II. In *High Performance Computing in Science and Engineering '16*. Springer, 2017.